

https://dspace.org/

Colloidal synthesis of WS2 nanostructures for application as electrode materials

Mphahlele, Lerato Sharon

2019

https://hdl.handle.net/10539/28831

Downloaded from a DSpace repository. https://dspace.org/



Colloidal synthesis of WS_2 nanostructures for application as electrode materials

A dissertation submitted to the Faculty of Science, University of the Witwatersrand in partial fulfilment of the requirements for the degree of Masters of Science in Chemistry

By

LERATO SHARON MPHAHLELE

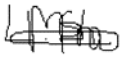
Student number:

609024

Supervisors: Prof. Nosipho Moloto and Dr. Siziwe Gqoba

Declaration

I declare that the work reported in this document is my own independent work. Submitted at the School of Chemistry, University of the Witwatersrand, Johannesburg. This work has not been submitted for any degree or examination in any other institution of higher learning.



	01/02/2019
Candidate	Date
(Lerato Sharon Mphahlele)	



	01/02/2019
Supervisor	Date
(Prof N. Moloto)	



	01/02/2019
Co-Supervisor	Date
(Dr S.S. Gqoba)	

Abstract

WS_2 is a material that has a two-dimensional, layered structure. The properties of WS_2 have made it an attractive material to be used in various applications such as sensors, photovoltaic devices and even as electrocatalysts. Its properties include a band gap that is comparable to that of silicon, electrocatalytic properties and good electronic properties. These properties have made WS_2 a candidate for application as a counter electrode in dye-sensitized solar cells. The counter electrode catalyses the redox reaction of the iodine electrolyte used within the cell. The synthesis of WS_2 nanostructures using the colloidal synthesis is reported in this project. Colloidal synthesis, unlike readily used methods such as exfoliation and chemical vapour deposition, has advantages such as mild synthetic conditions, reaction parameters that can be varied and the possibility of scaling up the reaction. Therefore, the effects of the capping agents, tungsten precursors as well as the sulphur precursors on the properties of WS_2 were investigated. The use of oleylamine as the sole precursor produced WS_2 with a flower-like morphology. When oleic acid was added in different ratios to oleylamine, the morphology changed to a stacked, petal-like morphology and flattened out as the oleic acid ratio was increased. When oleyl alcohol was used as a co-capping agent, the lower concentration of oleyl alcohol produced flower-like WS_2 and evolved into flatter, folded WS_2 nanosheets as the oleyl alcohol concentration was increased. Octadecene as a co-capping agent produced WS_2 with a flower-like morphology. All the WS_2 produced from these capping agents were semiconducting with visible light absorption. The metal precursors had a significant effect on the structure of the WS_2. Ammonium tungstate ($(NH_4)_{10}(H_2W_{12}O_{42})$) produced highly crystalline, flat, disc-like materials while tungsten hexacarbonyl ($W(CO)_6$) and tungsten hexachloride (WCl_6) resulted in the formation of less crystalline material that lacked the optical characteristics of WS_2. WCl_6 also produced a mixture of WS_2 and WO_3, while $W(CO)_6$ formed very small flakes. Sulfur precursors varied from thiourea to thioacetamide to diphenyl thiourea. Semiconducting WS_2 was obtained from all these precursors. The morphologies were flower-like for thiourea and diphenyl thiourea, while thioacetamide formed WS_2 that had a crumpled sheet-like morphology. Electrocatalytic measurements through cyclic voltammetry revealed that the WS_2 produced in some of these reactions are promising as they were able to oxidize and reduce the iodine electrolyte. However, some showed an inefficient reduction of the electrolyte. Reversibility was observed as a significant problem as the reduction of the electrolyte was not as efficient as the oxidation.

Acknowledgments

I would firstly like to thank Jesus Christ for allowing me this opportunity. I would also like to thank my supervisors Prof Nosipho Moloto and Dr Siziwe Gqoba for giving me the chance to be in their research group and for their continued help and support, both academically and financially. I also would like to thank Dr Rudolph Erasmus, Dr Boitumelo Matsoso and Thomas Mongwe for Raman Spectroscopy analysis. I thank all my lab co-workers who have helped me during these two years. Everybody from the CATMAT research group. I want to thank Tshwarela Kolokoto and Puledi Mphago with whom I worked closely as we worked on our dissertations. I would also like to thank the MMU staff for their constant help with microscopy analysis. I also acknowledge Dr Caren Billing for giving me access to the cyclic voltammetry equipment. Last but not least, I want to thank my family for being patient while I finished this degree. I want to thank my mom and grandmother for their prayers and my aunt for all her support. I also must give thanks to my friends and church family who have been supportive during this year.

List of presentations

1. Poster presentation at Frontiers of Electron Microscopy in Materials Science (FEMMS) held at Indaba hotel & conference centre, Johannesburg (September 2017).
2. Poster presentation at SACI NanoAfrica conference held at Salt rock hotel, Durban (April 2018).
3. Oral presentations at (Catalysis and Materials) CATMAT Seminar held at the University of the Witwatersrand, School of Chemistry (2017 and 2018).

List of publications

1. Synthesis of WS_2 nanostructures with various ratios of organic capping agents, to be submitted to *2D Materials* (2019).
2. The effect of tungsten and sulphur precursors on the properties WS_2, to be submitted to *New Journal of Chemistry* (2019).

Table of Contents

Declaration ii
Abstract iii
Acknowledgments iv
List of presentations v
List of publications v
List of figures viii
List of tables xi
List of abbreviations xi
Synopsis xiii
Chapter 1 1
Introduction 1
1.1 Background 1
1.2 Rationale for the study 2
1.3 Aim of the project 2
Chapter 2 4
Literature review 4
2.1 Transition metal dichalcogenides 4
2.2 WS_2 structure 5
2.3 Electronic structure and properties 6
2.4 Raman spectroscopy of WS_2 9
2.5 Synthesis of TMDs 12
2.6 Colloidal growth mechanisms 18
2.7 Application of WS_2 as a counter electrode in dye-sensitized solar cells 20
2.8 References 23
Chapter 3 27
Synthesis of WS_2 nanostructures with various ratios of organic capping agents 27
3.1 Introduction 27
3.2 Materials and method 29
3.3 Results and discussion 30
3.4 Conclusion 58
3.5 References 59
Chapter 4 62
Synthesis of WS_2 nanostructures with different tungsten precursors 62
4.1 Introduction 62
4.2 Methods and materials 63

4.3 Results and discussion 64
4.4 Proposed Mechanisms 72
4.5 Conclusion 75
4.6 References 75
Chapter 5 78
Synthesis of WS_2 using thiourea, thioacetamide, and N, N'-diphenyl thiourea as sulphur precursors 78
5.1 Introduction 78
5.2 Method and materials 79
5.3 Results and discussion 80
5.4 Proposed mechanisms 88
5.5 Conclusion 90
5.6 References 90
Chapter 6 93
Cyclic voltammetry of WS_2 materials for determination of electrocatalytic activity as a counter electrode 93
6.1 Introduction 93
6.2 Method and materials 94
6.3 Results and discussion 94
6.4 Conclusion 99
6.5 References 99
Chapter 7 102
General conclusions and recommendations 102

List of figures

Figure 2.1: Periodic table showing the transition metals and chalcogen atoms found in transition metal dichalcogenides. 5
Figure 2.2: (a) Layered crystal structure of WS_2 with (b) a depiction of the trigonal prismatic and octahedral coordination of the tungsten metal to the chalcogen precursors.[10] The stacking orders characteristic of (c) 2H, (d) 1T[11] and (e) 3R[3] polytypes. 6
Figure 2.3: Representation of the electronic structure of WS_2 as the number of layers change from bulk to monolayer.[11] 7
Figure 2.4: Simplified electronic structure of group 6 TMDs showing the co-existence of the split direct band gap and the indirect band gap.[10] 8
Figure 2.5: Representations of the (a) $E^1_{2g}(\mathbf{\Gamma})$ and (b) $A_{1g}(\mathbf{\Gamma})$ Raman modes of WS_2. 10
Figure 2.6: Diagram depicting the basic mechanism of top-down synthesis of transition metal dichalcogenides. 12
Figure 2.7: Nano-mechanical exfoliation using tungsten probe.[3] 13
Figure 2.8: Diagram depicting basic bottom-up synthesis of transition metal dichalcogenides. 14
Figure 2.9: Diagram of the classical nucleation theory showing the dependence of the free energy (ΔG) on the radius (r) of the nuclei.[44] 19
Figure 2.10: Diagram showing the separation between nucleation and growth based on Lamer's theory. 20
Figure 2.11: Diagram of a basic dye-sensitized solar cell. 21
Figure 2.12: Cyclic voltammograms showing the two oxidation and reduction peaks associated with the I^-/I_3^- electrolyte.[53] 22
Figure 3.1: Schematic showing the preferential binding of capping agents to specific facets of silver nanoparticles.[14] 28
Figure 3.2: Capping agent molecules: (a) oleylamine, (b) 1-octadecene, (c) oleic acid and (d) oleyl alcohol. 29
Figure 3.3: (a) PXRD pattern and (b) Raman spectrum of WS_2 synthesized with only oleylamine as a capping agent. 31
Figure 3.4: (a) TEM and (b) SEM micrographs of flower-like WS_2 synthesized with only oleylamine as a capping agent. 32
Figure 3.5: ^{1}H-NMR spectra of (a) WS_2 nanoparticles capped with oleylamine and (b) pure oleylamine. 33

Figure 3.6: UV-Vis absorption spectrum of WS_2 synthesized with only oleylamine as a capping agent. 34
Figure 3.7: PXRD patterns of WS_2 synthesized with increasing concentrations of octadecene. 35
Figure 3.8: EDS spectra of WS_2 prepared with a (a) 25%, (b) 50% and (c) 75% concentration of octadecene 35
Figure 3.9: Raman spectra of WS_2 synthesized with different concentrations of octadecene as a co-capping agent. 36
Figure 3.10: TEM micrographs of WS_2 obtained using (a, b) 25%, (c, d) 50% and (e, f) 75% concentration of octadecene. 38
Figure 3.11: FT-IR spectra of (a) pure oleylamine and octadecene and (b, c) WS_2 synthesized with both capping agents. 40
Figure 3.12: ^{1}H-NMR spectra of (a) pure oleylamine, (b) WS_2 and (c) pure octadecene. 41
Figure 3.13: UV-Vis absorption spectra of WS_2 prepared using various concentrations of octadecene. 42
Figure 3.14: PXRD patterns of WS_2 synthesized using various concentrations of oleic acid. 43
Figure 3.15: Raman spectra of WS_2 from various concentrations of oleic acid. 44
Figure 3.16: TEM and SEM images of WS_2 synthesized with (a, b) 25%, (c, d) 50%, (e, f) 75% and (g, h) 100% concentration of oleic acid. 45
Figure 3.17: FT-IR spectra of (a) pure oleylamine and oleic acid as well as (b, c) WS_2 synthesized with different concentrations of oleic acid. 47
Figure 3.18: ^{1}H-NMR spectra of (a) pure oleic acid, (b) capped WS_2 and (c) pure oleylamine. 48
Figure 3.19: UV-Vis absorption spectra of WS_2 synthesized with various concentrations of oleic acid. 49
Figure 3.20: PXRD patterns of WS_2 synthesized with different concentrations of oleyl alcohol. 50
Figure 3.21: Raman spectra of WS_2 obtained from varying concentrations of oleyl alcohol. 51
Figure 3.22: (a) TEM and (b) SEM micrographs of WS_2 synthesized with 25% oleyl alcohol. 52
Figure 3.23: (a) TEM and (b, c) SEM micrographs of WS_2 nanoflowers synthesized with 50% concentration of oleyl alcohol. 53
Figure 3.24: (a, b) TEM and (c) SEM micrographs of WS_2 synthesized with 75% oleyl alcohol. 54

Figure 3.25: FT-IR spectra of (a) pure oleylamine and oleyl alcohol as well as (b, c) WS_2 synthesized with both these capping agents.....55
Figure 3.26: ^{1}H-NMR spectra of (a) pure oleyl alcohol, (b) capped WS_2 and (c) pure oleylamine. The insets (d, e) are a magnification of the areas on the spectra indicated by the rectangles. 56
Figure 3.27: UV-Vis absorption of WS_2 using various concentrations of oleyl alcohol. 57
Figure 4.1: (a) Ammonium tungstate anion $[H_2W_{12}O_{42}]^{10-}$, (b) WCl_6 and (c) $W(CO)_6$. 63
Figure 4.2: PXRD patterns (a) and Raman spectra (b) of WS_2 synthesized using three different tungsten precursors and (c) Raman spectra of the WCl_6 and $W(CO)_6$ samples at 532 nm excitation wavelength. 65
Figure 4.3: EDS spectra of WS_2 synthesized with (a) ammonium tungstate, (b) WCl_6 and (c) $W(CO)_6$. 67
Figure 4.4: (a) TEM image showing WS_2 nanodisks and some curled up nanostructures. HRTEM images show the (b) layered structure of the WS_2, (c) the crystalline basal plane of the WS_2 and (d) magnified image of the basal plane showing the hexagonal crystal structure of WS_2. The SEM micrograph (e) of WS_2 disks/flakes synthesized from ammonium tungstate. 68
Figure 4.5: TEM (a), HRTEM (b, c) and SEM (d) micrographs of nanostructures synthesized with WCl_6.....69
Figure 4.6: (a, b) TEM images of nanostructures synthesized using $W(CO)_6$. 70
Figure 4.7: FT-IR spectra of pure oleylamine, as well as WS_2, synthesized with ammonium tungstate, WCl_6, and $W(CO)_6$. 71
Figure 4.8: UV-Vis absorption (a) and PL emission (b) spectra of the WS_2 produced from ammonium tungstate (black), WCl_6 (blue) and $W(CO)_6$ (green). 72
Figure 4.9: (a) White HCl gas evolved when WCl_6 is added to oleylamine and (b) WO_2Cl_2 solid that forms when WCl_6 is exposed to air. 74
Figure 5.1: Chemical structures of (a) thiourea, (b) thioacetamide and (c) diphenyl thiourea. 79
Figure 5.2: PXRD patterns for WS_2 obtained from thiourea, thioacetamide and diphenyl thiourea at 60 min reaction time. 81
Figure 5.3: Raman spectra of WS_2 obtained from thiourea, thioacetamide and diphenyl thiourea of the 60 min reaction time. 82
Figure 5.4: TEM images of WS_2 synthesized with thiourea for (a) 30 and (b) 60 minutes and a (c) SEM image of the 60 minute WS_2.....83

Figure 5.5: TEM images of WS_2 synthesized with thioacetamide for 30 (a) and 60 (b) minutes, including a SEM image (c) of the 60 min WS_2. 84
Figure 5.6: TEM images of WS_2 nanostructures obtained from diphenyl thiourea at (a) 30 and (b) 60 min reaction time and a (c) SEM image of the 60 minute WS_2 nanostructures. 85
Figure 5.7: (a) FT-IR spectra of pure oleylamine (black) and WS_2 derived from thiourea (blue), thioacetamide (red) and diphenyl thiourea (green) for the 60 min reaction time and (b) magnification of N-H stretch on pure oleylamine. 86
Figure 5.8: (a) UV-Vis absorption and (b) PL emission spectra of WS_2 obtained from thiourea, thioacetamide and diphenyl thiourea for the 60 min reaction time. 88
Figure 6.1: Cyclic voltammogram of platinum as a counter electrode. 95
Figure 6.2: Cyclic voltammograms of WS_2 –ODE at (a) 50 mV/s and (b) 10, 20, 50 and 100 mV/s scan rates. 96
Figure 6.3: Cyclic voltammogram of WS_2 synthesized with a 25% oleic acid concentration. (a) 50 mV/s and (b) 10, 20, and 100 mV/s scan rates. 97
Figure 6.4: Cyclic voltammograms of WS_2 synthesized with diphenyl thiourea as a sulfur source. (a) 50 mV/s only and (b) combined voltammograms with 10, 20, and 100 mV/s scan rate 98

List of tables

Table 3.1: Table showing ratios of oleylamine to the other capping agents used in capping agent study 29
Table 3.2: The wavelengths at which the absorption peaks of WS_2 peaks appear 42
Table 3.3: Raman shifts of the E^1_{2g} and $A_{1g}(\Gamma)$ modes of WS_2 synthesized with various concentrations of oleyl alcohol 51
Table 5.1: Raman shifts of 2LA(M) and $A_{1g}(\Gamma)$ modes, including the intensity ratios 82

List of abbreviations

ALD – Atomic layer deposition

CE – Counter electrode

CNT– Classical nucleation theory

CTAB – Cetrimonium bromide

CV– Cyclic voltammetry

CVD – Chemical vapour deposition

DSSC – Dye-sensitized solar cell

EDS – Energy dispersive spectroscopy

FT-IR – Fourier Transform Infrared

GPES – General Purpose Electrochemical System software

NC – Nanocrystal

NP – Nanoparticle

OAc – Oleic acid

ODE – 1-Octadecene

OLA – Oleylamine

PCE – Photoelectric conversion efficiency

PEG – Polyethylene glycol

PL – Photoluminescence

PVA – Polyvinyl alcohol

PXRD – Powder x-ray diffraction

TMD – Transition metal dichalcogenide

Synopsis

The aim of the study was to synthesize 2D layered tungsten sulphide nanostructures (WS_2) using the colloidal synthesis method and to evaluate their electrocatalytic properties using cyclic voltammetry for potential application as counter electrodes in dye-sensitized solar cells in order to replace the expensive Pt counter electrode. The layout of the dissertation is shown below:

Chapter 1: is comprised of the general background and rationale for the study as well as aims and objectives.

Chapter 2: is the literature review of transition metal dichalcogenides, in particular the properties of WS_2 and the various methods used to synthesize the materials. In addition, a short review on the application of WS_2 as a counter electrode for dye sensitized solar cells.

Chapter 3: reports on the effect of using various ratios of organic capping agents on the properties of WS_2 nanostructures formed during synthesis.

Chapter 4: reports on the effect of different tungsten precursors on the structure and properties of the WS_2 materials.

Chapter 5: reports on the effect of different sulphur precursors on the structure and properties of the WS_2 materials.

Chapter 6: reports on the investigation of WS_2 as an alternative electrode for DSSCs through cyclic voltammetry scans of thin films made from the WS_2 materials produced in previous chapters.

Chapter 7: critically looks at the conclusions and suggests possible future studies.

Chapter 1
Introduction

1.1 Background

Since the Kyoto protocol, several countries have committed to decreasing their fossil fuel and greenhouse gas emissions. This protocol is an international agreement between several countries to reduce greenhouse gases, because emission of these gases have been the major cause of global warming or climate change. In order to mitigate this issue, alternative energy sources are required to relieve the dependence on fossil fuel energy. The dependence on coal-generated electricity in South Africa is very high while the supply is not sufficient. This has led to some rural areas in South Africa still not having access to electricity or the electricity is very expensive. It is therefore important that technologies are developed for the harvesting of alternative energy in such a way as to provide more affordable electricity as well as protecting the environment and decreasing the fossil fuel emissions. It is evident that the sun is the most abundant energy source available. It is free and does not get depleted or lead to the emission of any greenhouse gases. Hence solar power is an attractive alternative to be explored for the generation of clean and affordable electricity in South Africa. Over the years research into solar energy has been extensive, starting with the first generation crystalline silicon solar cells to the third generation inorganic thin film solar cells such as GaAs etc. An approach that many countries, including South Africa, have taken to confront the energy issue is nanotechnology. Many nanomaterials have been identified as probable or attractive ways of harvesting solar energy; from polymer materials to metal oxides and transition metal dichalcogenides. These materials have been flagged as possible components of solar cells either as the active semiconductor or as electrode materials.

Semiconductor materials that absorb visible light are attractive in that they can act as active materials in photovoltaic cells for the conversion of photons into electrical currents. Some materials are better used as electrode materials for the separation of charge carriers that the semiconducting active materials produce.

WS_2 is a layered material that has both semiconducting and catalytic properties, making it an attractive candidate for application as a counter electrode in dye-sensitized solar cells (DSSCs). DSSCs were developed first in 1991 by O'Regan and Gratzel with efficiencies of

about 7%. Since then, research into DSSCs has grown rapidly. One of the major components of the DSSC is the counter electrode. A role typically filled by platinum. The counter electrode has two main functions: it catalyses the redox reaction of the electrolyte within the cell and it collects electrons from the external circuit and injects them back into the cell. Although platinum has been used extensively as a counter electrode due to its efficiency in catalysing the electrolyte redox reactions, it is also very expensive and gets corroded by the iodine electrolyte within the cell. This encourages the search for alternative materials that can replace platinum. Transition metal dichalcogenides such as WS_2 have been shown to have the catalytic and conductive properties necessary to work as a counter electrode.

1.2 Rationale for the study

As was mentioned before, platinum, although a good counter electrode, is expensive and prone to corrosion and requires new materials to be developed to replace it. This also means that suitable synthetic pathways for WS_2 are necessary that will allow for cost effective and energy efficient fabrication of DSSCs. Vapour deposition and exfoliation methods are the most widely used synthetic methods for WS_2. These methods, however, are not easy to scale up and they have high energy requirements. Colloidal synthesis is one of the most scalable methods of synthesis for WS_2. There are many adjustments that can be made to the synthetic method to optimize the formation of transition metal dichalcogenides in high yields. In the instance where scaling up will be necessary, the frequently used methods will not be able to supply the demand, but colloidal synthesis can.

1.3 Aim of the project

The main aim of this project was to investigate the colloidal synthesis of WS_2 nanomaterials and to determine how certain reaction parameters, such as capping agents, sulphur and tungsten precursors, affect the resultant WS_2. Furthermore it was to determine what parameters are necessary to obtain materials that are catalytically efficient.

In order to achieve the abovementioned aim, the following objectives were carried out:

- Colloidal synthesis and characterization of WS_2 nanostructures using different organic capping agent ratios
- Colloidal synthesis and characterization of WS_2 nanostructures using different tungsten precursors

- Colloidal synthesis and characterization of WS_2 nanostructures using different sulphur precursors
- Fabrication of thin films from the WS_2 nanostructures for cyclic voltammetry measurements
- Performance of cyclic voltammetry to determine the electrocatalytic activity of the WS_2 produced.

Chapter 2
Literature review

2.1 Transition metal dichalcogenides

Transition metal dichalcogenides (TMDs) are a class of layered materials where an individual layer consists of a metal atom layer sandwiched between two chalcogen layers in the X-M-X form, M being the metal atom and X being the chalcogen atom. The transition metals involved are usually from group 4 to group 6, while the chalcogen atoms are usually sulphur (S), selenium (Se) and tellurium (Te) as shown in Figure 2.1. The M-X bonds are strong covalent bonds within the layers, while the layers are held together by weak van der Waals forces as shown in Figure 2.2 (a).[1] This particular layered structure means that the physical and chemical properties of these materials are highly affected by the number of layers present.[2] There are approximately 40 combinations of layered TMDs and these different combinations give rise to different electronic structures and hence also exhibit different electronic properties. Some of these layered TMDs show insulating behaviour ($HfSe_2$), while others have semi-metallic (WTe_2), metallic ($NbSe_2$) and semiconducting properties (WS_2).[3] Some of these TMDs are unstable and react with the atmosphere which diminishes any interest in them.[3,4]

Group 6 TMDs are the materials of interest, in this case, especially WS_2, due to its band gap that lies between 1 and 2 eV which is appropriate for many optoelectronic applications.[3] WS_2 also has better thermal stability, high surface area[5], tunable band structure[6], high carrier mobility[4] and a high on/off ratio[3,7] that makes WS_2 a suitable material for field effect transistors. It also has the potential for efficient light harvesting, low threshold lasing and sensitive photodetection.[8] The tunable band structure makes it possible to manipulate the material's versatile properties. WS_2 can also undergo large amounts of strain without degradation, meaning it can be used in flexible and wearable electronics.[8] Physicists have found this material interesting as it has properties such a high quantum yield and a large exciton binding energy that makes it suitable for optoelectronic applications.[9]

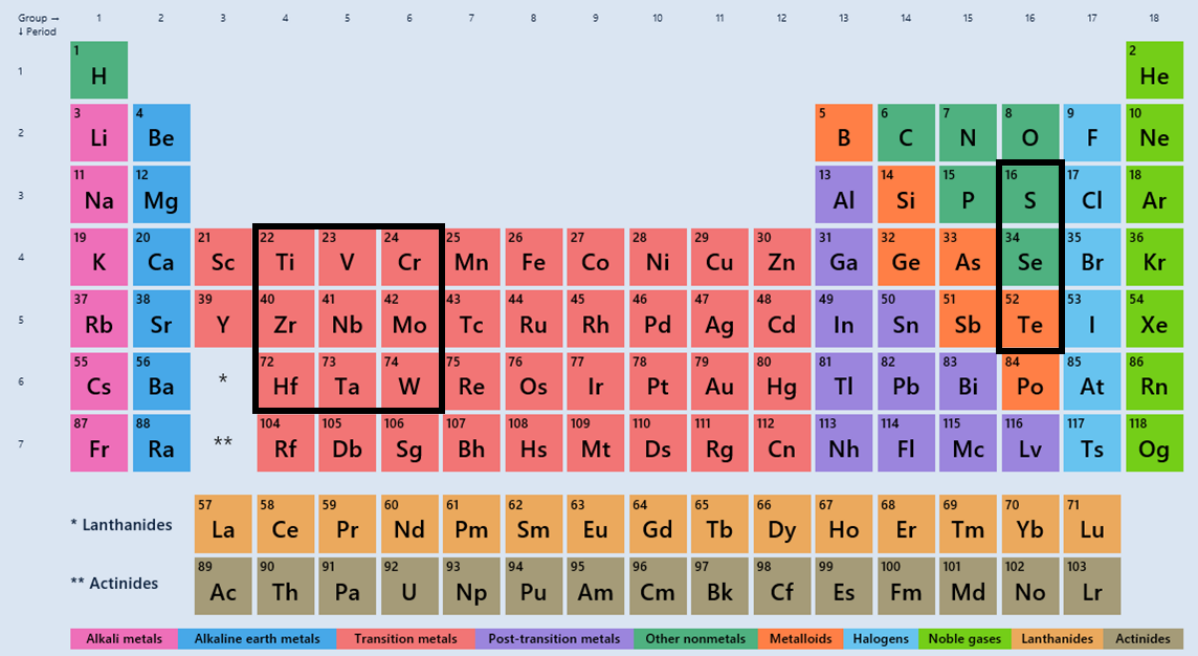


Figure 2.1: Periodic table showing the transition metals and chalcogen atoms found in transition metal dichalcogenides.

2.2 WS_2 structure

WS_2, made up of S-W-S layers (Figure 2.2 (a)) as described in section 2.1, can stack into different polytypes namely 1T (trigonal), 2H (hexagonal) and 3R (rhombohedral) where the letters represent the symmetry of the polytype and the number indicates the number of layers in a unit cell.[4,10] The formation of these polytypes depends on the coordination spheres of the metal atoms, as well as the stacking order of the layers.[4,10,11] 2H and 3R WS_2 have trigonal prismatic coordination of the tungsten atoms while the 1T polytype shows octahedral coordination of the tungsten atom to 6 sulphur atoms as shown in Figure 2.2 (b).[12] The stacking order refers to the sequence in which the individual S-W-S layers stack. For example, 2H-WS_2 has an AbA stacking order, meaning the chalcogen atoms (capital letters) in the layers occupy the same space or are aligned with each other in the layers [11] while the metal atom (small letters) is in a different position (Figure 2.2 (c)). The 1T polytype has an AbC stacking order, where the chalcogen atoms in the layers are not aligned with each other (Figure 2.2 (d)).[11] The 3R polytype has an AbA BcB stacking order as shown in Figure 2.2 (e). For WS_2 the 2H polytype is the more thermodynamically stable type. The 1T polytype can be obtained through specialized synthetic methods, but can easily be transformed into the 2H type when heated. [13]

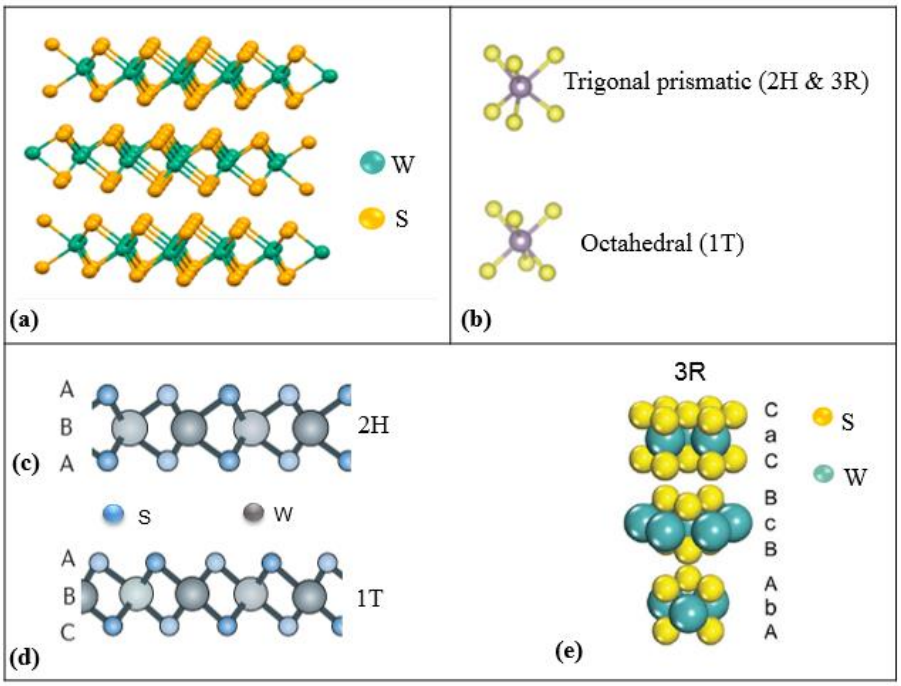


Figure 2.2: (a) Layered crystal structure of WS_2 with (b) a depiction of the trigonal prismatic and octahedral coordination of the tungsten metal to the chalcogen precursors.[10] The stacking orders characteristic of (c) 2H, (d) 1T[11] and (e) 3R[3] polytypes.

2.3 Electronic structure and properties of transition metal dichalcogenides

The electronic structure of TMDs has been studied extensively through density functional theory (first principles calculations) as well as various spectroscopy methods.[4] The coordination sphere of the metal, as well as its d-electron count, affects the electronic structure of the TMDs produced, which further affects their properties. This is clearly seen in the differences between the TMDs obtained from different groups of transition metals. The diverse electronic properties arise from the filling of the non-bonding d-orbitals from Group 4 to group 10 metals. An example is that when the d-orbitals are partially filled, the materials show metallic behaviour as in 2H-$NbSe_2$. Whereas when the orbitals are fully occupied as in 2H-WS_2, the materials exhibit semiconducting properties.[10] Another significant property of the materials, especially the group 6 semiconducting TMDs, is the gradual transition of the band structure from an indirect to a direct band gap.[7,12] This transition occurs when the thickness of the material is reduced from bulk to monolayer form. From first principles calculations it was shown that for 2H-WS_2, the band gap is indirect between the valence band maximum (VBM) at the Γ-point and the conduction band minimum (CBM) at the midpoint

between the K-point and Γ-point a shown in Figure 2.3. The band gap transitions to direct at the K-point of the Brouillon zone in monolayers. The transition of the band gap means that the materials will have a higher quantum efficiency and more light emission which is ideal for electronic applications such light emitting diodes.[3] The intrinsic band gap of 2H-WS_2 makes it suitable for use in transistor channels.[14]

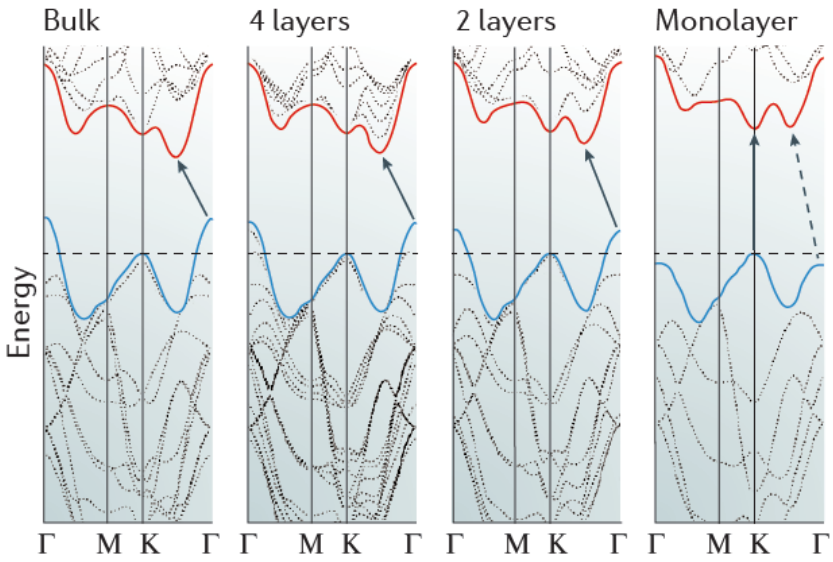


Figure 2.3: Representation of the electronic structure of WS_2 as the number of layers change from bulk to monolayer.[11]

The electronic band structure of the TMDs also gives rise to the optical properties of the material as shown in Figure 2.4. A simplified band structure of MoX_2 is shown indicating the indirect nature of the gap at the Γ-point and the direct nature of the gap at the K-point. It also shows the nature of the excitonic transitions that occur within the material.

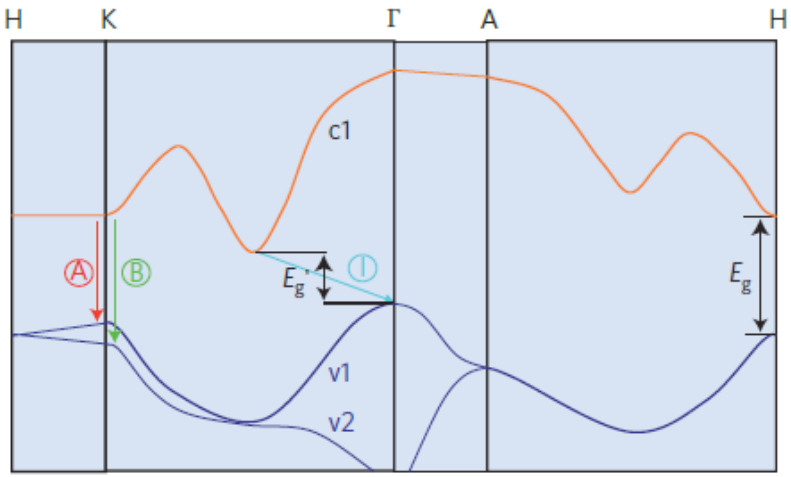


Figure 2.4: Simplified electronic structure of group 6 TMDs showing the co-existence of the split direct band gap and the indirect band gap.[10]

Although there is an indirect to direct band gap transition when the number of layers decrease, it is known that even in bulk TMDs, the direct and indirect gaps coexist.[15] The direct excitonic transitions are characterized by an A-B excitonic pair.[16] Different electronic structure models have been proposed to explain the A-B excitonic pair and it has been established that the direct transitions arise from d-d transitions and occur between d_{xy} and $d_{x^2-y^2}$ states of the valence band, that are split by interlayer interactions and spin-orbit coupling, and d_{z^2} states.[7,16] The valence splitting of WS_2 is larger than that of MoS_2.[7] As it was shown that the electronic structure of WS_2 is significantly affected by the number of layers, it is expected that the thickness of the material should cause a change in the band gap of the material. When the thickness of the material decreases, the valence band maximum moves downward (lower energy) and the conduction band minimum moves upwards (higher energy), hence an increase in the band gap energy.[7] As a layered material, it is expected that the dimensionality of WS_2 is two dimensional; however, it has been shown from various results that WS_2 is able to form 0D to 3D structures.[3] The dimensionality is based on the spatial quantum confinement in one, two or three dimensions.[3,17] 0D WS_2 are typically spherical quantum dots or inorganic fullerene-like materials where all three dimensions are smaller than twice their exciton Bohr radius. 1D WS_2 structures such as nanofibers have quantum confinement in two dimensions. 2D WS_2 such as nanosheets experience quantum confinement in one dimension.[3] It has been found that lateral quantum confinement in WS_2 enhances its luminescence efficiency and widens the band gap of the material.[18]

2.4 Raman spectroscopy of WS_2

Since the start of research into 2D layered materials, Raman spectroscopy has been employed to give insight into the crystal and electronic structure, lattice vibrations and even the sheet thickness of the materials.[2] Because of the layered nature of these materials and the van der Waals forces that hold the layers together, these materials can be easily exfoliated into fewer layers. Most of the Raman measurements done on WS_2 were done on exfoliated sheets. In this work, the WS_2 sheets are obtained from colloidal synthesis, hence the correct assignment of Raman peaks is important in order to correctly deduce the crystal and electronic structure as well as to correctly assign the crystal vibrations of WS_2 synthesized via the colloidal synthetic route. The crystal structure of WS_2 is well known. The point group symmetry of WS_2 however, changes depending on the number of layers present in the material. Bulk WS_2 has D_6h symmetry, while the fewer layered WS_2 with an odd number of layers has D_3h symmetry and the even numbered layers have D_3d symmetry.[2,19] This change in symmetry with the layer number or sheet thickness, means that the Raman modes will change with the sheet thickness, but has also sometimes led to the incorrect assignment of Raman modes. [19]

WS_2 has 18 vibrational modes at the centre of the hexagonal Brillouin zone, However, only 4 of those modes are Raman active. These modes are $A_{1g}(\Gamma)$, $E_{1g}(\Gamma)$ and two $E_{2g}(\Gamma)$ modes. The E_{1g} mode is forbidden in the backscattering configuration.[2,16] WS_2 also shows multi-phonon modes or second order modes, depending on the laser excitation energy used to probe the material.[20] These modes usually appear at frequencies lower than 350 cm^{-1}. It has been shown that the multi-phonon peaks disappear when the laser energies increase.[16] The E^1_{2g} mode is an in-plane vibrational mode where the W and S atoms vibrate horizontally in opposite directions as shown in Figure 2.5 (a). The A_{1g} mode is an out-of-plane vibration where the two S atoms move in opposite directions vertically (Figure 2.5 (b)). The A_{1g} mode is observed at 420 cm^{-1} in bulk WS_2 and the E^1_{2g} mode is observed at 356 cm^{-1}. The E^2_{2g} mode appears at very low frequencies because it denotes a shear mode that consists of the vibration of two rigid layers

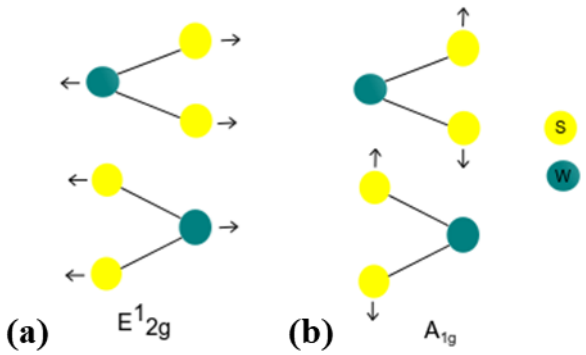


Figure 2.5: Representations of the (a) $E^1_{2g}(\Gamma)$ and (b) $A_{1g}(\Gamma)$ Raman modes of WS_2.

When the laser energy is resonant with the excitonic energies of the material, interesting features appear in the Raman spectra, such as the observation of a longitudinal acoustic mode 2LA(M) at 351 cm^{-1}. The longitudinal acoustic mode (LA) occurs at the M-point in the hexagonal Brillouin zone and it refers to the in-plane collective vibration of the atoms in the lattice.[20] It has been likened to sound waves. This phonon can also be described as periodic expansions and compressions of the lattice in the direction of propagation.[20] It has been found that the E^1_{2g} and 2LA(M) mode frequently overlap[4] depending on the laser wavelength used. While others have assigned the peak at 350 cm^{-1} to E^1_{2g} instead of the 2LA(M) mode for exfoliated WS_2 nanosheets.[22] The frequencies and intensities of the Raman modes are frequently reported as being useful tools to use in the determination of the number of layers or thickness of WS_2. Several theories have been suggested from various studies using the three visible first order modes A_{1g}, E^1_{2g} and 2LA(M). For WS_2 of 1-4 layers, the first order E^1_{2g} and A_{1g} mode appear at 356 cm^{-1} and 417cm^{-1} respectively[23] while for bulk WS_2 the E^1_{2g} mode frequency decreases to 355 cm^{-1} and the frequency of the A_{1g} mode increases to 420 cm^{-1}.[20,23,24] The second order 2LA(M) mode appears at 350 cm^{-1}, but shows no significant frequency shifts when the number of layers change.[23]

The increase in the frequency of the A_{1g} mode as the layers increase is attributed to the weak interlayer interactions caused by van der Waals forces between neighbouring layers.[20,24] The A_{1g} mode is an out-of-plane mode that involves the stretching and compressing of the S-atoms. With a monolayer, there is no interlayer interaction with the S atoms of neighbouring layers. When layers are added, the van der Waals interactions act like springs and then when the S atoms compress and expand simultaneously, there is a stronger interlayer interaction which leads to an increase in the frequency of this mode.[20,24] The increase in the frequency of

the A_{1g} mode is also said to be caused by the increase of the restoring force acting on the atoms as the layers increase.[25] This indicates that as the number of layers increase, the collective force that acts on the atoms due to the relaxation of the layers is increased.[25] The decreased frequency of the E^1_{2g} mode is caused by stronger dielectric screening of Coulomb interactions between effective charges in the material when the material is thicker.[20,23]

The changes in the frequencies of these modes mean that the separation between them also changes. It has been found that the distance between the A_{1g} and E^1_{2g} increases from 62 cm^{-1} to 66 cm^{-1} as the number of layers increase, because of the blue shift of the A_{1g} mode.[26] At times, when the E^1_{2g} and 2LA mode cannot be differentiated due to overlap, the average of the frequencies is taken and subtracted from the A1g frequency in order to obtain a relative separation.[26] The overlap of these two modes often causes an incorrect estimation of the thickness of the material. The intensities of the three main modes have also been used to estimate the number of layers in the material. Park *et al.* used the intensity ratio between the E^1_{2g} and the A_{1g} mode and deduced from their results, that the ratio decreased with the number of layers. The decrease means is attributed to the decrease of the A_{1g} mode intensity, due to weak interlayer coupling.[23] However, Berkdemir *et al.* showed that the thickness of the nanosheets has no significant effect on the intensity ratio between the E^1_{2g} and A_{1g} modes.[20] This discrepancy could be caused by the difference in the laser wavelengths that were used in the separate studies. Some reports have shown that the intensity of the 2LA(M) mode can be used to determine or estimate the number of layers in WS_2. It was found that the A_{1g} mode intensity increases when the layers increase while that of the 2LA(M) mode decreases when the layers increase.[20] The increase in the intensity of the A_{1g} mode is also attributed the interlayer interactions increasing as the layers increase, as mentioned before.[20,24] In order to use the intensities in the estimation of layer number, usually the Raman modes with the strongest intensities at a specific excitation wavelength are chosen. For the resonant excitation wavelength of 514 nm, the 2LA(M) and A_{1g} modes are strongest. The intensity ratio ($I_{2LA}/I_{A_{1g}}$) between the two is used as a fingerprint for layer number. It has been reported that for monolayer WS_2, this ratio is always above 2.[20] It has also been found that vibrations occur between the S-W-S layers. These layers can also be denoted as rigid layers and these layers also vibrate with respect to each other, giving rise to shear (S) and layer-breathing (LB) modes. These modes have been used to obtain the shear modulus of TMDs, as well gaining information on the stacking orders of TMDs that were mentioned earlier in the

description of the crystal structure of WS_2.[2] This shows that Raman spectroscopy is a valuable tool to probe the structure of TMDs. The S and LB modes are found at low frequencies (± 20 cm-1).

2.5 Synthesis of TMDs

The synthesis of TMDs consists of two main categories: a top-down and bottom-up synthesis.

2.5.1 Top-down synthesis

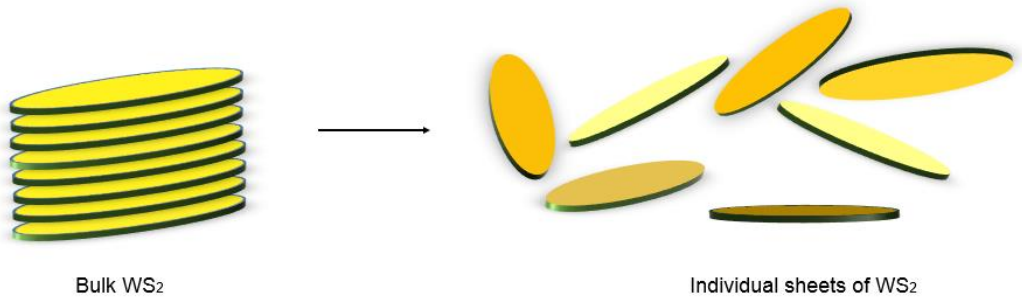


Figure 2.6: Diagram depicting the basic mechanism of top-down synthesis of transition metal dichalcogenides.

Top-down synthesis involves exfoliation of bulk TMD crystals into nanosized particles and is usually in the form of the following procedures:

(i) Mechanical exfoliation

Mechanical exfoliation is one of the first and most widely used top-down methods for the production of WS_2 monolayers. It relies on the weak van der Waals forces between the stacked WS_2 layers. The Scotch-tape method, as it's commonly referred to, involves using adhesive tape to peel off the layers from a bulk crystal until only one layer is left which can be transferred to the desired substrate.[8,12] This method produces high-quality nanosheets but is time-consuming and low yielding. A method of mechanical exfoliation using gold was developed where a gold film on the tape is used to peel off the layers. It proved more efficient in that it produced larger nanosheets. However, gold is an expensive metal that is usually discarded after exfoliation which is not economically feasible. The time it takes to produce these nanosheets does not change and the yield is still not satisfactory.[8,12] Other new adaptations for mechanical exfoliation were developed such as nano-mechanical exfoliation,

as shown in Figure 2.7, which uses a sharp tungsten probe to peel off the individual layers from a larger crystal.[3]

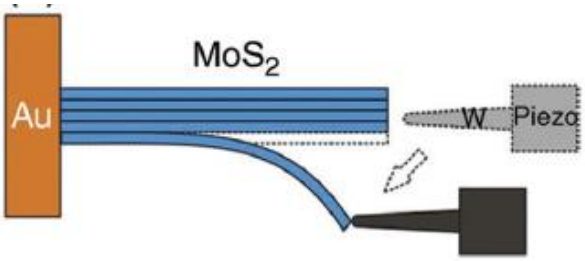


Figure 2.7: Nano-mechanical exfoliation using tungsten probe.[3]

The biggest drawback of this method is that it is labour intensive and ultimately produces a very poor yield of WS_2 nanosheets. The nano-mechanical exfoliation technique also requires complex and expensive equipment for low yields of products.[3] It is therefore not a suitable method for large scale production of WS_2, but is commonly used for proof-of-concept applications and demonstration of high-performance devices.[8,10,12]

(ii) Liquid phase exfoliation

Liquid phase exfoliation (LPE) is a better exfoliation method than the mechanical route because it produces higher yields of nanosheets.[10] This method typically involves sonication of the WS_2 bulk crystal in various solvents. The main consideration in this method involves the solvent used. The solvent not only has to overcome the cohesive energy between the layers during sonication, but also has to be able to prevent the exfoliated nanosheets from aggregation. Therefore, surfactant molecules, such as sodium cholate, with comparable surface energy to the material are usually used.[10]Although the yield is higher compared to mechanical exfoliation, sonication of the bulk crystal causes breakage of the nanosheets that are already exfoliated. There is no control over the size of the nanosheets or the thickness of the nanosheets. The process of sonicating the bulk crystals is also time-consuming.

(iii) Chemical exfoliation

Chemical exfoliation mainly involves using lithium ions as an intercalating agent. In this method, a solvent is used together with a lithium source such as n-BuLi where the lithium ions intercalate between the layers and form Li_xWS_2. The lithium intercalated material is then exposed to water which reacts with the Li, evolving H_2 gas which causes the exfoliation of the sheets.[12] The lithiation of the material, however, leads to a rearrangement of the lattice

which causes a phase transition from the 2H phase to the metallic 1T phase.[13] It has been found that the yields obtained for this method are very high. The drawbacks are that this method is carried out for long periods of time, with highly explosive lithium compounds. Also, there is the challenge of controlling the exfoliation as the lithium can also cause the formation of LiS_2.[10]

2.5.2 Bottom-up synthesis

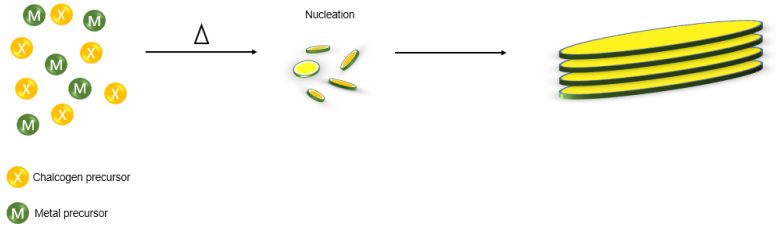


Figure 2.8: Diagram depicting basic bottom-up synthesis of transition metal dichalcogenides.

Bottom-up synthesis involves growing TMD nanocrystals from suitable chalcogen and transition metal precursors. The difficulty of bottom-up synthesis lies in the understanding of the energetics and control over the kinetics of the reactions. Because even though there are an infinite number of metal and chalcogen precursors that are available, it has been difficult to understand the energetics and kinetics involved in the formation of two-dimensional particles.[27] TMDs are naturally layered materials in their bulk form and once thinned to nanometre dimensions, the nanosheets become more unstable. A good understanding of the control over the growth of these nanoparticles will help to develop methods that favour the formation of nanosheets instead of bulk structures. This is the importance of research into the bottom-up synthesis of TMDs. To understand what conditions are best suited for the selective growth of nanosheets or whatever other preferred morphology or dimensionality of the TMDs that is required. The main bottom-up techniques include gas phase synthesis, hydro and solvothermal synthesis, microwave, and colloidal synthesis.

(i) Gas phase synthesis

Gas phase synthesis is the most widely used synthetic bottom-up technique for TMDs. In its most basic form, this method involves two main types of reactions:

(a) Vapour phase deposition, where gaseous metal and chalcogen precursors react and the product is deposited onto a substrate. This is a simple technique where the metal and chalcogen precursors are reacted in gas phase and the TMD monomers are deposited onto a substrate as a large area thin film, however it has been found to form polycrystalline thin films instead, with uncontrollable thickness .[28] This method requires very high temperatures and low pressures to be able to volatilize the metal and chalcogen precursors. Many considerations have to be taken in this case especially with regard to substrate interactions. The substrate used has to be flat and chemically inert so as to not react with the TMD monomers that are deposited on it. Lattice mismatch between the substrate and TMD lattice have to be minimized while van der Waals interactions must be promoted between the substrate and TMDs so that the resultant nanosheet can be easily peeled off.[27]

(b) The direct sulfurization of metal or metal oxide thin films by a gaseous chalcogen precursor. This method, although similar to the direct deposition mentioned above, is different in that it eliminates the transport of TMD monomers within the reaction chamber to be deposited.[29] It involves gaseous sulphur vapours flowing over a metal or metal oxide thin film, sulfurizing them into MS_2. This method is a relatively simple method of producing TMDs, but also comes with a few limitations. In order to control the thickness of the MS_2 nanosheets, precise control of the metal or metal oxide thin film thickness is required. It has been found that obtaining uniformity of the pre-deposited thin film is difficult which results in MS_2 nanosheets with non-uniform thickness and high grain and defect densities which severely hinders its electronic properties.[27,28] Zhan *et al.*,[30] found that when using metal films, the sulfurization doesn't always go to completion, leaving unreacted metal atoms within the sample which ended up with MoS_2 with metallic electronic properties. The switch from metal to metal oxide thin films was done in order to ensure that the products are completely semiconducting and have no metallic properties from unreacted metal.[28] Song *et al.*,[31] developed atomic layer deposition (ALD) where precise control of the metal oxide film thickness could be controlled in order to achieve uniformity. However, the suitable precursor used to form the WO_3 films is not readily available, which makes this method not very accessible and the standard inert and hydrophobic substrates used for this synthesis do not efficiently initiate WO_3 growth.

Apart from the two main vapour deposition methods, other adaptations of these methods have been used such as metalorganic CVD (MOCVD), where low vapour pressures of organometallic precursors are used.[32] Thermal decomposition of thiosalts has also been done

by decomposing precursors such as ammonium thiomolybdate $(NH_4)_2MoS_2$ into MoS_2 at elevated temperatures. The resultant products usually have sulphur deficiencies due to oxygen contamination. Further annealing at temperatures as high as 1000 ℃ in a sulfur-rich environment is necessary to reduce the oxygen defects.[33] Another method is the vaporization of TMD powders and recrystallizing them onto a substrate to form highly crystalline flakes of TMDs[34] that are not uniform due to the random growth of the flakes onto the substrate. The advantages of gas phase synthesis of TMDs are that the nanosheets produced are of very high quality so that they are compatible with existing technologies and the synthetic methods are scalable compared to mechanical exfoliation methods.[27] The resultant nanosheets are also of large area and this method, if developed properly, is able to produce wafer-scale 2D TMD nanosheets .[28]

The major drawbacks of the gas phase synthetic methods are that it requires the use of temperatures as high as a 1000 ℃ and at times the use of harmful gases such as H_2S. For instances where precise control of the thickness of the TMDs is important, CVD is not very suitable as there is no control over the growth of the particles. Other drawbacks include the difficulty of obtaining metal or metal oxide thin films of a thickness exactly to what is required of the TMDs and the use of generic substrates such as SiO_2. MS_2 films are deposited onto the substrates during synthesis and need to be peeled off and transferred to target substrates which cause breakage of the films.

(ii) Solution based syntheses

Solution based syntheses hold the advantage of being high yielding methods that can be scaled up and optimized for mass production. Also, these methods are flexible in that many parameters can be varied to fine tune the types of TMDs obtained.[35] Various morphologies with different properties can be produced with a variety of precursors or capping ligands or reaction temperature.

(a) Hydro/solvothermal method

This synthetic method involves the reaction of tungsten and sulphur precursors in an aqueous or non-aqueous solution in an autoclave at elevated temperatures and pressure for several hours. Hydro- and solvothermal methods are mostly similar, with the same kinds of precursors being used for both. The only difference is that solvothermal synthesis uses high boiling point organic solvents instead of water. The main advantage of hydro/solvothermal

methods are the lower temperatures used (100-240℃) compared to CVD.[36] The main drawbacks of these two methods are the long reaction times which range from 10-48 hours and the requirement of high pressures. The flexibility of this method means that by varying different parameters, different types of TMDs can be obtained. In the case of work done by Chakravarty *et al.*, large microrods and particles were obtained by varying the tungsten precursor.[37] Large mesoporous WS_2 particles were obtained when cetrimonium bromide (CTAB) was added to the hydrothermal reaction mixture.[38]

(b) Microwave-assisted synthesis

The microwave-assisted synthetic method is a fast and energy efficient way to produce nanoparticles. It involves mixing the metal and chalcogen precursors in a solvent and irradiating them with microwaves for a few minutes. The biggest advantage to this method is the fast reaction time and this method has been used widely for the synthesis of metal and metal oxide nanoparticles.[36] However, this method is not widely used for the synthesis of layered TMDs. Some work has been done to synthesize WS_2 using this method. Chaturvedi *et al.* developed a solventless plasma-assisted microwave synthesis of WS_2 which is like a combination of CVD and microwave synthesis. This method produced large hexagonal WS_2 nanoplates.[39] The drawback here was the longer reaction time but also a complex reaction set-up that required a vacuum. The same type of method was used to selenize WO_3 and MoO_3 to produce WSe_2 and $MoSe_2$ by Chen *et al.* who found that by varying the thickness of the metal oxide film on the substrate, they could influence the growth orientation of the layers.[40] Just like colloidal synthesis, various morphologies and types of TMDs can be produced via this method. Liu *et al.* produced inorganic fullerene-like WS_2 nanoparticles by incorporating polypyrrole nanofibers in the reaction medium.[41] WS_2 nanowires were obtained by Panigrahi *et al.*, however, the microwave part of the synthesis only yielded an intermediate that required annealing at 750 ℃ for 1.5 hours [42] which loses the energy efficiency associated with microwave synthesis. Other morphologies such as microrods,[37] nanosheets, nanocones, and nanoworms[43] were obtained by varying parameters such as the concentrations of the precursors used.

(c) Colloidal synthesis

This method also involves the reaction of metal and chalcogen precursors in a high boiling point organic solvent which also acts as a capping ligand. The reactions are usually carried

out under an inert atmosphere at elevated temperatures (±300℃). The reaction times are much shorter compared to the very long reaction times of hydro/solvothermal method. While the exfoliation methods suffered from non-scalability, colloidal synthesis is a method that is scalable and usually produces high yields of nanoparticles.[8] The use of capping or stabilizing ligands means that the surface chemistry of the nanoparticles is modified in such a way that the nanoparticles can be dispersed in various media for specific applications.[1] The capping ligands also lend in the stabilization of the particles, preventing agglomeration. One of the biggest advantages of colloidal synthesis is in its flexibility. The ability to change different reaction parameters in order to tune the types of TMDs obtained as well as their properties. This is what makes colloidal synthesis one of the most studied synthetic procedures for nanoparticles[44] and why it is the method of choice in this study.

Colloidal TMDs have a tendency to form nanostructures and flower-like morphologies, to minimize surface energies. Colloidal methods to produce TMD nanosheets with precisely controlled, size, shape, uniformity and layer thickness are not very common. There are many reaction parameters that influence the morphology of TMDs such as temperature, reactant concentration, the rate of decomposition of the precursors and the types of capping ligands used.[8] Colloidal synthesis poses a few challenges such as the difficulty of isolating nanosheets from solution, the difficulty in preventing restacking of the nanosheets and also the difficulty of obtaining flat nanosheets from a continuously stirred reaction medium. Although colloidal synthesis is a flexible technique for the synthesis of nanoparticles, understanding how these nanoparticles are formed has been a difficult topic as no theory or model exists that is able to fully describe or predict how the nanoparticles will evolve within a set of parameters.[45]

2.6 Colloidal growth mechanisms

There are two main colloidal growth mechanisms that attempt to explain how nanocrystals grow: The classical nucleation theory (CNT) and Lamer's theory. The classical nucleation theory states that a thermodynamic system tends to minimize its Gibbs free energy.[44] Therefore during colloidal synthesis, when nucleation begins, the Gibbs free energy increases as the monomers aggregate to form bigger units. The Gibbs energy continues to increase until the monomers reach the critical radius (r_c). The critical radius is the radius of the nuclei that prevent dissolution of the nuclei. It is also at the stage where the free energy is at its

maximum. Once the nuclei reach the critical radius, they begin to form stable nuclei. The free energy proceeds to decrease from there as the stable nuclei grow as shown in Figure 2.9. The CNT, however only describes the nucleation part of the process. The growth part is described using separate processes.[45]

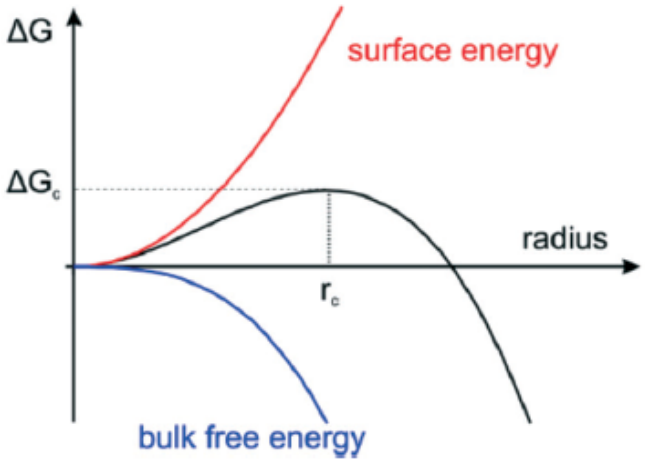


Figure 2.9: Diagram of the classical nucleation theory showing the dependence of the free energy (ΔG) on the radius (r) of the nuclei.[44]

Lamer incorporated the CNT into his theory, but also proposed separation between the nucleation and particle growth phases. Lamer showed that as the precursors are heated, monomers begin to form. The concentration of monomers [M] increases until it reaches super-saturation or critical nucleation [Mc]. Once nucleation of nanoparticles starts, the [M] begins to decrease because as the nanoparticles form, the monomers are rapidly consumed. Nucleation eventually stops when the monomer concentration drops below the equilibrium monomer concentration [Ma], which is the concentration required to prevent dissolution of very small particles. Once the monomer concentration is below [Ma], the very small particles that have a radius less than the critical radius (r_c) re-dissolve and participate in the growth of the larger, more stable nuclei.[45,46] Having these theories in mind, it can be inferred, especially with regards to the particle size distribution, what effect different parameters will have on the resultant nanoparticles. Parameters such as heating rate, growth temperature, precursor type, and concentration as well as capping ligands[44], some of which will be discussed in later chapters.

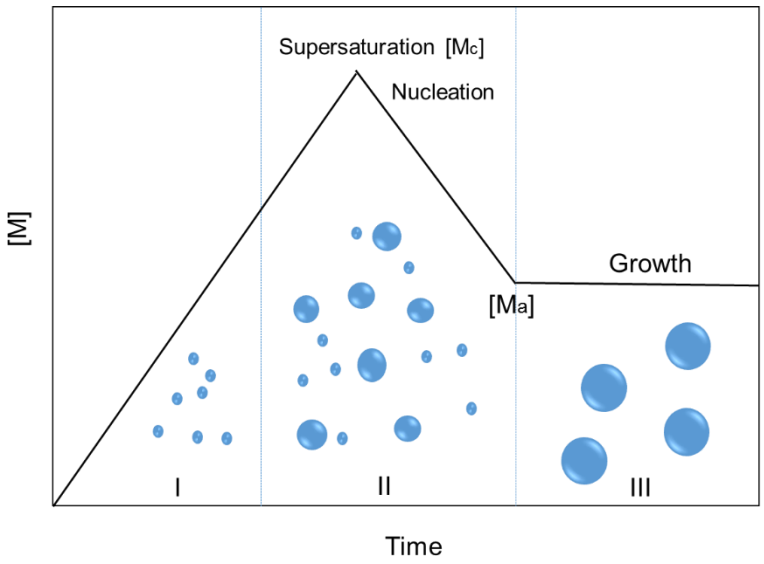


Figure 2.10: Diagram showing the separation between nucleation and growth based on Lamer's theory.

When it comes to the growth of anisotropic materials such as nanosheets, kinetics plays a role in the growth mechanisms. Within colloidal synthesis, anisotropic materials can be achieved by the use of various capping ligands.[47] The capping ligands have been shown to be able to selectively stabilize certain crystal facets which cause them to grow at different rates, hence causing anisotropic growth of the nanoparticles. Due to the flexibility of the colloidal synthetic method, TMDs with varying morphologies have been synthesized. From nanosheets to nanoflowers, nanospheres and even microboxes.[3] Nanomaterials can be classified into categories: nano-objects and nanostructures. Nano-objects are materials that have one external dimension at the nanoscale, while nanostructures are materials that are usually larger than the typical nanoscale materials, but are made up of nanoscale internal structures. For example when individual nanosheets aggregate to form micro flowers. These are also classified as hierarchical nanostructures.[48]

2.7 Application of WS_2 as a counter electrode in dye-sensitized solar cells

In solar cells, WS_2 has the capability to function as the active semiconductor material or as the electrodes that capture the generated charge carriers. Dye-sensitized solar cells (DSSCs) were first demonstrated by O'Regan and Grätzel in 1991 as a cheaper alternative to silicon photovoltaic (PV) cells.[49] Over the years, as research into DSSCs increased, these types of solar cells have shown to have several advantages which make them a promising third generation PV technology. DSSCs are easy to prepare, have low production and

environmental costs. They have shown enhanced performance in outdoor conditions and have also been found to outdo silicon-based solar cells in indoor applications.[50] High temperatures and vacuums are not necessary for the fabrication of these cells, which also leads to the lowered production costs. These cells are bifacial so they capture light from all angles, making them very efficient.[50] A basic DSSC consists of three main components: a working electrode (TiO_2) sensitized by an organic dye, an electrolyte solution (LiI and I_2) and a counter electrode (Pt)[51] as shown in Figure 2.11.

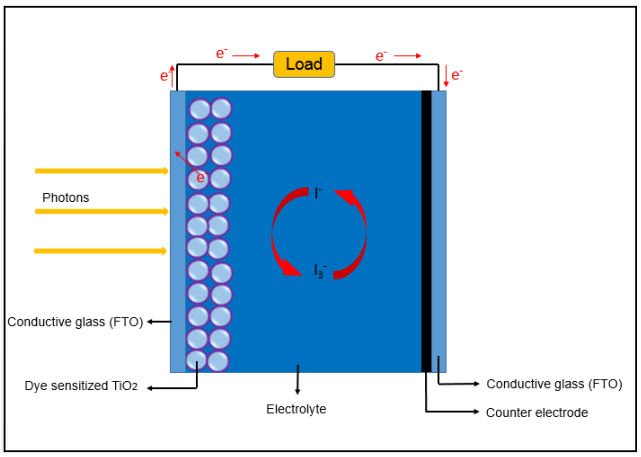


Figure 2.11: Diagram of a basic dye-sensitized solar cell.

TiO_2 is a wide-bandgap semiconductor and does not absorb visible light efficiently, which is the reason for its sensitization with visible-light sensitive dye. The dye assists the TiO_2 to absorb visible light more efficiently.[50] The electrolyte acts as an electron donor that rapidly donates electrons into the oxidized dye, to regenerate the dye or return the dye to its ground state. The basic operation of the DSSC starts with absorption of photons by the sensitizer dye. The photons excite the electrons in the dye and the dye further donates electrons into the conduction band of the TiO_2 which causes the dye to be oxidized. The electrons travel to the counter electrode through the external circuit. The oxidized dye is replenished by injection of electrons from the electrolyte and I_3^- is oxidized to I^-. The electrons in the counter electrode then regenerate the electrolyte by reducing the iodide to the triiodide.

WS_2 will be used as a replacement of platinum as the counter electrode (CE). Platinum has shown high photoelectric conversion efficiency (PCE) as a CE, however, platinum is an expensive and scarce noble metal which hikes up the production costs of the DSSCs. WS_2 has been shown to have good conductivity, electro-catalytic capabilities and is relatively

inexpensive. As a CE, WS_2 will act as a catalyst, promoting the reduction of the oxidized electrolyte which will result in the regeneration of the sensitizer dye. It will also collect electrons from the external circuit, returning them back into the cell's circulation.[50] Cyclic voltammetry is the electrochemical method that is used to evaluate the electrochemical catalytic activity of the counter electrode. A three-electrode cell consisting of the working electrode, reference electrode, and the counter (auxiliary) electrode is the basic set-up of the cyclic voltammetry measurements. Potential will be swept at a constant rate while the resultant current is observed. For the iodide/triiodide redox couple, 2 peak currents are usually observed (Figure 2.12) that correspond to the following reactions:

$I_3^- + 2e^- \rightarrow 3I^-$ (1)

$3I_2 + 2e^- \rightarrow I_3^-$ (2)

The first reaction has been found to have the biggest influence on the performance of the DSSCs.[52]

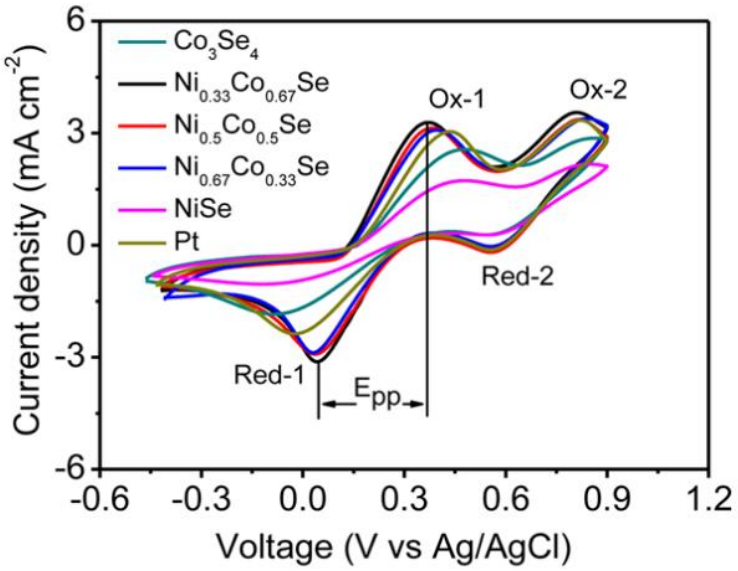


Figure 2.12: Cyclic voltammograms showing the two oxidation and reduction peaks associated with the I^-/I_3^- electrolyte.[53]

Several different transition metal chalcogenide materials have been used as substitutes for platinum as counter electrodes in DSSCs. Cobalt sulphides of different compositions have been used and even CoS/rGO composites. These have achieved photoelectric conversion efficiencies (PCE) between 6.5 and 9.4%.[49,54]From the work that was done on MoS_2 and WS_2, researchers have found that these materials have good PCE, even more than that of platinum. Edge oriented WS_2 has had the highest PCE of 8.85%, where the PCE of platinum

was 7.2%.[55] The edge orientation of WS_2 is important as it has been shown to be more catalytically active than the basal planes of the nanosheets. MoS_2 nanofilms and other WS_2 nanomaterials showed efficiencies of 8.3%[56] and 7.73%[57] respectively.

2.8 References

1. J. H. Han, S. Lee, and J. Cheon, *Chem. Soc. Rev.*, 2013, **42**, 2581–2591.
2. X. Zhang, Q. H. Tan, J. Bin Wu, W. Shi and P. H. Tan, *Nanoscale*, 2016, **8**, 6435–6450.
3. M. Samadi, N. Sarikhani, M. Zirak, H. Zhang, H. L. Zhang and A. Z. Moshfegh, *Nanoscale Horiz.*, 2018, **3**, 90–204.
4. U. Wurstbauer, B. Miller, E. Parzinger, Z. Lin, B. R. Carvalho, E. Kahn, M. O. Brien, N. Mcevoy, C. Motta, F. Wang, I. A. Kinloch, D. Wolverson, R. Tenne, A. Zak and E. O. Connell, *2D Mater.*, 2016, **4**, 015007.
5. X. Li, A. Tang, J. Li, L. Guan, G. Dong, and F. Teng, *Nanoscale Res. Lett.*, 2016, **11**, 1–7.
6. X. Zhou, J. Jiang, T. Ding, J. Zhang, B. Pan, J. Zuo and Q. Yang, *Nanoscale*, 2014, **6**, 11046–11051.
7. C. Xia and J. Li, *J. Semicond.*, 2016, **37**, 021001.
8. J. S. Ponraj, Z. Xu, S. Chander, F. Wang, Z. Wang and L. Wang, *2D Mater*., 2016, **3**, 042001.
9. C. Cong, J. Shang, Y. Wang and T. Yu, *Adv. Opt. Mater.*, 2018, **6**, 1–15.
10. M. Chhowalla, H. S. Shin, G. Eda, L. Li, K. P. Loh and H. Zhang, *Nature Chemistry*, 2013, **5**, 263-275.
11. S. Manzeli, D. Ovchinnikov, D. Pasquier, O. V Yazyev and A. Kis, *Nat. Rev. Mater*., 2017, **2**, 17033.
12. Q. H. Wang, K. Kalantar-Zadeh, A. Kis, J. N. Coleman and M. S. Strano, *Nat. Nanotechnol.*, 2012, **7**, 699–712.
13. D. Xu, Y. Zhu, J. Liu, Y. Li, W. Peng, G. Zhang, F. Zhang and X. Fan, *Nanotechnology*, 2016, **27**, 385604.
14. W. Tang, S.S. Rassay and N.M. Ravindra, Madridge J. Nano Tech., 2017, **2**, 59–65.
15. W. Zhao, Z. Ghorannevis, L. Chu, M. Toh, C. Kloc, P. Tan and G. Eda, *ACS Nano*, 2013, **7**, 791-797
16. C. Sourisseau, F. Cruege, and M. Fouassier, *Chemical Physics*, 1991, **150**, 281-293.

17. P. Miró, J. H. Han, J. Cheon, and T. Heine, *Angew. Chem. Int. Ed*., 2014, **55**, 12624–12628.
18. A. Bayat and E. Saievar-iranizad, *J. Lumin.*, 2017, **185**, 236–240.
19. H. Terrones, E. Del Corro, S. Feng, J. M. Poumirol, D. Rhodes, D. Smirnov, N. R. Pradhan, Z. Lin, M. A. T. Nguyen, A. L. Elías, T. E. Mallouk, L. Balicas, M. A. Pimenta and M. Terrones, *Sci. Rep.*, 2014, **4**, 4215.
20. A. Berkdemir, H. R. Gutiérrez, A. R. Botello-Méndez, N. Perea-López, A. L. Elías, C.-I. Chia, B. Wang, V. H. Crespi, F. López-Urías, J.-C. Charlier, H. Terrones and M. Terrones, *Sci. Rep.*, 2013, **3**, 1755.
21. N. Razgoniaeva, L. Carrillo, P. Moroz, P. Adhikari, P. Yadav, D. Khon and M. Zamkov, *Chem. Mater*., 2016, **28**, 2823-2833.
22. G. Pagona, C. Bittencourt, R. Arenal and N. Tagmatarchis, *Chem. Commun.*, 2015, **51**, 12950–12953.
23. J. Park, W. Lee, T. Choi, S. H. Hwang, J. M. Myoung, J. H. Jung, S. H. Kim, and H. Kim, *Nanoscale*, 2015, **7**, 1308–1313.
24. A. Molina-Sánchez and L. Wirtz, *Phys. Rev. B - Condens. Matter Mater. Phys.*, 2011, **84**, 1-8.
25. T. Georgiou, H. Yang, R. Jalil, J. Chapman, K. S. Novoselov and A. Mishchenko, *Dalt. Trans.*, 2014, **43**, 10388–10391.
26. P. Kumar, H. Abuhimd, W. Wahyudi, M. Li, J. Ming, and L.-J. Li, *ECS J. Solid State Sci. Technol.*, 2016, **5**, 3021–3025.
27. J. R. Brent, N. Savjani and P. O'Brien, *Progress in Materials Science*, 2017, **89**, 411–478.
28. Y. Shi, H. Li and L. Li, *Chem. Soc. Rev*., 2015, **44**, 2744–2756.
29. Y. Guo, X. Fu, and Z. Peng, *Journal of Nanomaterials*, 2017, **2017**, 1-6.
30. Y. Zhan, Z. Liu, S. Najmaei, P. M. Ajayan and J. Lou, *Small*, 2012, **8**, 966–971.
31. J. Song, J. Park, W. Lee, T. Choi, H. Jung, C. W. Lee, S. Hwang, J. M. Myoung, J. Jung, S. Kim, C. Lansalot-matras and H. Kim, *ACS Nano*, 2013, **7**, 11333–11340.
32. N. Zink, H. A. Therese, J. Pansiot, A. Yella, F. Banhart and W. Tremel, *Chem. Mater*., 2008, **20**, 65-7.
33. K. Liu, W. Zhang, Y. Lee, Y. Lin, M. Chang, C. Su, C. Chang, H. Li, Y. Shi,H. Zhang, C. Lai and L. Li, *Nano Lett*., 2012, **12**, 1538-1544.
34. S. Jeong, D. Yoo, J. Jang, M. Kim and J. Cheon, *J. Am. Chem. Soc*., 2012, **134**, 18233.

35. R. Munoz-Espi, Y. Mastai, S. Gross and K. Landfester, *CrystEngComm*., 2013, **15**, 2175–2191.
36. J. Wang, G. Li and L. Li, *InTech*, 2016.
37. D. Chakravarty and D. J. Late, *RSC Adv*., 2015, **5**, 21700–21709.
38. S. V. P. Vattikuti, C. Byon and C. V. Reddy, *Mater. Res. Bull.*, 2016, **75**, 193–203.
39. A. Chaturvedi, A. Slabon, P. Hu, S. Feng, K. Zhang, R. Ramanujam and C. Kloc, *J. Cryst. Growth*, 2016, **450**, 140–147.
40. Y. Chen, H. Medina, S. Wang, T. Su, J. Li, W. Yen, K. Cheng, H. Kuo, G. Shen and Y. Chueh, *Chem. Mater*., 2016, **28**, 1147-1154.
41. Z. Liu, L. Zhang, R. Wang, S. Poyraz, J. Cook, M. J. Bozack, S. Das, X. Zhang and L. Hu, *Sci. Rep*., 2016, **6**, 22503.
42. P. K. Panigrahi and A. Pathak, *Sci. Technol. Adv. Mater*., 2008, **9**, 045008-045014.
43. H. Yan, J. Li, D. Liu, X. Jing, D. Wang and L. Meng, *CrystEngComm*, 2018, **20**, 2324–2330.
44. J. Polte, *CrystEngComm*., 2015, **17**, 6809–6830.
45. J. Van Embden, A. S. R. Chesman and J. J. Jasieniak, *Chem. Mater*., 2015, **27**, 2246-2285.
46. K. L. Sowers, B. Swartz and T. D. Krauss, *Chem. Mater*., 2013, **25**, 1351-1362.
47. N. D. Burrows, A. M. Vartanian, N. S. Abadeer, E. M. Grzincic, L. M. Jacob, W. Lin, J. Li, J. M. Dennison, J. G. Hinman and C. J. Murphy, *J. Phys. Chem. Lett*., 2016, **7**, 632-641.
48. J. Zhang, S. Liu, H. Liang, R. Dong and X. Feng, *Adv. Mater*., 2015, **27**, 7426–7431.
49. E. Singh, K. S. Kim, G. Y. Yeom and H. S. Nalwa, *RSC Adv*., 2017, **7**, 28234-28290.
50. J. Wu, Z. Lan, J. Lin, M. Huang, Y. Huang, L. Fan and G. Luo, *Chem. Soc. Rev*., 2017, **46**, 5975–6023.
51. S. Li, Z. Chen and W. Zhang, *Mater. Lett.*, 2012, **72**, 22–24.
52. D. Vikraman, S. A. Patil, S. Hussain, N. Mengal, H. Kim, S. Hoon, J. Jung, H. Kim and H. Joon, *Dyes and Pigments*, 2018, **151**, 7–14.
53. X. Qian, H. Li, L. Shao, X. Jiang and L. Hou, *ACS Appl. Mater. Interfaces*, 2016, **8**, 29486-29495.
54. S. Chang, M. Lu, Y. Tung and H. Tuan, *ACS Nano*, 2013, **7**, 9443–9451.
55. S. H. Ahn and A. Manthiram, *Adv. Energy Mater*., 2016, **6**, 1501814.
56. J. Liang, J. Li, H. Zhu, Y. Han, Y. Wang, C. Wang, Z. Jin, G. Zhang and J. Liu, *Nanoscale*, 2016, **8**, 16017–16025.

57. M. Wu, Y. Wang, X. Lin, N. Yu, L. Wang and L. Wang, *Phys. Chem. Phys. Chem*., 2011, **13**, 19298–19301.

Chapter 3

Synthesis of WS_2 nanostructures with various ratios of organic capping agents

3.1 Introduction

The flexibility of colloidal synthesis comes from the fact that nanoparticles can be modified by altering various reaction parameters. Capping agents are one of the important parameters that must be considered in colloidal synthesis. Due to their size, nanoparticles have much higher surface energy compared to bulk particles. Nanoparticles tend to agglomerate due to instability caused by the high surface energies.[1–3] Capping agents are molecules that bind onto the surface of the nanoparticles to stabilize the particles and prevent agglomeration. The binding of the capping agents occurs through van der Waals forces, chemisorption or hydrophobic interactions.[4] The surface chemistry of nanoparticles depends largely on the capping agents.[5] Because of the surface modifying effects of capping agents on the nanoparticles, the nanoparticles are able to be dispersed in various media and are made compatible with various solvents, hence providing the ability to tailor the nanoparticles to specific applications.[1,6,7] Some capping agents such as citrate and alkylamines have the additional role of reducing the metal ions in solution.[1,8]

Capping agents are also able to cause anisotropic growth of nanoparticles by selectively capping certain crystal facets.[3,9] The anisotropic growth comes from the differing affinities that the capping agents have to certain facets of the particles. The functional groups bind to the facets through dynamic adsorption and desorption. The facets for which they have the highest affinities will bind more strongly to the capping agents. The affinities are governed by the geometry of the atoms in that crystal plane.[3] During crystal growth, atom deposition on the strongly bound facets is limited, meaning the growth of these facets is slower than those that are weakly bound. In the end, the facets with the slow growth will be preserved and are the facets that will be exposed in the resultant nanoparticles.[10,11] The resultant shapes of the nanoparticles are consequently changed by the capping agents used as shown in Figure 3.1. The figure shows how using sodium citrate (Na_3CA) or polyvinyl pyrrolidone (PVP) as capping agents results in vastly different silver nanoparticle morphologies. This has been shown with various metal nanoparticles such as silver, platinum, and palladium to name a few.[10,12,13]

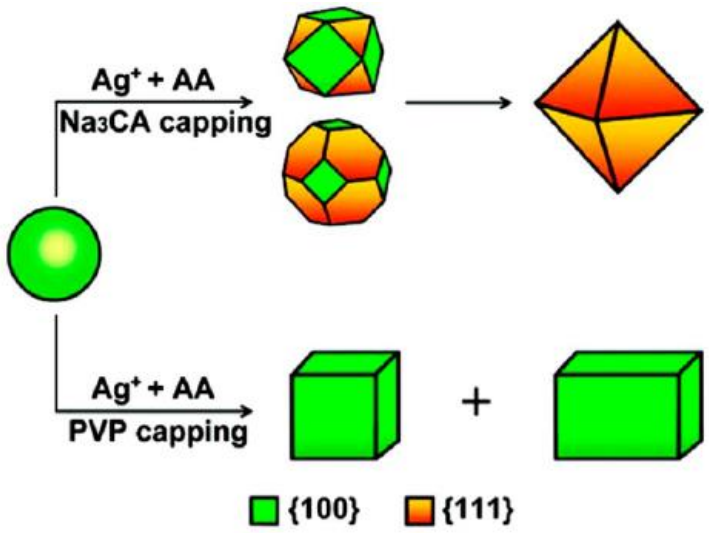


Figure 3.1: Schematic showing the preferential binding of capping agents to specific facets of silver nanoparticles.[14]

TMDs are naturally anisotropic materials and the effect of capping agents was mostly seen in the control of the number of layers in the nanosheets more than the control of the shapes of the sheets. An example was shown when oleic acid, oleylamine and oleyl alcohol were used to synthesize WSe_2 nanomaterials. It was found that using oleic acid caused the formation of monolayer WSe_2 and oleylamine resulted in few-layered WSe_2. This was attributed also to the affinity of the capping agents to the edge sites of the material.[15] Different types of molecules can be used as capping agents. From surfactants like cetrimonium bromide (CTAB) to organic molecules such as oleylamine and polymers such as polyvinyl alcohol (PVA) or polyethylene glycol (PEG).[1,16] In this study oleylamine, oleyl alcohol, oleic acid, and octadecene are used as organic capping agents for the synthesis of WS_2 nanomaterials. These molecules have the same chain length as well as a double bond in the chain. The double bond in oleylamine, oleic acid, and oleyl alcohol is situated between the 9^{th} and 10^{th} carbon in the chain, while that of 1-octadecene is situated between the 1^{st} and 2^{nd} carbon in the chain. The other difference between them being the head group as shown in Figure 3.2. Oleylamine has been shown to be an excellent capping and reducing agent,[17], therefore, it is used as the main capping agent while the other capping agents are used as co-capping agents. The use of co-surfactants is to determine how the other capping agents affect the morphology and thickness of the WS_2.

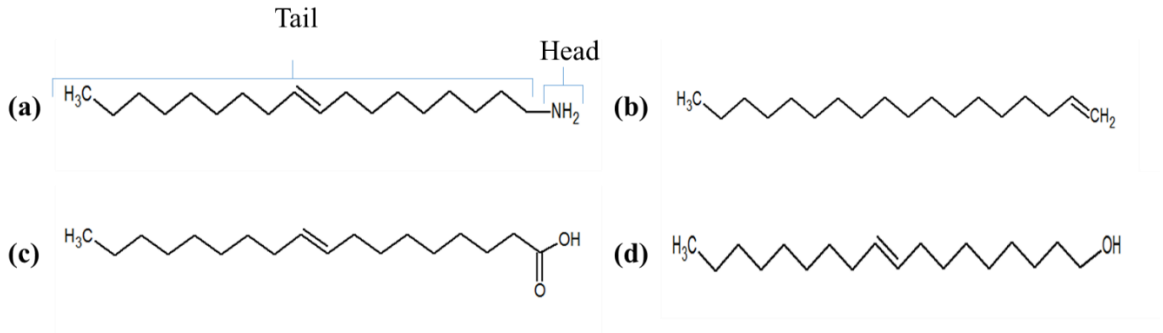


Figure 3.2: Capping agent molecules: (a) oleylamine, (b) 1-octadecene, (c) oleic acid and (d) oleyl alcohol.

3.2 Materials and method

3.2.1 Chemicals

Tungstic acid (H_2WO_4, 99%), thiourea ($CS(NH_2)_2$, 99%), oleylamine (70% technical grade), 1-octadecene (90% technical grade) , oleic acid (90% technical grade) and oleyl alcohol (85% technical grade). All chemicals were purchased from Sigma Aldrich South Africa.

3.2.2 Experimental procedure

Tungstic acid and thiourea in a 1:4 molar ratio were placed in a three-necked round bottom flask. Ratios of oleylamine with the other capping agents as shown in Table 3.1 were added to the flask. The mixture was purged with N_2 gas at room temperature while stirring for 20 minutes to eliminate any air in the reaction vessel. Thereafter the mixture was heated to 300℃ and held for two hours. The resultant black product was cooled to room temperature. The product was washed with equal parts ethanol and hexane and air-dried overnight.

Table 3.1: Table showing ratios of oleylamine to the other capping agents used in capping agent study

	Oleylamine	Oleic acid/ oleyl alcohol/ octadecene
0%	20 ml	0 ml
25%	15 ml	5 ml
50%	10 ml	10 ml
75%	5 ml	15 ml
100%	0 ml	20 ml

3.2.3 Characterization

Powder X-ray diffraction (PXRD) was carried out on the Bruker MeasSrv (D2-205530)/D2205530 diffractometer using CuKα radiation (λ 1.5406 Å) at 30 kV/30 mA. Raman spectroscopy was performed on a Horiba J-Y T64000 micro-Raman spectrometer. The excitation wavelength used for all samples was 514 nm. Fourier Transform Infrared (FT-IR) spectroscopy was performed on a Bruker Tensor 27 spectrometer. Transmission electron microscopy (TEM) was done on the FEI Technai T12 microscope with an accelerating voltage of 120 kV. Scanning electron microscopy and energy dispersive spectroscopy (EDS) was performed on the FEI Nova Nanolab 600 microscope. ^{1}H-NMR spectroscopy was performed on a Bruker spectrometer of 500 MHz. The UV-Vis absorption characteristics were measured with the Varian Cary Eclipse (Cary 50) UV-vis absorption spectrophotometer.

3.3 Results and discussion

3.3.1 WS_2 nanostructures synthesized with only oleylamine (OLA)

PXRD and Raman spectroscopy were used to probe the crystal structure of the material produced. The PXRD pattern in Figure 3.3 (a) shows distinct 2H-WS_2 reflections, matching to the PDF card number 00-084-1398. The pattern shows the (002) plane, which is attributed to the c-axis of the material. The presence of this plane indicates the layered structure of the WS_2 and the presence of more than one layer of WS_2.[18] The crystallinity of the WS_2 is not very high as evidenced by the lack of separation of peaks in the 30-45° range on the pattern. Decreased crystallinity is usually observed with very small or very thin WS_2 materials.[19] A peak at 25° (*) is visible which is due to excess tungstic acid (JCPDS -ICDD pattern no: 84-0886).[20] The Raman spectrum in Figure 3.3 (b) indicates two modes characteristic of 2H-WS_2. The 2LA (M) mode at 353 cm^{-1} and the $A_{1g}(\Gamma)$ mode at 418 cm^{-1}. From various studies, it has been shown that the frequencies of these modes, especially $A_{1g}(\Gamma)$, are affected by the number of layers in the material as discussed in the literature review. The $A_{1g}(\Gamma)$ mode is located at 418 cm^{-1} which indicates two layers of WS_2.[21,22] The intensity ratio (I_{2LA}/I_{A1g}) between the 2LA and $A_{1g}(\Gamma)$ mode is 1.4, which is also indicative of a double layer of WS_2.[21]

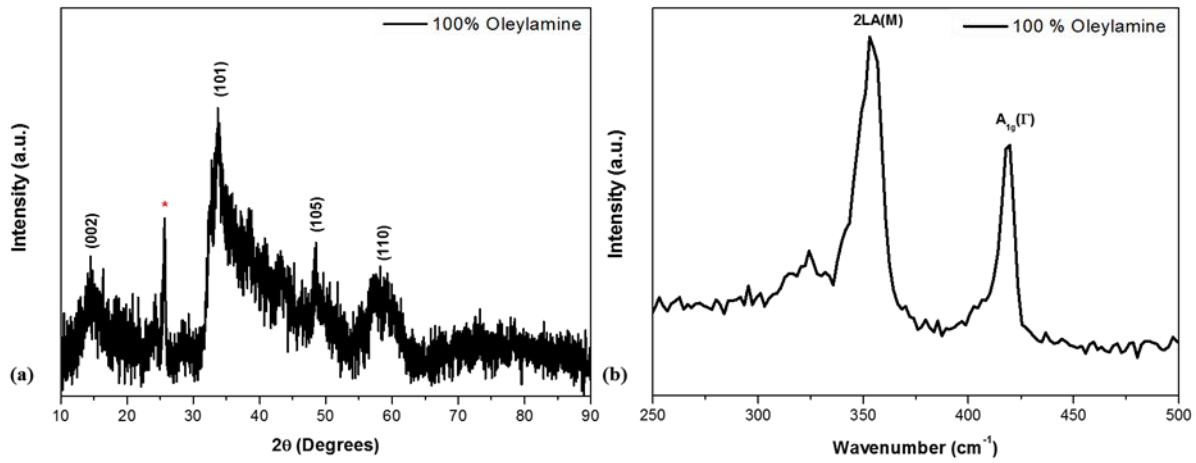


Figure 3.3: (a) PXRD pattern and (b) Raman spectrum of WS_2 synthesized with only oleylamine as a capping agent.

Transmission and scanning electron microscopy (TEM and SEM) have been used to visualize the structures and morphologies of the WS_2 particles formed. The TEM micrograph in Figure 3.4 (a) shows the flower-like WS_2 that was produced. The 'petals' of these flowers do not appear to be connected at a central core growing outwards. Instead, they appear to be assembled randomly. The TEM image also shows that the compactness of the flowers is different. Some flowers show more compact petals (green circle) while others look more like crumpled/folded sheets (red circle). The more compact flowers could possibly be formed by the continuous folding over of the sheets into a flower-like morphology. From the SEM micrograph in Figure 3.4 (b) the petals appear to be made up of assemblies of sheets that have their edges exposed. Perhaps the small sheets are made of a bilayer WS_2 that aggregate to form the flower-like morphology. This morphology could possibly lead to a very high surface area which would be beneficial in catalytic applications.

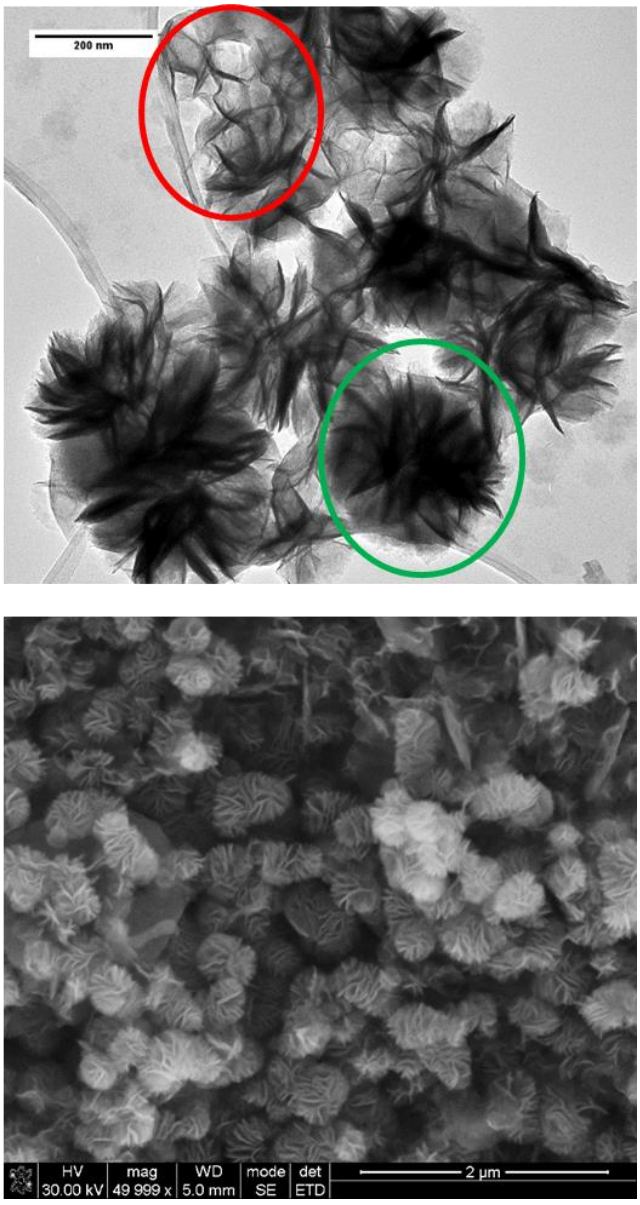


Figure 3.4: (a) TEM and (b) SEM micrographs of flower-like WS_2 synthesized with only oleylamine as a capping agent.

Proton NMR spectroscopy was used to identify the ligands bound to the surface of the nanoparticles. When the capping agents are bound to the surface of the nanoparticles, line broadening and signal shifts occur on the ^{1}H-NMR spectra.[23] Figure 3.5 shows the ^{1}H-NMR spectra of pure oleylamine and the OLA capped WS_2 particles. The double bond proton resonance peaks situated at 5.34 ppm are shifted to 5.4 ppm on the OLA capped WS_2 nanoparticles as shown in Figure 3.5 (a). Another characteristic resonance peak belonging to the methylene protons adjacent to the amine group has a resonance peak at 2.67 ppm as shown in Figure 3.5 (b). This resonance peak is weakened and severely broadened so that it

appears to be absent. These results show the presence of oleylamine on the nanoparticle surface.

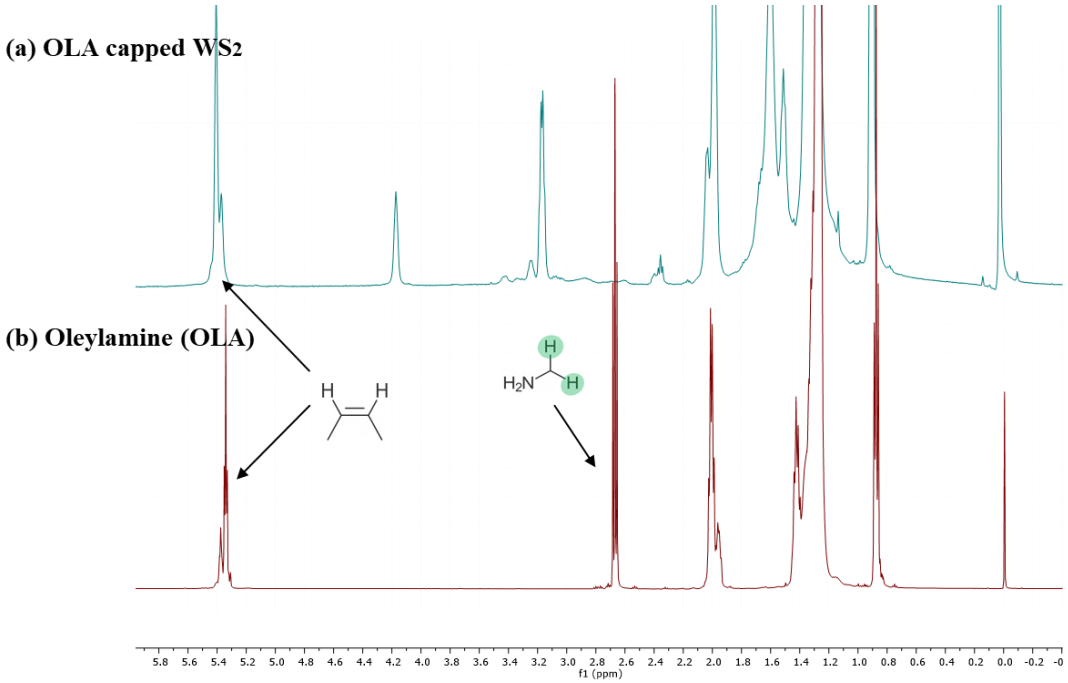


Figure 3.5: ^{1}H-NMR spectra of (a) WS_2 nanoparticles capped with oleylamine and (b) pure oleylamine.

UV-Vis spectroscopy is able to provide information on the optical and electronic properties of the WS_2 produced. The absorption spectrum in Figure 3.6 shows three weak absorption peaks attributed to the three distinct excitons associated with semiconducting 2H-WS_2. Exciton A and B, at 670 nm and 524 nm respectively, are a pair that appear due to interlayer coupling within WS_2.[24] Exciton A and B are direct transitions that occur between the split valence band and the conduction band at the K-point of the Brillouin zone.[24] Exciton C at 450 nm is a high energy exciton that is caused by optical transitions between densities of state in the valence and conduction band of WS_2.[25]

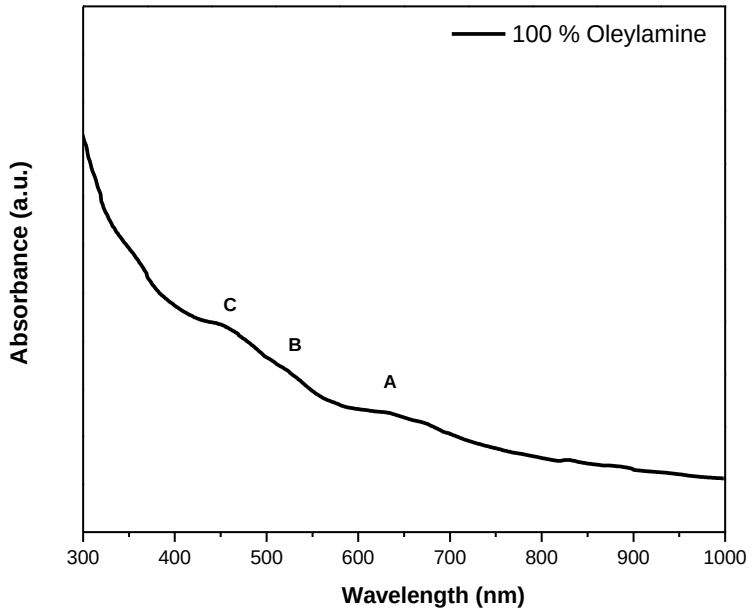


Figure 3.6: UV-Vis absorption spectrum of WS_2 synthesized with only oleylamine as a capping agent.

Oleylamine has been shown to preferentially passivate the edge sites of the sheets, because the edges of the sheets contain tungsten atoms that are not fully coordinated, hence causing them to have higher surface energy.[15,26,27] The formation of the nanosheet assemblies into flowers could be related to the reduction of the surface energy of the particles. Since oleylamine stabilizes the edges more strongly, they have lower surface energy and are exposed as shown on the SEM image (Figure 3.4 (b)). The basal plane may not have been stabilized as effectively, causing their surface energy to remain high. Therefore the nanosheets assemble to form a flower-like morphology to reduce the surface energy. The formation of only a bilayer of WS_2 may be due to the fact that excess oleylamine attaches weakly to the basal plane, preventing the growth of more than 2 layers of WS_2.

3.3.2 WS_2 nanostructures synthesized with ratios of 1-Octadecene (ODE)

The PXRD patterns in Figure 3.7 indicate that the crystal structure of the materials is that of 2H-WS_2 (PDF: 01-084-1398). As the ODE concentration increases from 25% to 75%, the (002) plane at 14° decreases and ultimately disappears at 75% ODE. The (002) plane represents the c-axis of the material. Where the (002) peak is diminished, it is indicative of a single layer of WS_2. The crystallinity is also decreased at the 75% concentration of ODE. This is evidenced by the very few, poorly defined peaks. For the lower concentrations of

ODE (25% and 50%), the (002) plane increases in intensity and broadens, which indicates the presence of a few layers of WS_2. These patterns also show the presence of WO_x impurities (*) which may have been caused by oxidation during synthesis at high temperatures. The increase in impurities as more ODE is used could be due to less reduction occurring as the concentration of oleylamine decreases significantly. This is supported by the EDS spectra in Figure 3.8 that show the presence of oxygen in addition to tungsten and sulfur.

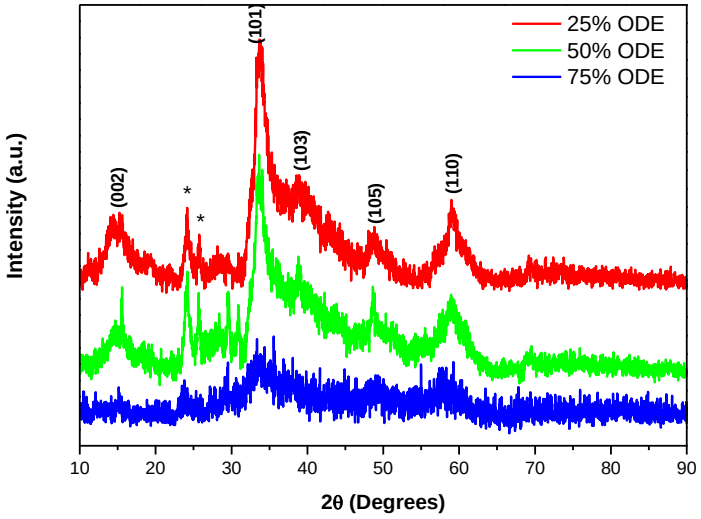


Figure 3.7: PXRD patterns of WS_2 synthesized with increasing concentrations of octadecene.

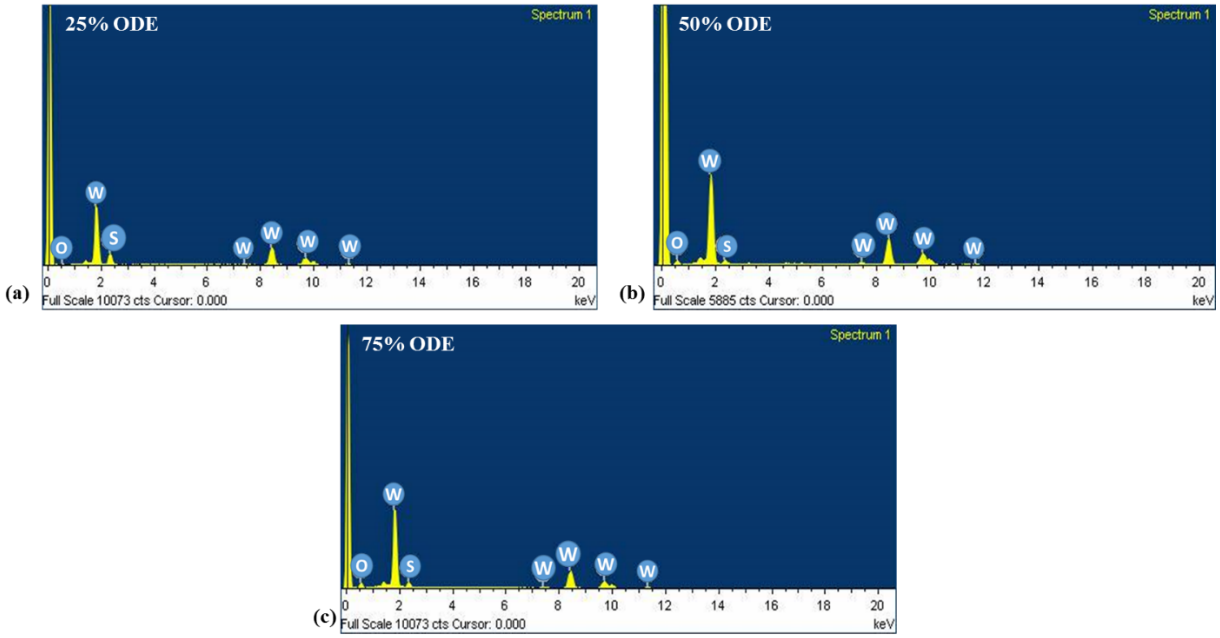


Figure 3.8: EDS spectra of WS_2 prepared with a (a) 25%, (b) 50% and (c) 75% concentration of octadecene.

Raman spectroscopy was used to probe the crystal structure. The $E^1_{2g}(\Gamma)$ and $A_{1g}(\Gamma)$ modes are depicted on the Raman spectra in Figure 3.9. On closer inspection, a shift to lower wavenumbers is observed for the $A_{1g}(\Gamma)$ mode as the concentration of ODE increases. At 25% and 50% ODE, the $A_{1g}(\Gamma)$ mode is at 419 cm^{-1} and decreases to 417 cm^{-1} at 75% ODE. As was previously stated, the $A_{1g}(\Gamma)$ mode frequency is highly dependent on the number of layers. It has been shown that when the $A_{1g}(\Gamma)$ mode is situated at 419 cm^{-1}, it is indicative of a four layer material. The frequency decreases to 417 cm^{-1} which is characteristic for a single layer of WS_2.[21,22] Therefore the increasing concentration of ODE affects the thickness of the material. The decreasing thickness is also supported by the diminishing (002) plane intensity on the PXRD pattern. The $E^1_{2g}(\Gamma)$ mode remains at a Raman shift of about 355 cm^{-1}.

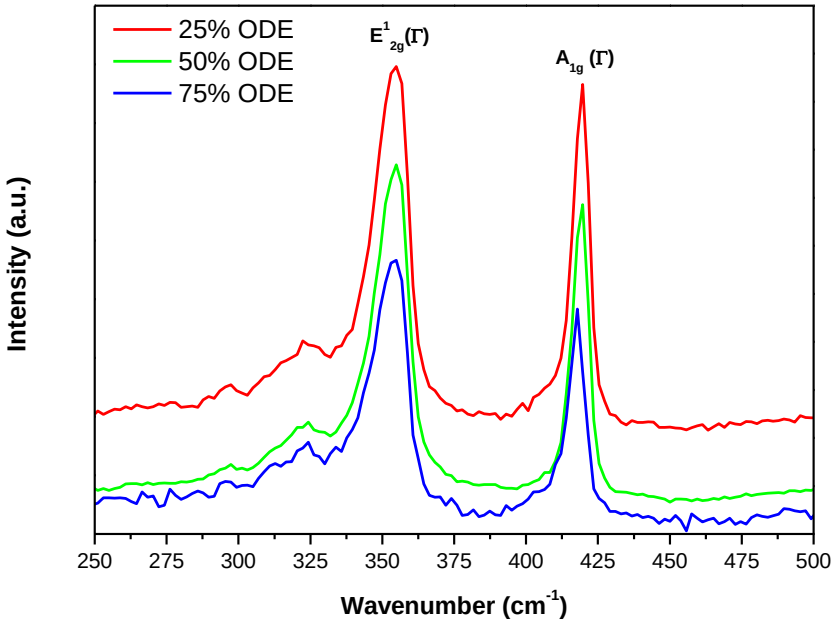


Figure 3.9: Raman spectra of WS_2 synthesized with different concentrations of octadecene as a co-capping agent.

The TEM micrographs in Figure 3.10 (a-f) shows the WS_2 obtained from the different ODE concentrations in order to observe the morphology produced. At a 25% ODE concentration (Figure 3.10 (a, b)), the WS_2 takes on a sheet-like morphology. The sheets appear to be crumpled or folded in places. This is understandable as flat two-dimensional nanosheets are more unstable and folding and crumpling is a mechanism to reduce the surface energy.[28] The crumpling of the sheets makes it appear as if the WS_2 has a flowerlike morphology as shown in Figure 3.10 (b). When a 50% concentration of ODE is used, the flowerlike morphology is more pronounced as shown in Figure 3.10 (c, d). Most of the flowers appear to be made up of

folding nanosheets that overlap onto each other. It is also evident that not all the WS_2 formed are in a flower-like morphology. Some exhibit the crumpled nanosheet morphology (Figure 3.10 (d)). An ODE concentration of 75% produces thin, crumpled WS_2 sheets that also have a flower-like morphology (Figure 3.10 (e)). The red oval in Figure 3.10 (f) shows a section where it appears that a few sheets have assembled or agglomerated at a point or sheets have folded over onto each other. The folding of the nanosheets here does not form very dense flowers compared to the 50% ODE concentration.

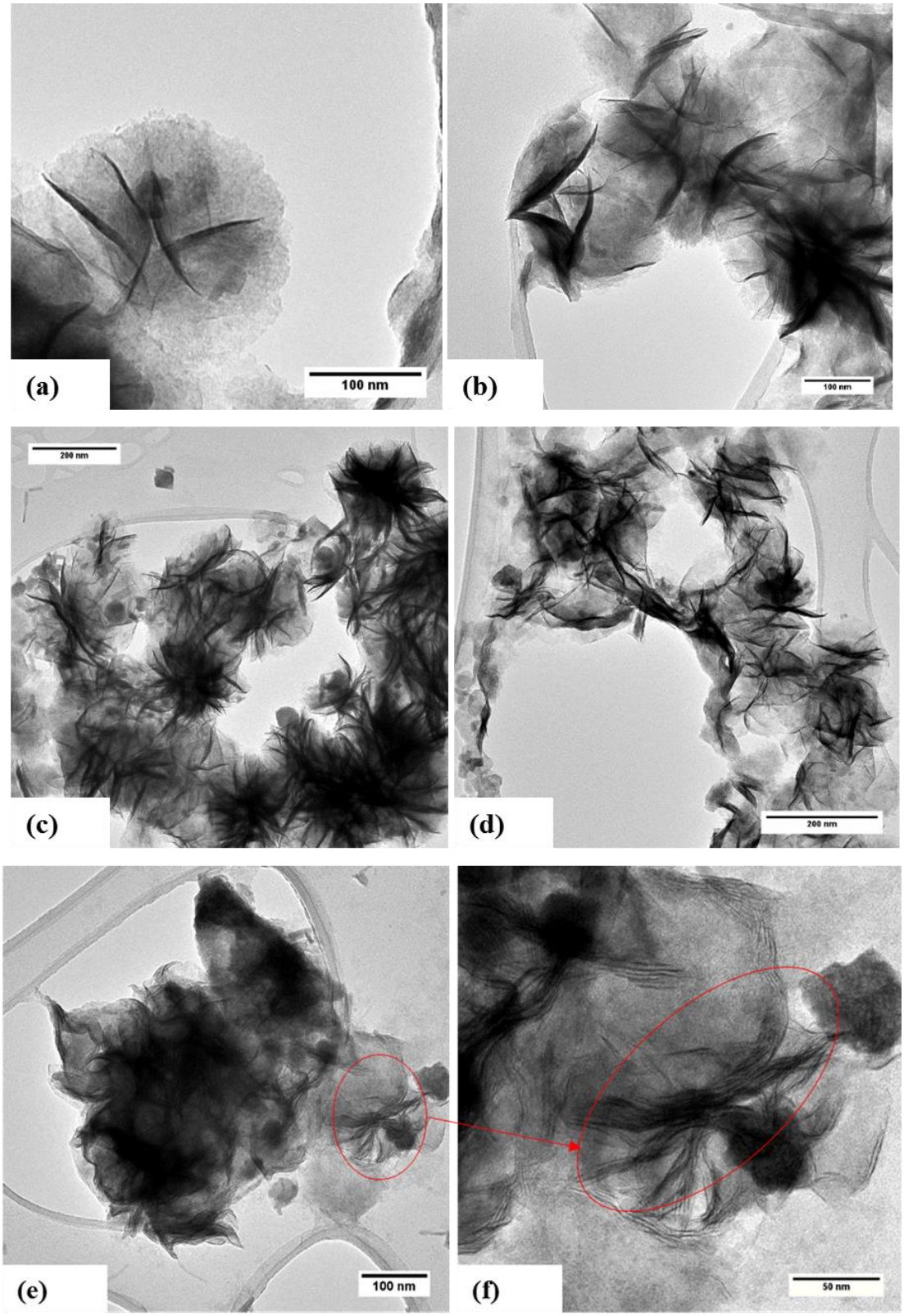


Figure 3.10: TEM micrographs of WS_2 obtained using (a, b) 25%, (c, d) 50% and (e, f) 75% concentration of octadecene.

FT-IR spectroscopy is able to give an indication of the capping of the ligands on the surface of the nanoparticles. The FT-IR spectra of pure 1-octadecene and oleylamine are depicted in Figure 3.11 (a). The purple labels correspond to bands exclusive to oleylamine, while the black labels correspond to bands exclusive to octadecene. The blue labels are the bands both capping agents have in common. In Figure 3.11 (b) and (c) are the WS_2 FT-IR spectra. The first observation is that the (-C-H) and (=C-H) stretches between 2750 cm^{-1} and 3000 cm^{-1} are present but weak. There also exists weak and broad peaks 1406 cm^{-1} and 940 cm^{-1} which correspond to the (CH_3) bending mode and the (C=C) bend from the amine capping agent respectively (Figure 3.11 (c)). These results suggest that oleylamine is present as a capping agent. The peaks corresponding to the amine head group have disappeared which suggests that chemisorption onto the WS_2 through the amine has taken place. The lack of any distinctive octadecene bands on the WS_2 materials makes it difficult suggests that there was no coordination of octadecene onto the particles. 1-octadecene is a non-coordinating solvent. It is, therefore, possible that octadecene did not coordinate to the WS_2, however, was inserted between the WS_2 layers. As was shown with the Raman spectra that the layers decreased when the octadecene concentration increased.

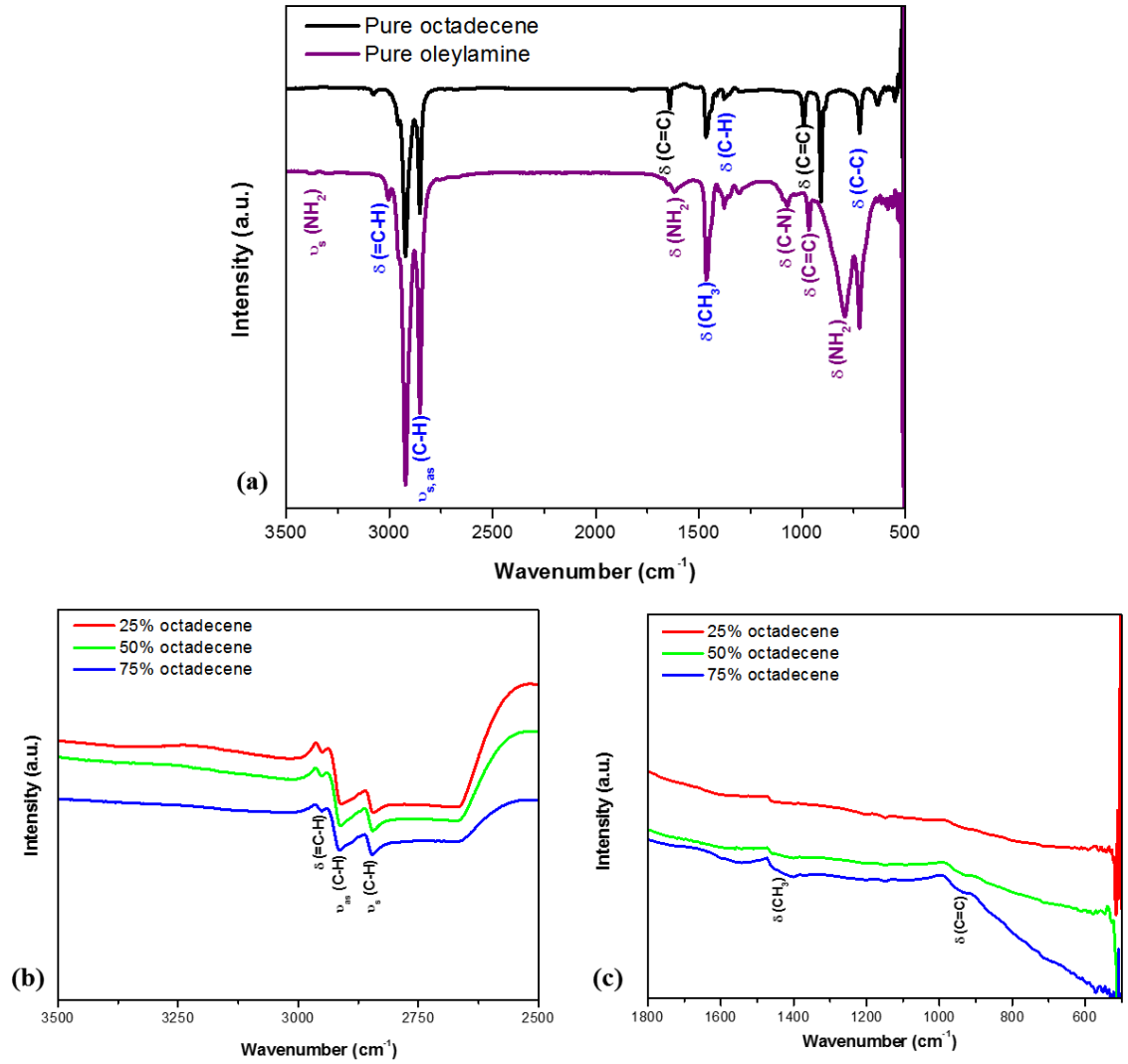


Figure 3.11: FT-IR spectra of (a) pure oleylamine and octadecene and (b, c) WS_2 synthesized with both capping agents.

Due to the limiting information that was obtained from FT-IR spectroscopy, ^{1}H-NMR was done on the 75% ODE concentration sample to determine the presence of octadecene on the surface of the WS_2. As was said earlier, ^{1}H-NMR is a useful tool used to identify the ligands that are capped onto the WS_2 nanoparticle surface. The WS_2 spectrum contains resonance peaks that belong to both oleylamine and octadecene. The resonance peaks of the oleylamine vinyl protons are situated between 5.33 and 5.39 ppm as shown in Figure 3.12 (a). These resonance peaks are shifted and slightly broadened on the WS_2 spectrum as shown in Figure 3.12 (b). A peak shift and broadening is also observed for the methylene protons adjacent to the amine group at 2.67 ppm. The shifts and broadening indicate that oleylamine is indeed capping the WS_2 nanoparticles.

In the case of octadecene, the double bond proton resonance peaks appear as a multiplet at 4.9-5 ppm as shown in Figure 3.12 (c). These resonance peaks are present on the WS_2 spectrum and have slightly shifted as well. The WS_2 spectrum also contains a weak resonance peak at 5.8 ppm that also comes from octadecene, suggesting that octadecene has also capped the WS_2 nanoparticles. Octadecene is not expected to cap the particles as it is a non-coordinating solvent, however, the double bond could be involved in a weak dative bond that results in the capping of the nanoparticles.

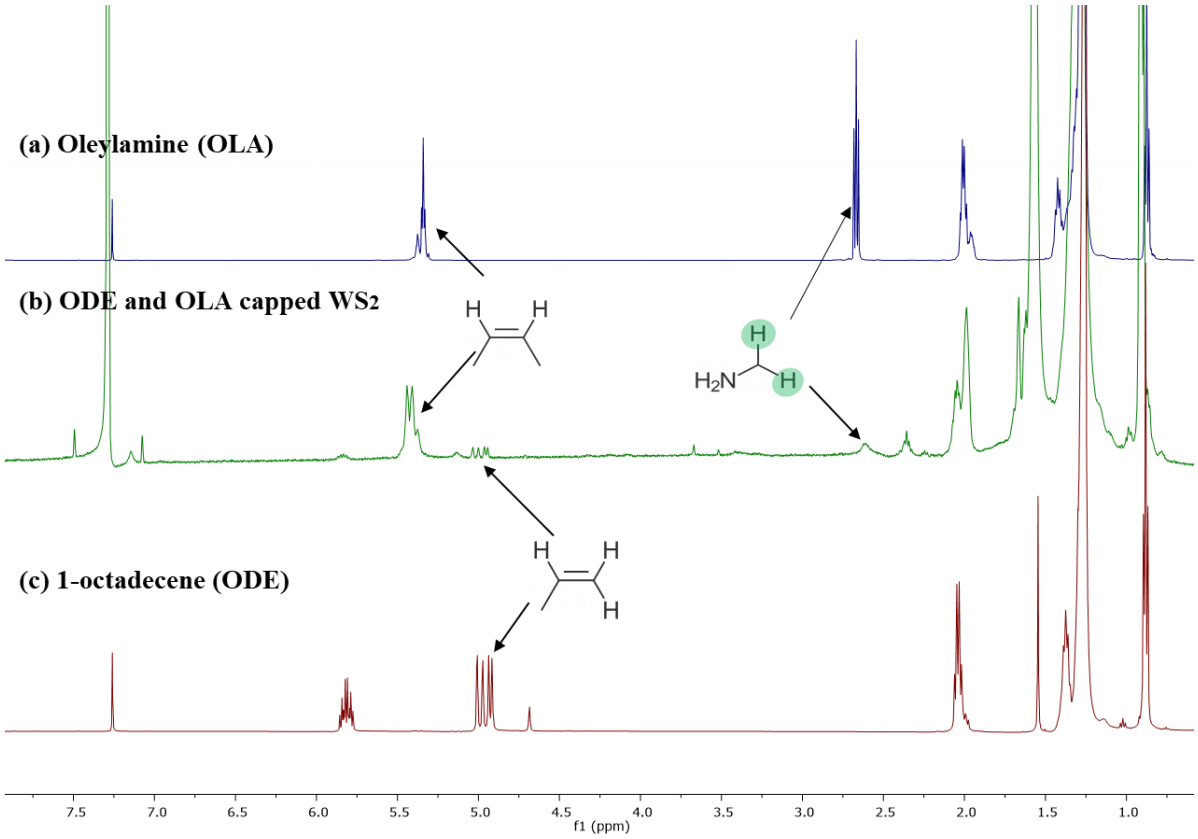


Figure 3.12: ^{1}H-NMR spectra of (a) pure oleylamine, (b) WS_2 and (c) pure octadecene.

UV-Vis absorption spectra shown in Figure 3.13 are able to reveal the semiconducting nature of the materials. The UV-Vis absorption spectrum for 25% ODE shows the three characteristic absorption peaks of 2H-WS_2. The A and B excitonic pair that is caused by interlayer and spin-orbit coupling is present,[20] including exciton C which is caused by optical transitions between densities of state in the valence and conduction bands of WS_2.[25] As the ODE concentration increases, the absorption peaks weaken until they disappear at the 75% concentration of ODE. With 50% ODE, the B-exciton decreases. The presence of both A and B excitons is only seen in few layered WS_2,[20] so the weakening of the B-exciton could be due

to the decreasing of the number of layers, which is suggested also by the Raman spectra. Table 3.2 shows the positions of the absorption peaks. An absorption spectrum that is void of the three characteristic WS_2 excitons as shown for the 75% ODE spectrum is usually seen with WS_2 quantum dots.[29] This kind of absorption indicates a significant widening of the band gap, due to quantum confinement.[19] In this case, the WS_2 formed are not quantum dots, but single layer WS_2. Bulk WS_2 exhibits absorption of light starting at 920 nm,[30], therefore, the WS_2, in this case, shows a significant blue shift which is caused by quantum confinement.

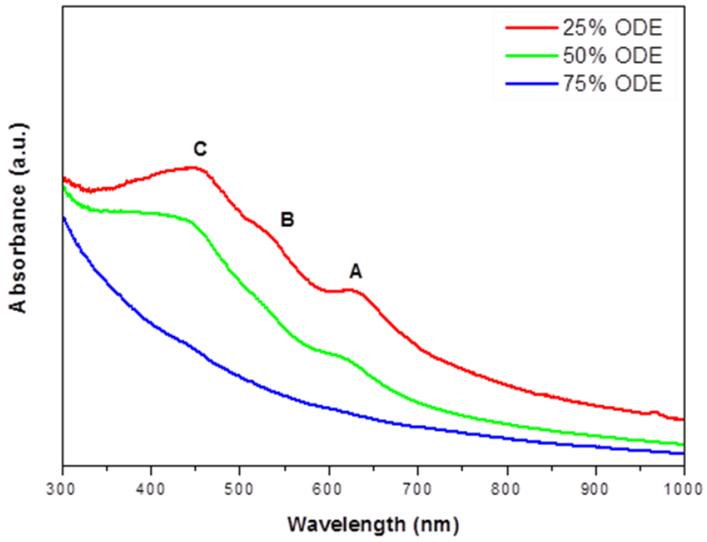


Figure 3.13: UV-Vis absorption spectra of WS_2 prepared using various concentrations of octadecene.

Table 3.2: The wavelengths at which the absorption peaks of WS_2 peaks appear

	A (nm)	B (nm)	C (nm)
25% ODE	628	536	451
50% ODE	620	-	445
75% ODE	-	-	-

3.3.3 WS_2 nanostructures synthesized with ratios of oleic acid (OAc)

The PXRD patterns of the WS_2 synthesized with oleic acid are depicted in Figure 3.14. Using a 25% oleic acid concentration produces very crystalline 2H-WS_2 (PDF: 01-084-1398). The high intensity (002) plane indicates the well-stacked structure. With the addition of more oleic acid to the reaction mixture (Figure 3.14 (b)), two different materials are formed. 2H-WS_2 as shown by the indexed planes and a highly crystalline ammonium tungsten oxide $(NH_4)_{0.5}(WO_3)$* matching to PDF: 01-073-9917. The intensities of the WS_2 (002) plane are

decreased, indicating the formation of fewer layers compared to the 25% oleic acid concentration. There also exists a (100) plane that belongs to WO_3 (PDF: 00-041-0905). When the oleic acid concentrations are increased, there might be a decreased reduction of the H_2WO_4 precursor, leading to the formation of WO_3 within the flask. The ammonium ion (NH_4^+) could possibly come from the NH_3 gases that are produced from the thiourea precursor or from the $RCOO^-$:RNH_4^+ acid-base complex that forms between the two capping agents.[4] From the patterns in Figure 3.14 (b), it appears that the WS_2 peaks are broadening, with some peaks disappearing, indicating the decrease in crystallinity of WS_2 as well as a decrease in the thickness of the material.

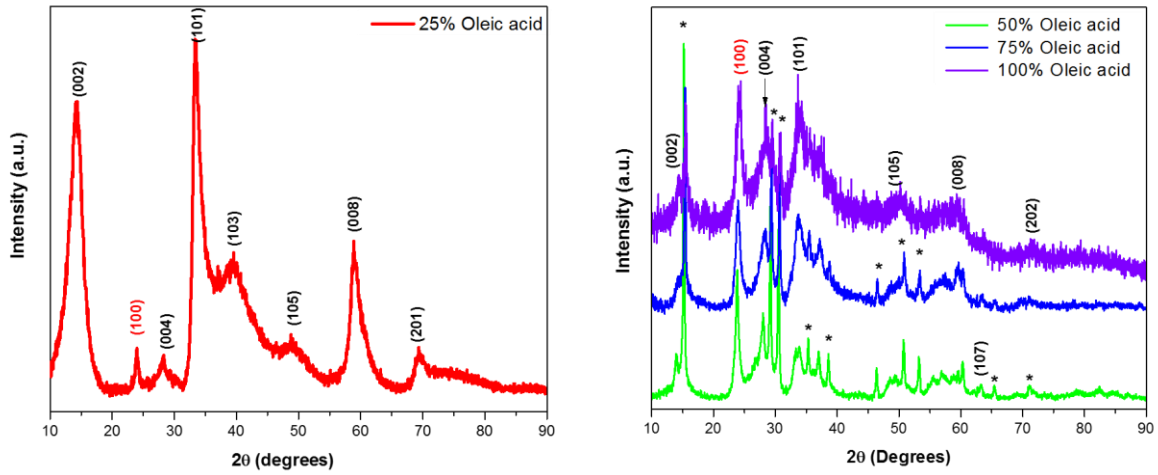


Figure 3.14: PXRD patterns of WS_2 synthesized using various concentrations of oleic acid.

The Raman spectra depicted in Figure 3.15 shows two modes of 2H-WS_2: $E^1_{2g}(\Gamma)$ and $A_{1g}(\Gamma)$. Close inspection of the spectra shows that the frequency of the $A_{1g}(\Gamma)$ mode decreases from 418 cm^{-1} to 417 cm^{-1} as the oleic acid concentration increases from 25% to 100%. The decrease of the $A_{1g}(\Gamma)$ mode frequency indicates the decreasing of the number of layers of WS_2. This is also observed on the PXRD patterns. The $E^1_{2g}(\Gamma)$ mode shows no appreciable shifts as the oleic acid concentration increases. The frequency of the $A_{1g}(\Gamma)$ mode for the 25% oleic acid concentration suggests two layers of WS_2. The $A_{1g}(\Gamma)$ mode for the higher oleic acid concentrations is situated at 417 cm^{-1} suggesting a single layer of WS_2. The presence of the (002) plane in the PXRD patterns, however, shows that WS_2 contains more one layer.

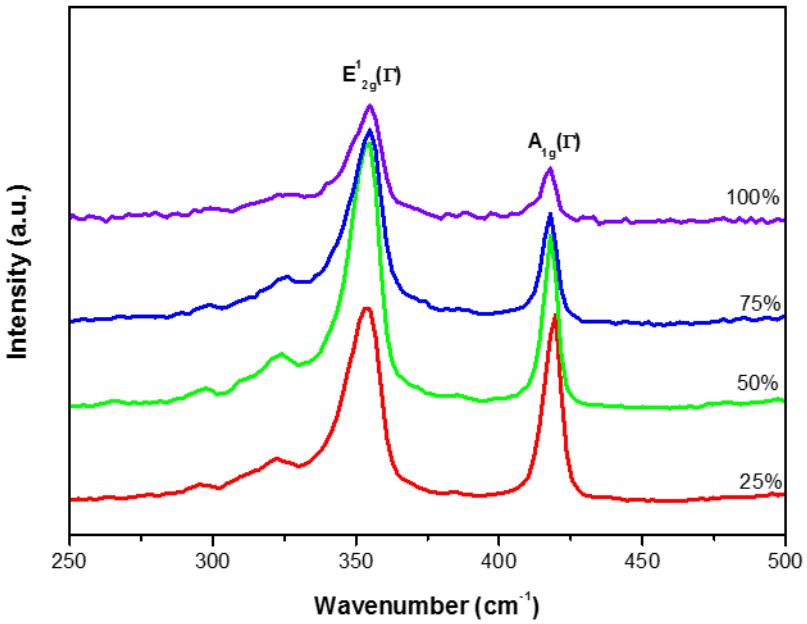


Figure 3.15: Raman spectra of WS_2 from various concentrations of oleic acid.

TEM and SEM images in Figure 3.16 show the morphology and the evolution of the morphology of the WS_2 produced as the oleic acid concentration increases. The particles synthesized with a 25% concentration of oleic acid (Figure 3.16 (a and b)) have a stacked, petal-like morphology that is between 110 nm and 160 nm wide as shown in the TEM and SEM images. There also exists some slightly crumpled sheets in the midst of these stacked petals. With more oleic acid in the reaction flask (50%), the stacked petal-like morphology changes into flatter sheets with curled up edges (Figure 3.16 (c)). The SEM image (Figure 3.16 (d)) shows a collection of nanosheets with their edges exposed. A 75% oleic acid concentration produces nanosheets that are flat in some areas and in other areas they are oriented sideways (Figure 3.16 (e)). The side-oriented sheets appear to be slightly wrinkled. The SEM image (Figure 3.16 (f)) shows agglomerations of edge-oriented sheets. Where only oleic acid is used as a capping agent, the WS_2 materials are agglomerated as shown by the TEM and SEM images (Figure 3.16 (g, h)).

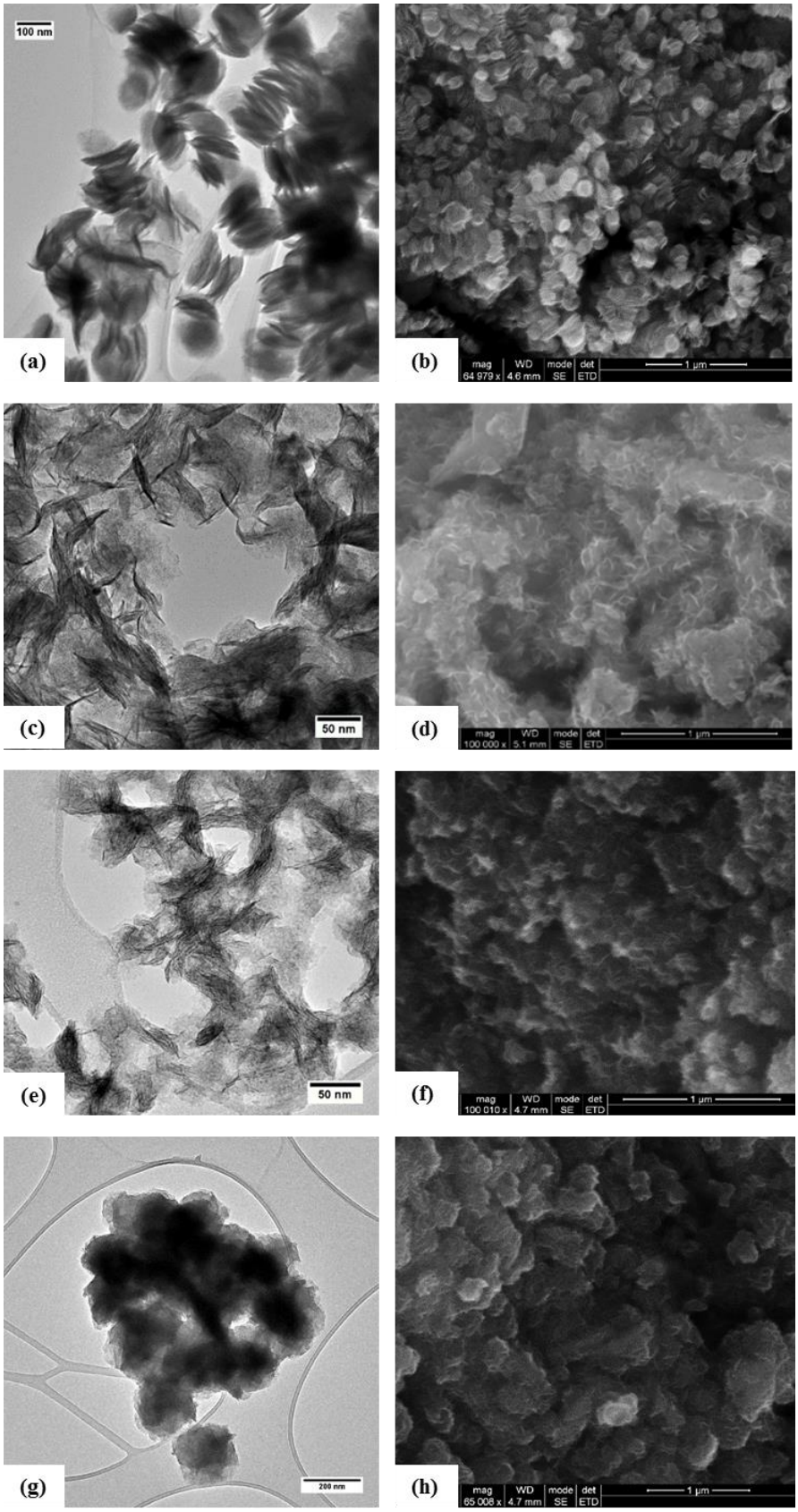


Figure 3.16: TEM and SEM images of WS_2 synthesized with (a, b) 25%, (c, d) 50%, (e, f) 75% and (g, h) 100% concentration of oleic acid.

From a study done on WSe_2 nanosheets, it was reported that amines have the greatest affinity for the edge sites than carboxylic acids.[15] The stacking of the "petals" is a way of minimizing the surface energy of any freestanding petals.[28] When the concentration of oleic acid is increased, the morphology of the WS_2 changes from stacked petals to flatter nanosheets. The flattening of the nanosheets can be due to more effective passivation of the basal plane of the WS_2 by the higher concentration of oleic acid. However, when only oleic acid is used, agglomeration occurs which indicates that oleic acid on its own is not an effective capping agent in this synthesis. It was reported in the colloidal synthesis of quantum dots, that a high concentration of oleic acid, causes delayed nucleation and ultimately results in larger quantum dots.[31] The agglomeration observed when a 100% oleic acid is used could be due to the delayed nucleation.

The FT-IR spectra of pure oleylamine and oleic acid are depicted in Figure 3.17 (a). The relevant stretching and bending modes are labeled. The red labels correspond to the bands that the two capping agents have in common. In Figure 3.17 (b), the spectra of WS_2 synthesized with different concentrations of oleic acid are shown. Between 2800 cm^{-1} and 2900 cm^{-1} the asymmetric and symmetric CH_2 stretches are visible. Figure 3.17 (c) shows a close-up of the region between 800 cm^{-1} and 1600 cm^{-1}. At 1460 cm^{-1} there exists a weak peak (*) that has been assigned to a metal carboxylate band.[32] This band indicates that oleic acid is coordinated to the metal ion via the COO^- head group. At 1403 cm^{-1}, the symmetric stretch of the carboxylate group of oleic acid is visible, although weak for some of the samples. The disappearance of the C=O band could indicate that oleic acid has bonded to the particles as a bidentate ligand.[33] The 25% and 50% oleic acid samples also contain a C-N band at 1145 cm^{-1}, indicating the presence of oleylamine. The band disappears when the oleic acid concentration increases to 75% and 100%. This result suggests that the higher concentration of oleic acid causes it to dominate as the capping agent for the materials.

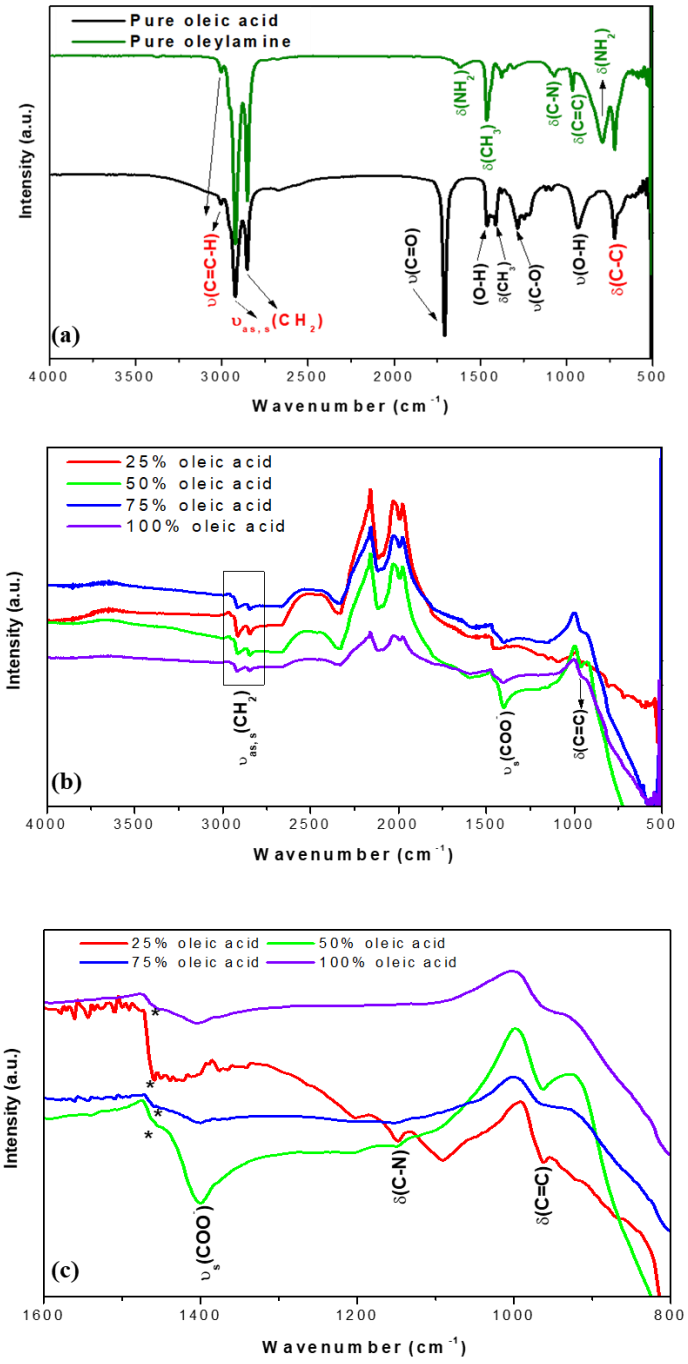


Figure 3.17: FT-IR spectra of (a) pure oleylamine and oleic acid as well as (b, c) WS_2 synthesized with different concentrations of oleic acid.

For further clarification of the binding of the capping agents, proton NMR was done on the WS_2 sample that was synthesized with a 50% concentration of oleic acid and oleylamine in order to determine whether both capping agents are indeed capping the particles or just one. Some of the characteristic resonance peaks from oleylamine and oleic acid are shown in Figure 3.18. The methylene protons adjacent to the carboxylic and amine groups are situated

at 2.34 ppm and 2.67 ppm respectively. The spectrum of the WS_2 particles contains these resonance peaks that are shifted and broadened. The same is observed for the alkene proton resonance peaks at 5.34 ppm that that shifted and broadened. This result shows that both oleylamine and oleic acid are capping the nanoparticles.

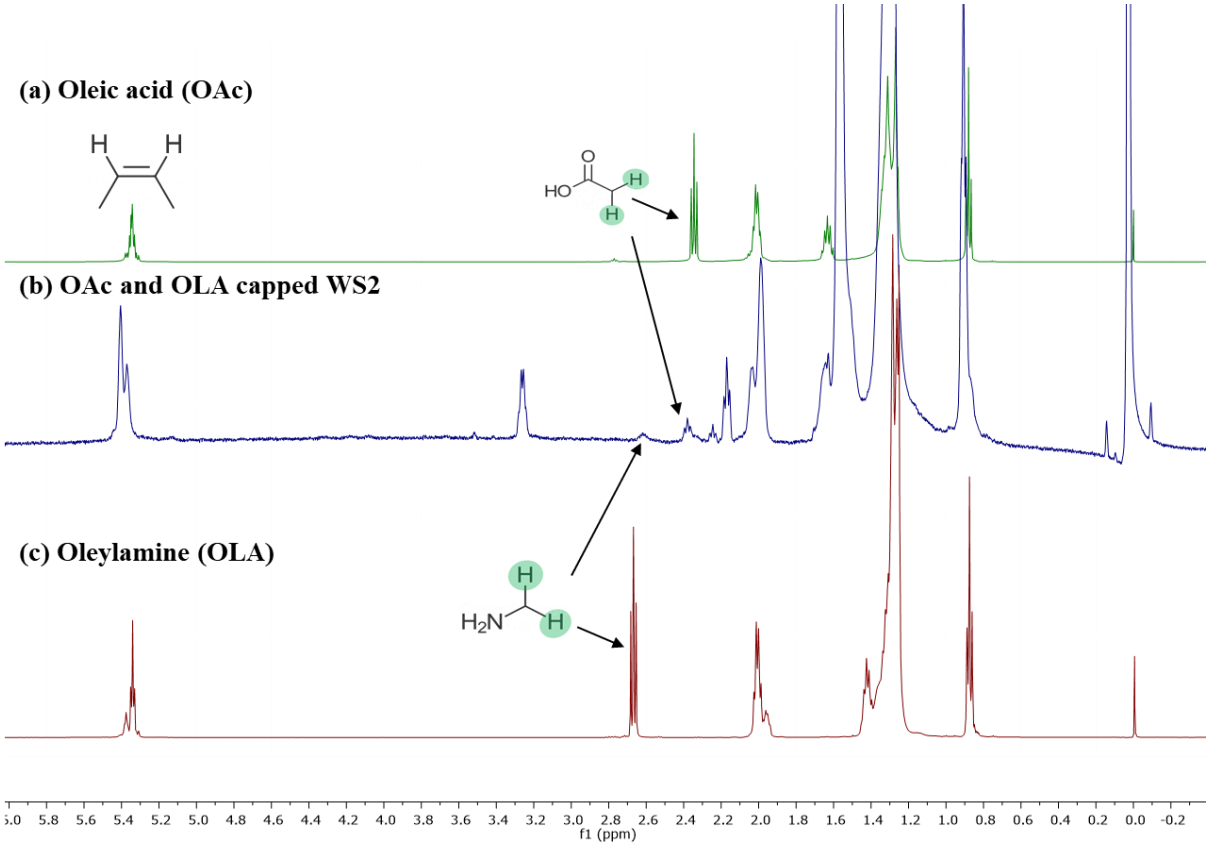


Figure 3.18: ^{1}H-NMR spectra of (a) pure oleic acid, (b) capped WS_2 and (c) pure oleylamine.

Three characteristic absorption peaks of 2H-WS_2 are depicted in the UV-Vis absorption spectra in Figure 3.19. The A-B direct excitonic pair as well as the C-exciton which corresponds to optical transitions between densities of state in the valence and conduction band. The A-exciton absorption occurs at 633 nm for the 25% oleic acid concentration. For the higher concentrations (50-75%), the A-exciton blue shifts to 618 nm, indicating that the WS_2 formed are smaller. The WS_2 obtained with a 100% oleic acid concentration shows red-shifting of the A-exciton. This is caused by the aggregation of the WS_2 as was shown in the TEM and SEM images in Figure 3.16.

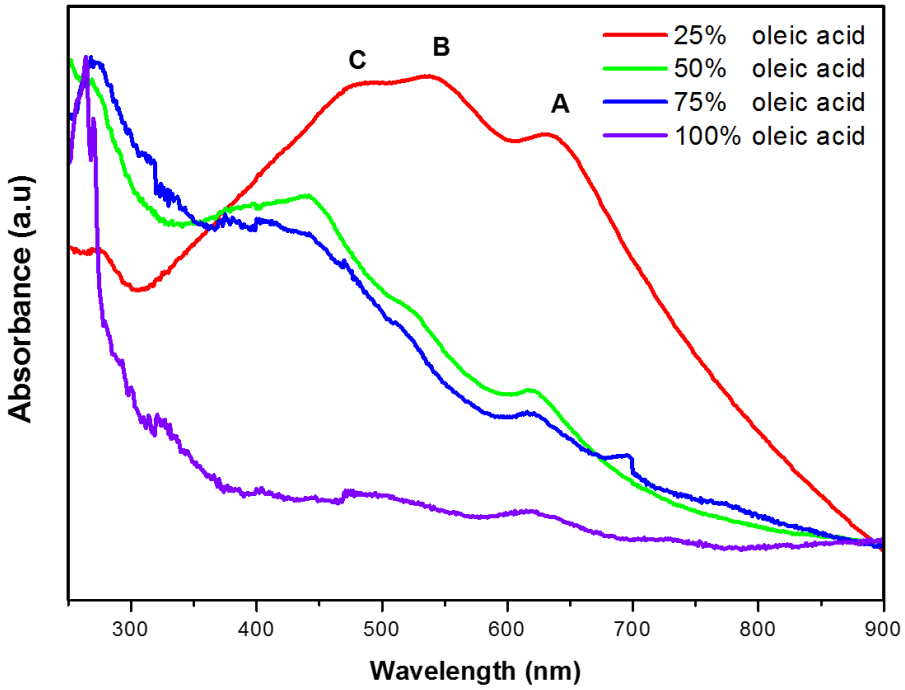


Figure 3.19: UV-Vis absorption spectra of WS_2 synthesized with various concentrations of oleic acid.

3.3.4 WS_2 nanostructures synthesized with ratios of oleyl alcohol

When oleyl alcohol was added as a co-capping agent to oleylamine, the crystal structure of the products matched that of 2H-WS_2 (PDF: 01-084-1398) as shown on the PXRD patterns in Figure 3.20. When only oleyl alcohol was used without any oleylamine, no reaction occurred. Instead, the reagents coagulated and stuck to the bottom of the reaction flask. The maximum concentration of oleyl alcohol used is therefore 75%. The presence of the (002) plane at 14° indicates that the WS_2 has a well-stacked, layered structure. The peaks marked with an asterisk are of the 3R-WS_2 polytype (PDF: 01-084-1399). The 3R- polytype occurs only with the 50% and 75% oleyl alcohol concentration. A WO_3 (100) plane appears at 25° (PDF 00-041-0905). WS_2 is prone to oxidation at high temperatures, especially when aliquots are extracted from the flask.

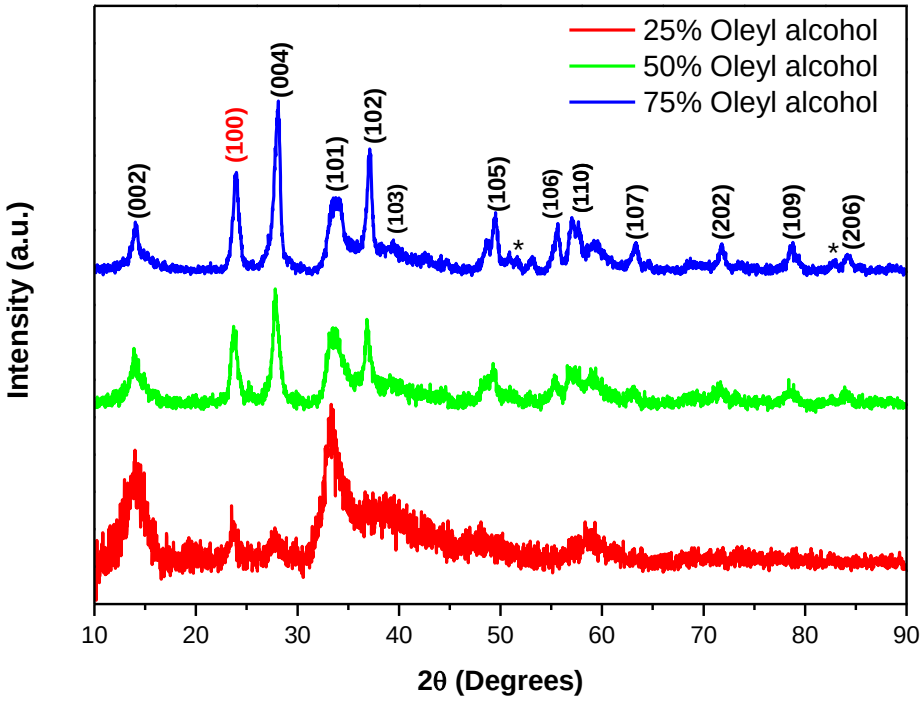


Figure 3.20: PXRD patterns of WS_2 synthesized with different concentrations of oleyl alcohol.

The Raman spectra in Figure 3.21 show the $E^1_{2g}(\Gamma)$ and $A_{1g}(\Gamma)$ modes characteristic of the 2H-WS_2 crystal structure. No significant shift of the $A_{1g}(\Gamma)$ mode, which remains at 418 cm^{-1} for all the oleyl alcohol concentrations occurs, as shown in Table 3.3. There is a slight shift of almost 1 cm^{-1} for the $E^1_{2g}(\Gamma)$ mode, from 354 cm^{-1} at the 25% and 50% concentration to 353 cm^{-1} for the 75% concentration. It has been shown that the frequency of the $E^1_{2g}(\Gamma)$ mode slightly decreases as the number of layers increase. From studies done on the number of layers, the frequencies of both modes have been assigned to WS_2 with two to three layers as shown in the table 3.3.[21,34] Hence, we can conclude that the WS_2 formed from using oleyl alcohol as the co-capping agent has between 2 and 3 layers.

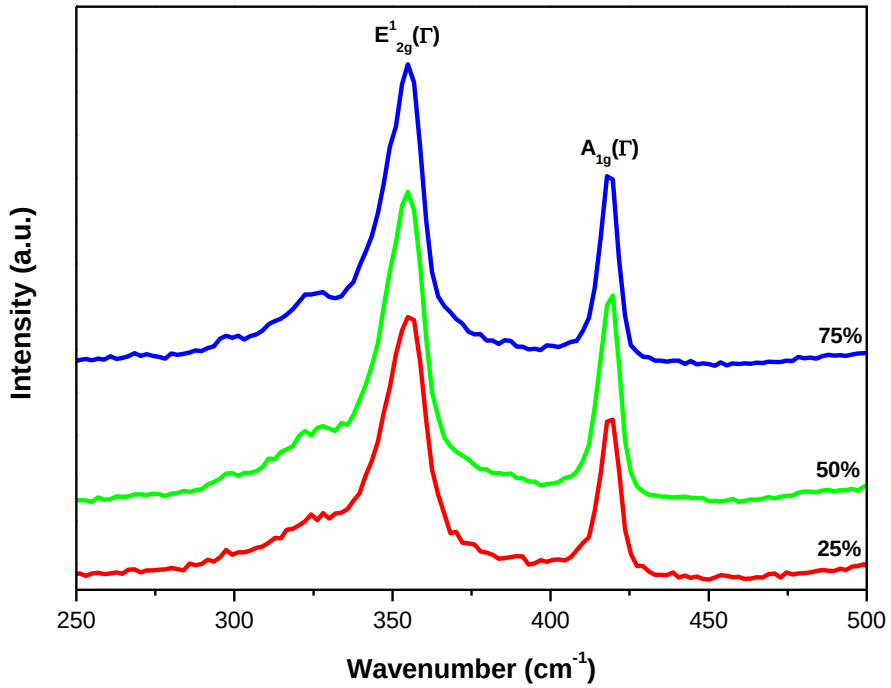


Figure 3.21: Raman spectra of WS_2 obtained from varying concentrations of oleyl alcohol.

Table 3.3: Raman shifts of the E^1_{2g} and $A_{1g}(\Gamma)$ modes of WS_2 synthesized with various concentrations of oleyl alcohol

	$E^1_{2g}(\Gamma)$	$A_{1g}(\Gamma)$	No. of layers
25%	354.5	418.7	2-3
50%	354.6	418.6	2-3
75%	353.9	418.5	2-3

The WS_2 produced from a 25% concentration of oleyl alcohol are thin sheets that are folded and crumpled into an almost flower-like morphology as shown in the TEM image in Figure 3.22 (a). The SEM image (Figure 3.22 (b)) shows edge-oriented sheets with some flowerlike structures. It appears that the flowerlike structures are formed from the folding and aggregation of these edge-oriented nanosheets.

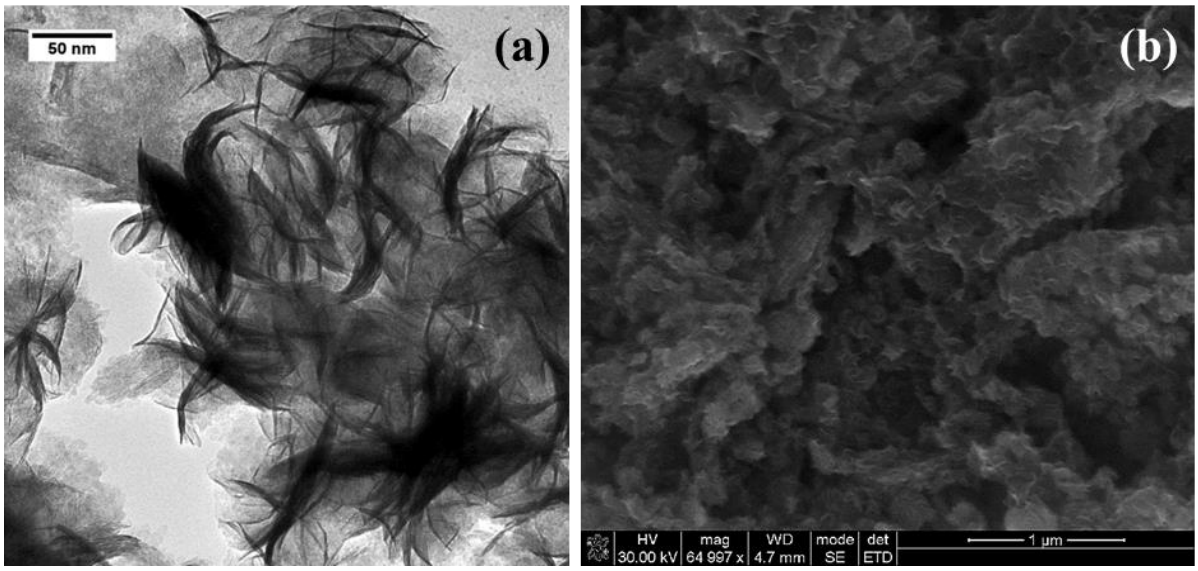


Figure 3.22: (a) TEM and (b) SEM micrographs of WS_2 synthesized with 25% oleyl alcohol.

The flower-like morphology is also formed with the 50% oleyl alcohol concentration as shown in the TEM image (Figure 3.23 (a)). These structures don't have a dense core that indicates growth from the centre. The structures appear more like assemblies of nanosheets in such a way that the edges are exposed. Figure 3.23 (b) is a SEM image that also shows the exposed edges of the nanostructures. The second SEM micrograph (Figure 3.23 (c)) shows the exposed edges also, however in this image the nanostructures seem to have fused together to form a continuous hierarchical structure.

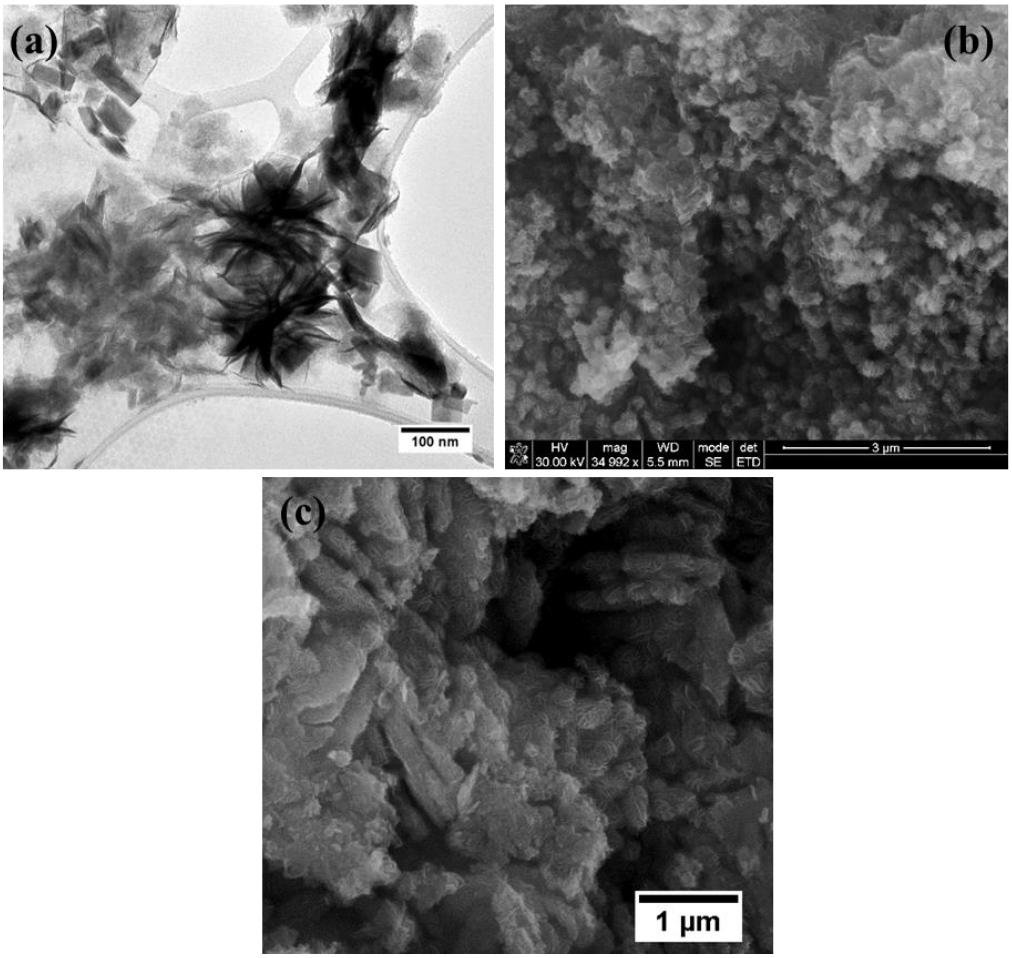


Figure 3.23: (a) TEM and (b, c) SEM micrographs of WS_2 nanoflowers synthesized with 50% concentration of oleyl alcohol.

A 75% oleyl alcohol concentration produces sheet-like WS_2 that are crumpled and folded over at the edges as shown in Figure 3.24 (a, b). The sheets appear to be very thin. The folding over is probably due to their instability and needing to reduce their surface energy.[28] From the SEM image (Figure 3.24 (c)), the sheets are visible with their edges exposed.

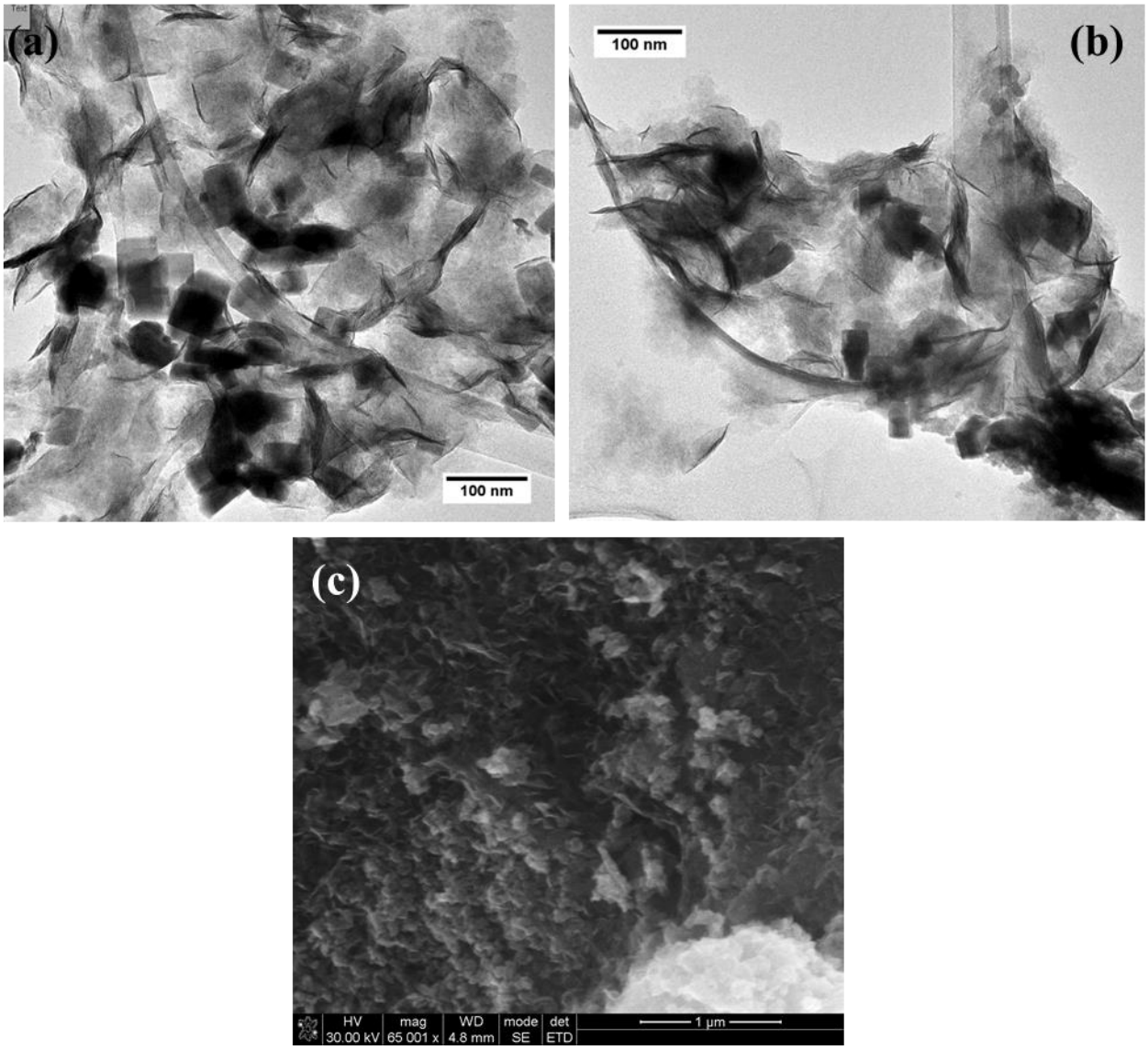


Figure 3.24: (a, b) TEM and (c) SEM micrographs of WS_2 synthesized with 75% oleyl alcohol.

The FT-IR spectra of pure oleylamine and oleyl alcohol are shown in Figure 3.25 (a). The blue labels show the bands that both capping agents have in common. Figure 3.25 (b, c) show the spectra of the WS_2 particles. It is evident from Figure b that the (=C-H) and (-C-H) stretches that come from both capping agents is present. Between 3300 cm^{-1} and 3400 $cm^{-1,}$ there exists a broadened peak that corresponds to the (O-H) stretch of oleyl alcohol. It is possible that oleyl alcohol binds to the particles with the lone pairs on the oxygen atom, leaving the O-H intact. It is evident that this peak is more prominent for the 50% and 75% oleyl alcohol concentrations. This indicates that for these particles, there is more oleyl alcohol capping the particles than oleylamine. Figure 3.25 (c) shows a broadened peak that is assigned to the (C-OH) stretch of oleyl alcohol. Again it is evident that this peak is more

prominent for the 50% and 75% oleyl alcohol concentrations. The absence of any nitrogen-containing modes makes it difficult to elucidate the adsorption of oleylamine on the nanoparticles.

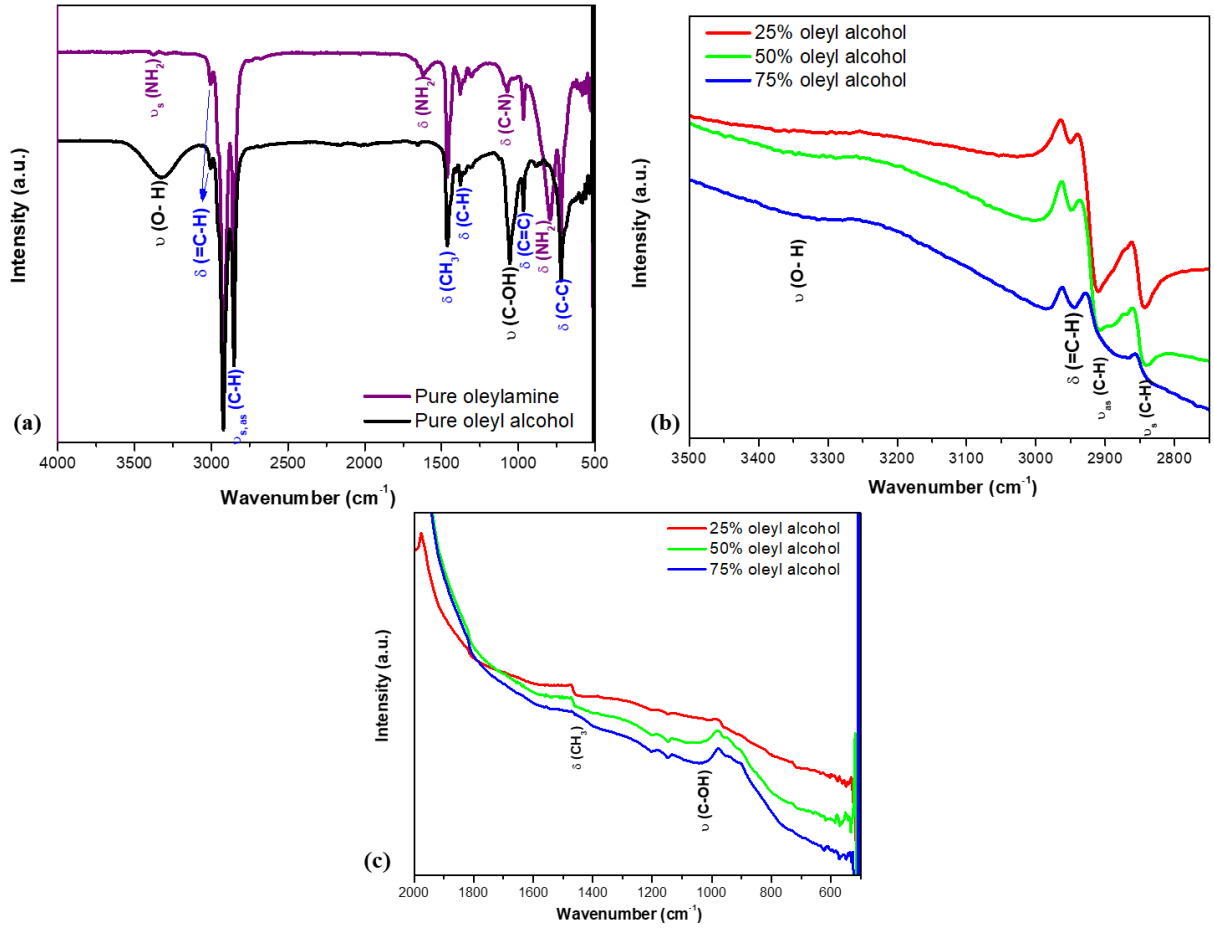


Figure 3.25: FT-IR spectra of (a) pure oleylamine and oleyl alcohol as well as (b, c) WS_2 synthesized with both these capping agents.

Proton NMR was also used on the 50% oleyl alcohol concentration WS_2 samples to elucidate the presence of both oleyl alcohol and oleylamine as capping agents for these samples.

Characteristic peaks belonging to both oleylamine and oleyl alcohol are depicted in the ^{1}H-NMR spectra in Figure 3.26. The methylene protons adjacent to the alcohol and amine moiety are situated at 3.67 ppm and 2.67 ppm respectively as shown in Figure 3.26 (a) and (c). The methylene protons that are one carbon away from the alcohol groups is shown at 1.57 ppm in Figure (a). The spectrum of the WS_2 particles has the vinyl proton resonance peaks at 5.4 ppm. It also contains the peaks for the methylene protons directly adjacent to the alcohol group at 3.67 ppm (shown as inset with black border). The methylene protons

adjacent to the amine group appear to be shifted and broadened (red inset spectra), indicating the capping of oleylamine as well. From these results, it can be concluded that both oleylamine and oleyl alcohol passivate the nanoparticles.

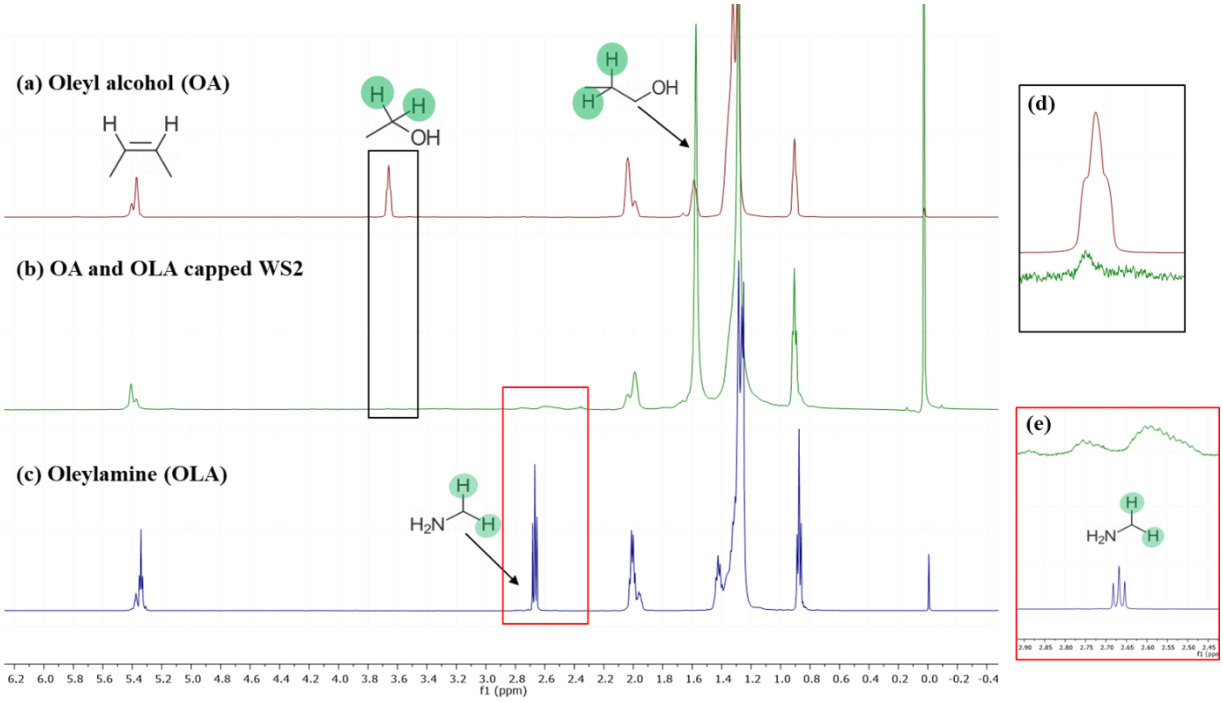


Figure 3.26: ^{1}H-NMR spectra of (a) pure oleyl alcohol, (b) capped WS_2 and (c) pure oleylamine. The insets (d, e) are a magnification of the areas on the spectra indicated by the rectangles.

The absorption spectra in Figure 3.27 shows the characteristic excitons associated with 2H-WS_2. The direct A-B exciton pair that appears with few layered WS_2 and the C- exciton peak that is due to optical transitions between densities of state in the valence and conduction bands. From the spectra, it is evident that the B peak is not very pronounced, probably due to the formation of bilayer WS_2. The interlayer coupling may be weak due to the presence of only two layers in each sheet. It is also evident that the 75% oleyl alcohol spectrum is slightly blue shifted to 615 nm compared to the other two spectra (both at 618 nm). The blue shift can be attributed to a slight decrease in the size of the nanosheets obtained. From the table it is shown that the A exciton peaks are at wavelengths that are significantly shorter than those on bulk WS_2 (920 nm), indicating the quantum confinement effect that has occurred within these nanocrystals.[11]

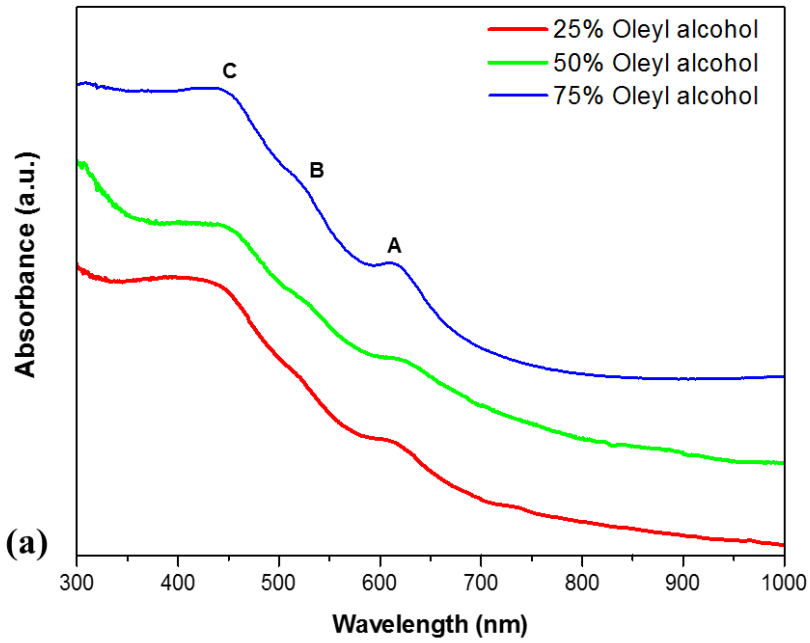


Figure 3.27: UV-Vis absorption of WS_2 using various concentrations of oleyl alcohol.

From the above data, it is evident that the oleyl alcohol concentration affects the morphology and the optical properties of the material. Firstly, it was shown that as the oleyl alcohol concentration increased, the morphology evolved from flower-like nanostructures to nanosheets. It has been suggested that the formation of flowerlike morphology in 2D layered materials is a way for the particles minimize their surface energy.[28] Capping agents such as oleylamine and oleyl alcohol also play the role of stabilizing the particles. As was mentioned in the section (3.1), capping agents can selectively cap certain facets of a particle more than others. From a study done on WSe_2, it was found that oleylamine has a higher affinity for the edge sites of WSe_2 than oleyl alcohol. This meant that the when more oleylamine is present in the vessel, lateral growth of sheets is hindered while horizontal growth is promoted.[15] This means that the basal plane surface energy remains high and the formation of flowers occurs to minimize that surface energy. This can be seen also in the WS_2 where only oleylamine is used as a capping agent in Figure 3.4. We know that free-standing 2D nanosheets are unstable and hence begin to fold in order to stabilize themselves. Free-standing nanosheets are observed when 75% oleyl alcohol concentration is used. This could mean that the oleyl alcohol passivates the free standing nanosheets better than oleylamine. This could mean that oleyl alcohol passivates the basal plane (002) better, hence the formation of thin nanosheets.
Secondly, the increase in the concentration of oleyl alcohol impacted the optical band gap of the material. The improved band gap could be caused by thin free-standing nanosheets. It has

been shown in literature that thin WS_2 have a larger optical band gap than thicker sheets. This is because of the band structure transitions from an indirect to a larger direct band gap.[35] This is shown by the slight blue shift of the A-exciton on the absorption spectra (Figure 3.27).

3.4 Conclusion

From the studies, one of the main observations was that when the concentration of oleylamine is high in the vessel, WS_2 tends to form a flower-like morphology. As the oleylamine concentration decreases, the flower-like morphology evolves into flat and almost free-standing sheets. It has been established that the edge sites of WS_2 are most unstable and in the flowerlike morphology, the edge sites are most exposed, indicating that oleylamine efficiently stabilizes them. In order to achieve WS_2 nanostructures that have more exposed edge sites or a dominating edge orientation, oleylamine is the best capping agent for that purpose as it has produced flowerlike WS_2 where it is in high concentrations.

1-Octadecene

It was shown through Raman and PXRD that increasing the octadecene ratio affects the thickness of the WS_2 produced. The morphology that was produced consists of folded sheet-like morphology to a flower-like morphology. The WS_2 produced with octadecene as a co-capping agent shows good visible light absorption.

Oleic acid

Using a concentration of oleic acid higher than 25% produces a mixture of products (WS_2 and $(NH_4)_{0.5}(WO_3)$. This makes the use of high concentrations of oleic acid undesirable. Oleic acid needs a co-surfactant to prevent the agglomeration of the WS_2 sheets. Although the high concentration of oleic acid causes the formation of mixtures, it is able to control the thickness of the WS_2 to a certain extent. A 25% oleic acid concentration produces WS_2 with many layers. High concentrations of oleic acid also decrease the crystallinity of the WS_2 produced. It appears that oleic acid binds to the WS_2 in a bidentate manner. Oleic acid dominates the capping of the nanoparticles as its concentration increases.

Oleyl alcohol

Oleyl alcohol cannot be used as a capping agent in this synthesis without an additional reducing agent. The concentration of oleyl alcohol can be tuned in order to tune the morphology of the WS_2 obtained. A high concentration of oleyl alcohol should be used if flat

WS_2 sheets are the desired morphology. The WS_2 formed with oleylamine and oleyl alcohol as co-surfactant is a good semiconductor with appreciable optical absorption in the visible range. Oleyl alcohol's weakened affinity for the edge sites of WS_2 makes it possible to determine the morphology of the material. A higher concentration of oleyl alcohol also increases the crystallinity of the WS_2 produced. There does not appear to be any real thickness control as the data suggests that all the WS_2 produced contains approximately two to three layers.

Overall, the study also suggests that in order to obtain WS_2 with appreciable crystallinity, oleylamine has to be used with a co-surfactant.

3.5 References

1. B. Ajitha, Y. A. K. Reddy, P. S. Reddy, H. Jeon, and C. W. Ahn, *RSC Adv.*, 2016, **6**, 36171–36179.
2. G. Murugadoss and V. Ramasamy, *Luminescence*, 2013, **28**, 69–75.
3. Z. Niu and Y. Li, *Chem. Mater*., 2014, **26**, 72-83.
4. R. A. Harris, P. M. Shumbula and V. Der Walt, *Langmuir*, 2015, **31**, 3934-3943.
5. S. Patra and A. Samanta, *J. Phys. Chem. C*, 2014, **118**, 18187-18196.
6. K. Akhil, J. Jayakumar, G. Gayathri and S. S. Khan, *Journal of Photochemistry and Photobiology*, 2016, **160**, 32–42.
7. E. E. L. Tanner, K. Tschulik, R. Tahany, K. Jurkschat, C. Batchelor-mcauley, and R. G. Compton, *J. Phys. Chem. C*, 2015, **119**, 18808-18815..
8. D. Wang and Y. Li, *Inorg. Chem*., 2011, **50**, 5196–5202.
9. C. M. Phan and H. M. Nguyen, *J. Phys. Chem. A*, 2017, **121**, 3213-3219.
10. C. Chiu, Y. Li, L. Ruan, X. Ye, C. B. Murray, and Y. Huang, *Nat. Chem.*, 2011, **3**, 393–399.
11. M. Nasilowski, B. Mahler, E. Lhuillier, S. Ithurria and B. Dubertret, *Chem. Rev*., 2016, **116**, 10934-10982.
12. Z. Niu, Q. Peng, M. Gong, H. Rong, and Y. Li, *Angew. Chem. Int. Ed*., 2011, **50**, 6315–6319.
13. H. Lee, S. E. Habas, S. Kweskin, D. Butcher, G. A. Somorjai and P. Yang, *Angew. Chem. Int. Ed*., 2006, **45**, 7824–7828.
14. J. Zeng, Y. Zheng, M. Rycenga, J. Tao, Z. Li, Q. Zhang, and Y. Zhu, *J. Am. Chem. Soc*., 2010, **132**, 8552–8553.

15. W. Jung, S. Lee, D. Woo, S. Jeong, P. Miro, A. Kuc, T. Heine, and J. Cheon, *J. Am. Chem. Soc*., 2015, **2**, 7266-7269.
16. S. Campisi, M. Schiavoni, C. E. Chan-thaw and A. Villa, *Catalysts*, 2016, **6**, 1–21.
17. S. Mourdikoudis and L. M. Liz-Marzan, *Chem. Mater*., 2013, **25**, 1465-1476.
18. M. Zhou, Z. Zhang, K. Huang, Z. Shi, R. Xie, and W. Yang, *Nanoscale*, 2016, **2**, 15262–15272.
19. A. Bayat and E. Saievar-iranizad, *J. Lumin.*, 2017, **185**, 236–240.
20. C. Veenas, L. Asitha, V. Bose, A. Aiswarya Raj, G. Madhu, and V. Bij, *IOP. Conf. Series: Materials Science and Engineering*, 2015, **73**, 012119.
21. A. Berkdemir, H. R. Gutiérrez, A. R. Botello-Méndez, N. Perea-López, A. L. Elías, C.-I. Chia, B. Wang, V. H. Crespi, F. López-Urías, J.-C. Charlier, H. Terrones and M. Terrones, *Sci. Rep.*, 2013, **3**, 1755.
22. N. Peimyoo, J. Shang, W. Yang, Y. Wang and C. Cong, *Nano Res*., 2014, **8**, 1210-1221.
23. G. Gabka, P. Bujak, D. Zabost, K. Kotwica, K. Malinowska, A. Ostrowski, I. Wielgus, W. Lisowski, J. W. Sobczak, M. Przybylski and A. Pron, *Phys. Chem. Chem. Phys*., 2016, **18**, 15091–15101.
24. T. P. Nguyen, W. Sohn, J. H. Oh, H. W. Jang and S. Y. Kim, *J. Phys. Chem. C*, 2016, **120**, 10078-10085.
25. W. Zhao, Z. Ghorannevis, L. Chu, M. Toh, C. Kloc, P. Tan and G. Eda, *ACS Nano*, 2013, **7**, 791-797
26. T. Moon, J. Kim, J. Seo, Y. Jun, S. Park, H. Nah, T. Moon, B. Park, J. Kim, Y. J. Kim and J. Cheon, *Angew. Chem. Int. Ed*., 2007, **46**, 8828-8831.
27. J. Jang, S. Jeong, J. Seo, M. Kim, E. Sim, Y. Oh, S. Nam, B. Park and J. Cheon, *J. Am. Chem. Soc*., 2011, **133**, 7636–7639.
28. S. Cao, T. Liu, S. Hussain, W. Zeng and X. Peng, *Mater. Lett.*, 2014, **129**, 205–208.
29. H. Long, L. Tao, C. P. Chiu, C. Y. Tang and K. H. Fung, *Nanotechnology*, 2016, **27**, 414005.
30. S. Cao, C. Zhao, L. Peng and T. Han, *J. Mater. Sci. Mater. Electron.*, 2016, **27**, 3821–3825.
31. S. Koh and D. Lee, *MRS Commun*., 2018, **8**, 742–753.
32. K. Woo, J. Hong, J. Ahn, J. Park and K. Kim, *Inorg. Chem*., 2005, **44**, 7171–7174.

33. A. Weddemann, I. Ennen, A. Regtmeier, C. Albon, A. Wolff, K. Eckstädt, N. Mill, M. K. Peter, J. Mattay, C. Plattner, N. Sewald and A. Hütten, *Beilstein J. Nanotechnol*., 2010, **1**, 75–93.
34. T. A. J. Loh, D. H. C. Chua and A. T. S. Wee, *Sci. Rep*., 2015, **5**, 1–9.
35. Q. H. Wang, K. Kalantar-Zadeh, A. Kis, J. N. Coleman and M. S. Strano, *Nat. Nanotechnol.*, 2012, **7**, 699–712.

Chapter 4

Synthesis of WS_2 nanostructures with different tungsten precursors

4.1 Introduction

One of the most important parameter considerations in colloidal synthesis is the types of precursors used to form the monomers. The chemistry of the precursors and ligands determine the evolution of the nanoparticles over time.[1] Precursor reactivity influences the nanoparticle growth and growth rate.[2,3] For nanoparticles to begin growing, free monomers are required. These are obtained by the reaction of the precursors through reduction or thermal decomposition. The reactivity of the precursors is affected by the ligands they are bound to. For example, precursors with strongly bound ligands decompose slower than precursors with ligands that are weakly bound.[4] For the heat-up synthesis used in this study, the ideal precursors would be precursors that are stable at room temperature but can undergo rapid decomposition at elevated temperatures, preferably below 300 ℃. In ideal cases, the precursor should decompose at a rate that would allow for uniform nucleation.[1] This is usually a precursor that decomposes at a moderate rate, because when the nucleation rate is too high or too low, very wide size distributions and low yields occur.[1] It has been shown that precursors are able to influence the shape, size, composition, and yield of the resultant nanoparticles.[5] Arellano *et al.* showed that the morphology of CdSe nanoparticles could be changed with a variation of cadmium precursor. $CdCl_2$ produced spherical nanoparticles, while $Cd(NO_3)_2$ and $Cd(CH_3COO)_2$ formed agglomerated bar and rod-shaped nanoparticles respectively.[6]

Three different tungsten precursors are used in this study: $(NH_4)_{10}H_2(W_2O_7)_6$ (ammonium tungstate), $W(CO)_6$ (tungsten hexacarbonyl) and WCl_6 (tungsten hexachloride) as shown in Figure 4.1. Ammonium tungstate is a tungsten oxide that contains ammonium ions within its crystal structure.[7] It decomposes into WO_3 by the removal of water and ammonia gas.[8] WCl_6 and $W(CO)_6$ are organometallic precursors. WCl_6 is air and moisture sensitive[9] and has relatively weak W-Cl bonds which means that decomposition occurs faster compared to ammonium tungstate. $W(CO)_6$ has been said to be susceptible to oxidation[10] and decomposes at approximately 150 ℃[11] which is faster than ammonium tungstate as well.

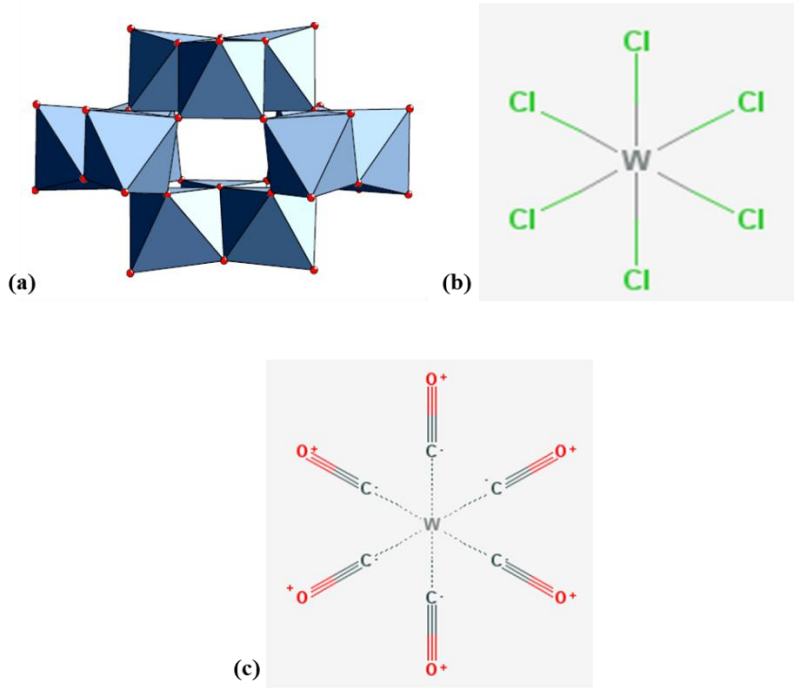


Figure 4.1: (a) Ammonium tungstate anion $[H_2W_{12}O_{42}]^{10-}$,[7] (b) WCl_6 and (c) $W(CO)_6$.

4.2 Methods and materials

4.2.1 Chemicals

Ammonium tungstate ($(NH_4)_{10}H_2(W_2O_7)_6$), tungsten hexachloride (WCl_6, 99.9% reagent grade), tungsten hexacarbonyl ($W(CO)_6$, 97%), thiourea (99% reagent grade), oleylamine (70% technical grade). All chemicals were obtained from Sigma Aldrich.

4.2.2 Experimental procedure

The tungsten precursor (ammonium tungstate or WCl_6 or $W(CO)_6$) was mixed with thiourea in a 1 mmol:4 mmol ratios at room temperature. Oleylamine (20 ml) was added to the mixture in a three-necked round bottom flask. The mixture was purged with N_2 gas for 20 minutes at room temperature. Thereafter the mixture was heated to 300 ℃ under N_2 gas. At 300 ℃, the reaction was timed for 1 hour before cooling. The resultant black product was washed several times with 1:1 volume of ethanol and hexane. The nanoparticles were re-dispersed in chloroform for characterization.

Ammonium tungstate-WS_2 indicates WS_2 synthesized using ammonium tungstate as precursor.

WCl_6-WS_2 indicates WS_2 synthesized using WCl_6 as precursor.

$W(CO)_6$-WS_2 indicates WS_2 synthesized with $W(CO)_6$ as precursor.

4.2.3 Characterization

Powder X-ray diffraction (PXRD) was carried out on the Bruker D2 diffractometer using CuKα radiation (λ 1.5406 Å) at 30 kV/30 mA. Raman and solid-state photoluminescence (PL) spectroscopy were done on the Horiba J-Y T64000 micro-Raman spectrometer. The excitation wavelength used for all samples was 514 nm. Fourier Transform Infrared (FT-IR) spectroscopy was performed on a Bruker Tensor 27 spectrometer. The UV-Vis absorption characteristics were measured with the Varian Cary Eclipse (Cary 50) UV-vis absorption spectrophotometer. Transmission electron microscopy (TEM) was done on the FEI Technai T12 microscope with an accelerating voltage of 120 kV. A JEOL JEM-2100 High-Resolution Transmission Electron Microscope (HRTEM) was used for further structural analysis. Scanning electron microscopy and energy dispersive spectroscopy (EDS) were performed on the FEI Nova Nanolab 600 microscope.

4.3 Results and discussion

PXRD and Raman spectroscopy were used to probe the crystal structure of the materials. The first noticeable trait seen from the PXRD patterns in Figure 4.2 (a) is that WS_2 prepared using ammonium tungstate is very crystalline and pure. The peaks all match to that of 2H- WS_2 (PDF: 00-084-1398). The pattern shows a high-intensity peak at 14° that corresponds to the (002) plane. This plane is related to the c-axis or the basal plane of the nanocrystals. The high intensity shows that the WS_2 has a well stacked, layered structure.[12] With the use of organometallic precursors, WCl_6 and $W(CO)_6$, the crystallinity of the material diminishes, as shown by the poor separation between the peaks. The (002) plane is absent in these patterns. There exists a plane at 18° that could be due to oxide by-products.[13,14] A shift to lower angles is observed for the (110) plane at 56° (marked with an asterisk) as well. This shift has been observed in WS_2 nanosheets and nanoworms that had been synthesized by Li *et al.*[13] The shifts were attributed to decreasing crystallinity. It is evident in the above patterns that the crystallinity of the materials has also decreased, which could be the reason for the shifts of the peaks. The (100) or (101) planes are asymmetrical; this indicates that the stacking of the sheets is turbostratic.[15] This means that the stacking of the basal planes is out of alignment. This is usually caused by the surface passivation of oleylamine that prevents the sheets from stacking in a perfectly ordered fashion.

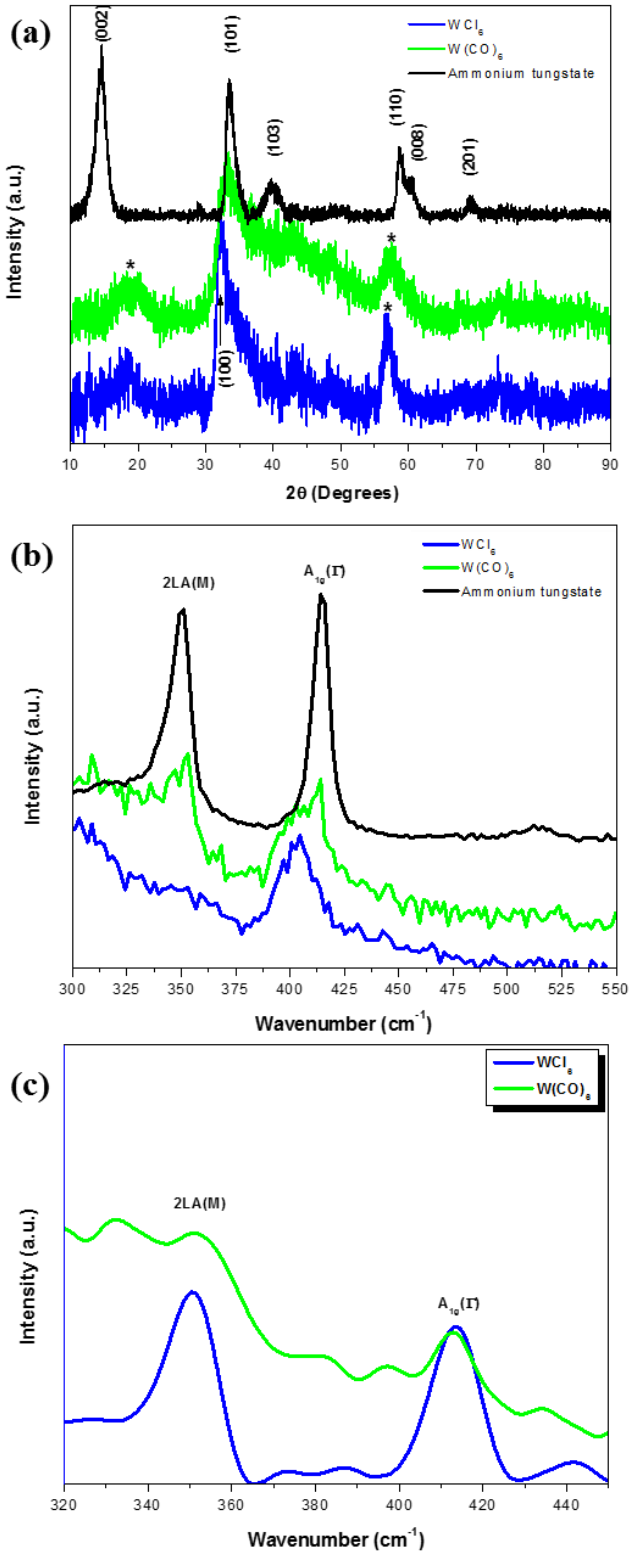


Figure 4.2: PXRD patterns (a) and Raman spectra (b) of WS_2 synthesized using three different tungsten precursors and (c) Raman spectra of the WCl_6 and $W(CO)_6$ samples at 532 nm excitation wavelength.

The Raman spectra in Figure 4.2 (b) also reveal significant differences between the materials synthesized with ammonium tungstate compared to those of WCl_6 and $W(CO)_6$. Firstly, the two main distinct peaks for WS_2 are prominent in the ammonium tungstate-WS_2, while they weaken when the organometallic precursors are used. This is due to the deterioration of the WS_2 crystal structure. From the PXRD patterns, it is evident that the crystallinity is deteriorated and the formation of mixtures and unknown products occurs which in turn means that the distinct 2H- WS_2 Raman modes are weakened or even absent. For the ammonium tungstate-WS_2, the 2LA(M) mode is situated at 350 cm^{-1} and the $A_{1g}(\Gamma)$ mode is situated at 415 cm^{-1}. For WS_2 with a few layers, the $A_{1g}(\Gamma)$ mode is expected between 419 cm^{-1} and 416 cm^{-1}.[16] The downshift of this peak could be due to localized heating of the sample which has been shown to cause a shift of Raman peaks to lower energies.[17,18] From the spectrum, it is clear that the $A_{1g}(\Gamma)$ intensity is higher than that of the 2LA(M) mode. The intensity ratio between the 2LA(M) and $A_{1g}(\Gamma)$ mode is 0.8, indicating that the WS_2 synthesized with ammonium tungstate has three to four layers.[16,19] This is in agreement with the high intensity of the (002) PXRD plane in Figure 4.2(a). Figure 4.2 (c) shows the Raman spectra of the materials produced with WCl_6 and $W(CO)_6$ at an excitation wavelength of 532 nm. The expected 2H-WS_2 modes are clearly present for the sample prepared with WCl_6, while they are weakened for the sample prepared with $W(CO)_6$.

The EDS spectra in Figure 4.3 indicate that for all three samples there exist sulfur and tungsten species as expected. The ammonium tungstate-WS_2 contains some oxygen species which could be oxides that exist on the surface of the material due to oxidation over time. The same is observed for the WCl_6-WS_2. The WS_2 produced through $W(CO)_6$ contains no oxygen species which suggests that no oxides were formed on the surface of the material.

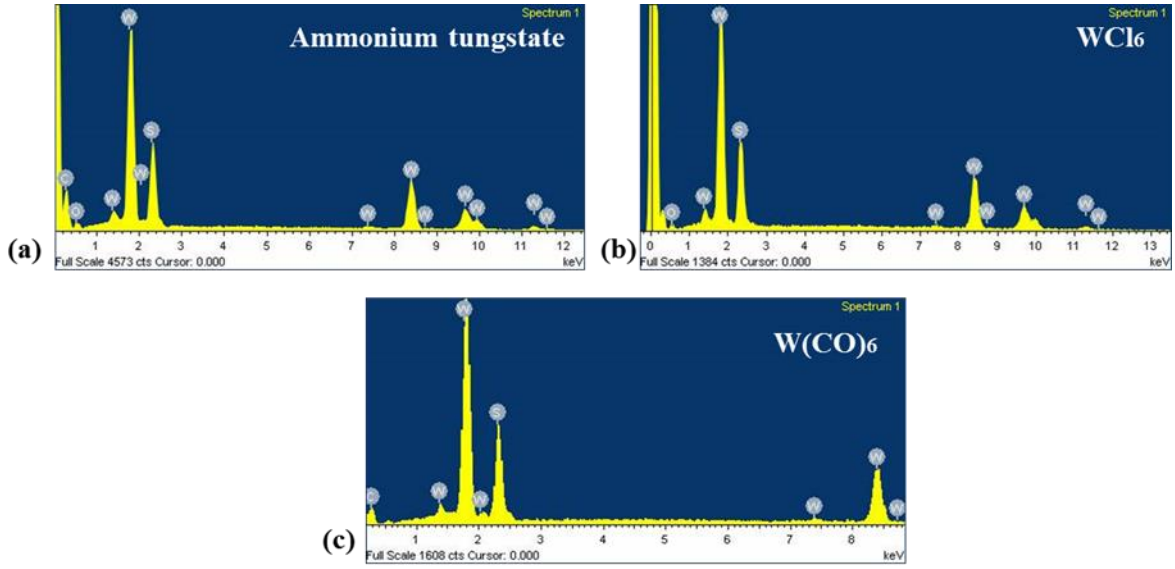


Figure 4.3: EDS spectra of WS_2 synthesized with (a) ammonium tungstate, (b) WCl_6 and (c) $W(CO)_6$.

The low magnification TEM image in Figure 4.4 (a) shows the WS_2 synthesized with ammonium tungstate that has formed a disk-like morphology. There also exists some elongated structures that are shown in Figure 4.4 (b) to be multi-layered WS_2 that is orientated sideways. It may be that the elongated structures occur when the disc-like structures are edge oriented. The interlayer spacing between the layers was measured to be 0.65 nm which is usually observed for 2H- WS_2.[20] Figure 4.4 (c) shows the HRTEM image of the flat disc-like WS_2 structures. Excellent crystallinity is observed which is in agreement with PXRD pattern. Further magnification into the area indicated by the yellow circle in Figure 4.4 (c), shows the hexagonal packing of 2H-WS_2 is observed (Figure 4.4 (d)). The d-spacing of the (101) plane is indicated in yellow to be 0.27 nm, which is characteristic of 2H-WS_2.[21–23] The SEM image (Figure 4.4 (e)) shows a large collection of flake-like structures with some edges exposed.

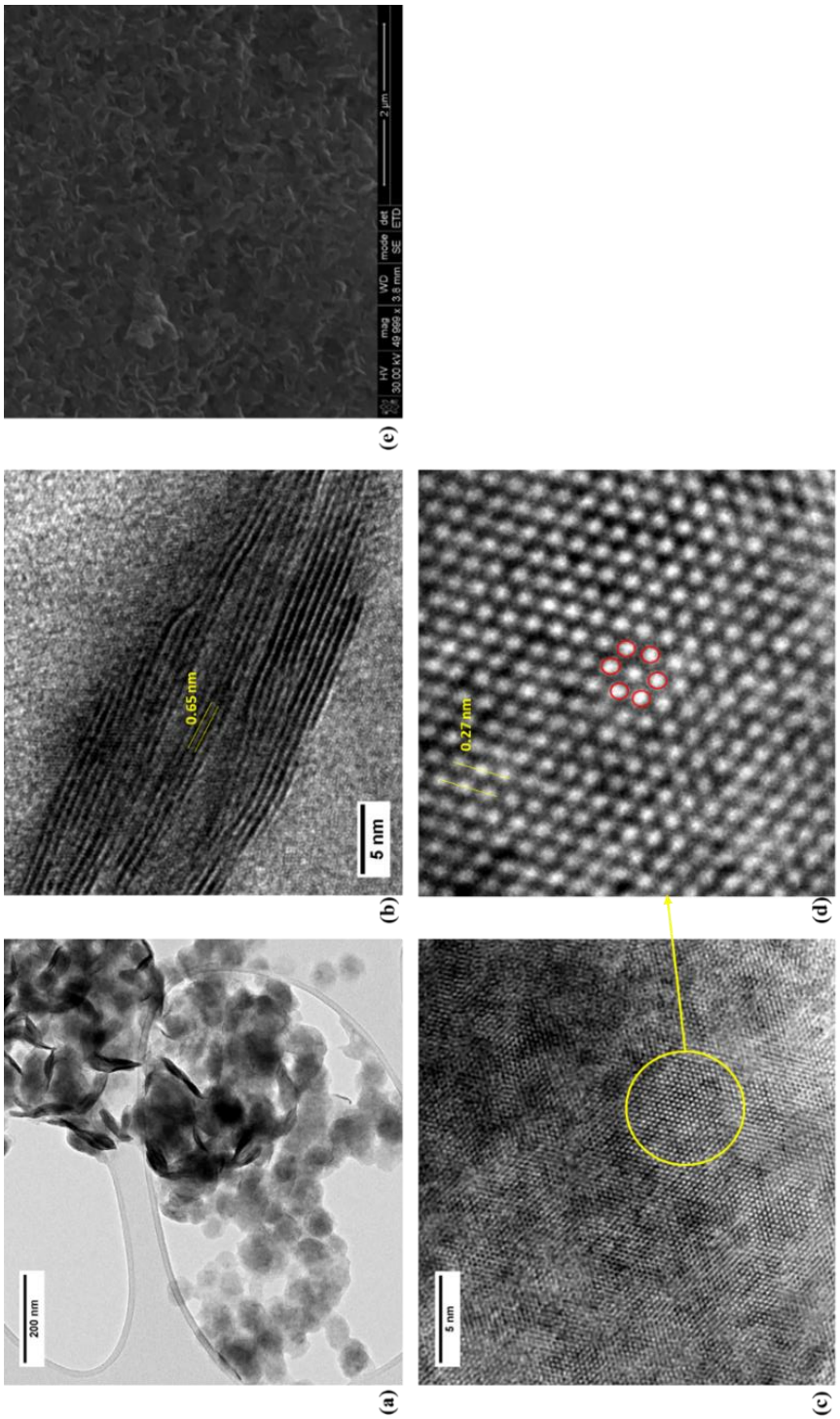


Figure 4.4: (a) TEM image showing WS_2 nanodisks and some curled up nanostructures. HRTEM images show the (b) layered structure of the WS_2, (c) the crystalline basal plane of the WS_2 and (d) magnified image of the basal plane showing the hexagonal crystal structure of WS_2. The SEM micrograph (e) of WS_2 disks/flakes synthesized from ammonium tungstate.

Figure 4.5(a) is a low magnification TEM image of the almost circular shaped particles produced from WCl_6. Figure 4.5(b) shows that there are highly crystalline areas and areas that are not very crystalline but contain wire-like structures. The wires are small and thin WS_2 layers where the basal plane or c-axis lies parallel to the electron beam. Figure 4.5(c) is an HRTEM image of the highly crystalline areas of the sample. Lattice fringes are clearly visible and their d-spacing was measured to 0.38 nm which corresponds to the (020) lattice plane of orthorhombic WO_3 (β-WO_3).[14] These images indicate that WCl_6 formed both WS_2 and WO_3. WCl_6 forms WO_2Cl_2 when in contact with air. WO_3 is easily formed from this tungsten dioxodichloride compound. The particles appear to be highly agglomerated in the SEM image (Figure 4.5(d)).

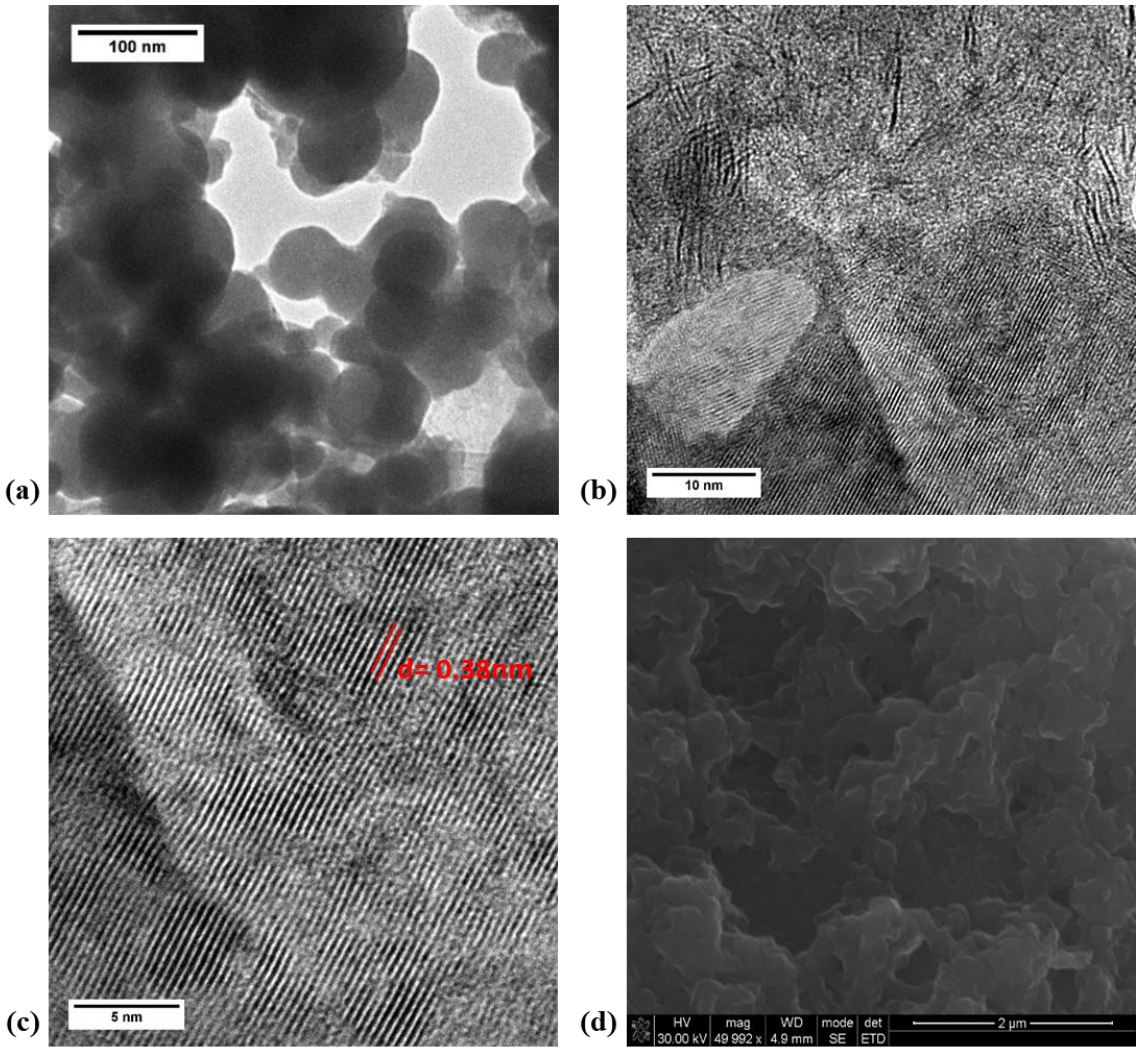


Figure 4.5: TEM (a), HRTEM (b, c) and SEM (d) micrographs of nanostructures synthesized with WCl_6.

The TEM images in Figure 4.6 show that some of the particles synthesized with $W(CO)_6$ have sheet-like morphology (b), while also having formed very small quantum dot-like material (a). The decreased crystallinity observed in the PXRD patterns, as well as the weak Raman modes, are caused by the size of these quantum dot-like materials. It is evident from the TEM images that the structures of the WS_2 change with the change in the precursor. This is related to the reactivity of the precursors. Ammonium tungstate is less reactive compared to $W(CO)_6$ and WCl_6. Ammonium tungstate decomposes into monomers at approximately 300 ℃, while $W(CO)_6$ decomposes at 150 ℃ and WCl_6 reacts immediately with oleylamine. According to kinetic and thermodynamic studies, highly reactive precursors cause faster nucleation and ultimately results in smaller particles.[2] This is also observed with the WS_2 produced from the organometallic precursors. WCl_6 forms the small, thin sheets while $W(CO)_6$ forms very small flakes. Ammonium tungstate produces larger WS_2 disks, due to its slower nucleation.

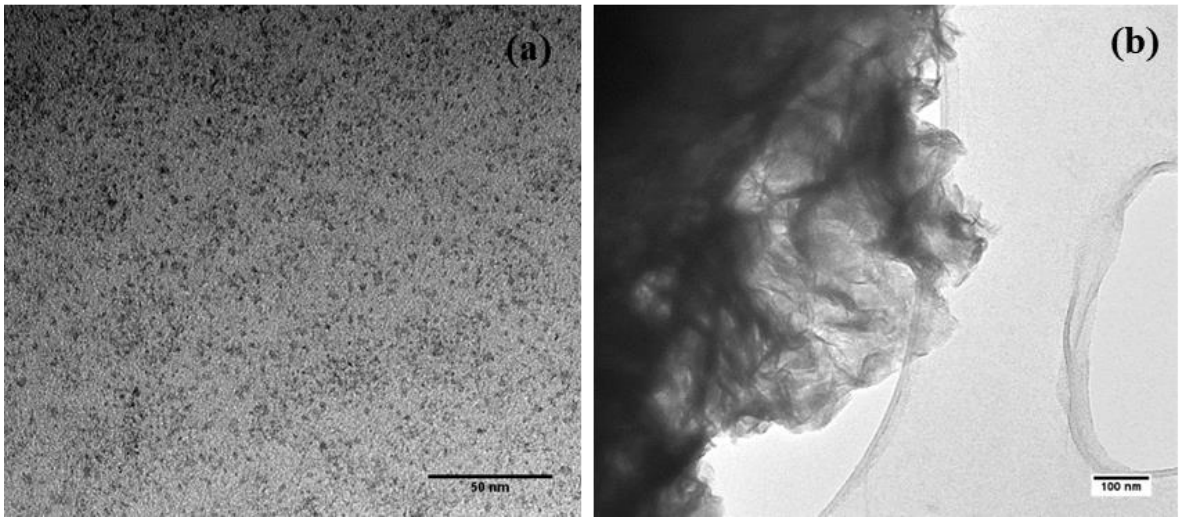


Figure 4.6: (a, b) TEM images of nanostructures synthesized using $W(CO)_6$.

FT-IR spectroscopy was used to determine whether oleylamine passivates the nanoparticles. The FT-IR spectra of pure oleylamine and of the WS_2 samples are depicted in Figure 4.7. It is clearly evident that some of the vibrational modes oleylamine are present in the WS_2 samples. The C─H stretches between 2800-2900 cm^{-1}, the CH_3 and C─H bends between 1250- 1500 cm^{-1}. The C─C bend is also present at 724 cm^{-1}. The double bond C=C stretch is also present at approximately 960 cm^{-1}. The modes that are of most interest are those belonging to the amine head group of oleylamine, as they may indicate how the capping agent is bonded onto the nanoparticles. There are two NH_2 bends situated at 1600 cm^{-1} and

795 cm^{-1}; a C─N bend at 1069 cm^{-1} and an NH_2 stretch at 3300 cm^{-1}. On all the particles the NH_2 stretch at 3300 cm^{-1} disappears, while both NH_2 bends at 1600 cm^{-1} and 795 cm^{-1} are present. These are more pronounced in the particles synthesized with WCl_6 and $W(CO)_6$. It is possible that the oleylamine is adsorbed onto the nanoparticles with the lone pair on the nitrogen atom while leaving both N─H bonds intact. It is evident that oleylamine has passivated the nanoparticles. For the ammonium tungstate-WS_2, the NH_2 stretch and bends are not present, which indicates that oleylamine is chemisorbed onto the WS_2.

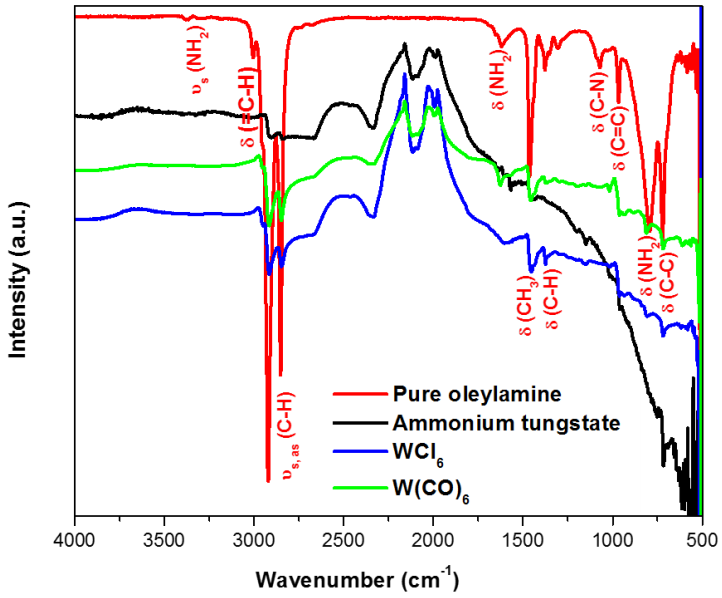


Figure 4.7: FT-IR spectra of pure oleylamine, as well as WS_2, synthesized with ammonium tungstate, WCl_6, and $W(CO)_6$.

Three absorption peaks are observed for the ammonium tungstate synthesis which is characteristic of 2H-WS_2. The A-B excitonic pair and exciton C are observed at 625 nm, 523 nm, and 461 nm respectively. The peaks A and B are the direct excitonic transitions that occur at the K-point of the Brillouin zone, between the conduction band and the split valence band.[24] The splitting of the valence band is caused by spin-orbit coupling between layers.[25] Exciton C is the optical transitions between densities of state in the valence and conduction bands.[23] The optical band gap, based on the longest wavelength absorption at 625 nm is approximately 1.9 eV, which is a significant blue shift from the bulk WS_2 band gap of 1.3

eV. This blue shift is an indication of the quantum confinement that exists within the ammonium tungstate-WS_2.[18]

The PL of the ammonium tungstate sample has a very weak emission at 658 nm and a stronger emission at 603 nm as well as 550 nm. The peaks just above 550 nm are attributed to the emission of the carbon peaks and the peak at 603 nm could be the second order emission of the carbon peaks. The weak emission at 658 nm could be attributed to the direct A-exciton of WS_2.[24] The very weak emission is caused by the presence of more than one layer of WS_2. The same is not observed with the materials synthesized with $W(CO)_6$ and WCl_6. Their optical absorption begins at 552 nm and 566 nm for $W(CO)_6$ and WCl_6 respectively. The tailing of the absorption spectra in Figure 4.8(a) is due to the presence of particles of different sizes as shown by the TEM and SEM images of both WCl_6-WS_2 and $W(CO)_6$-WS_2.

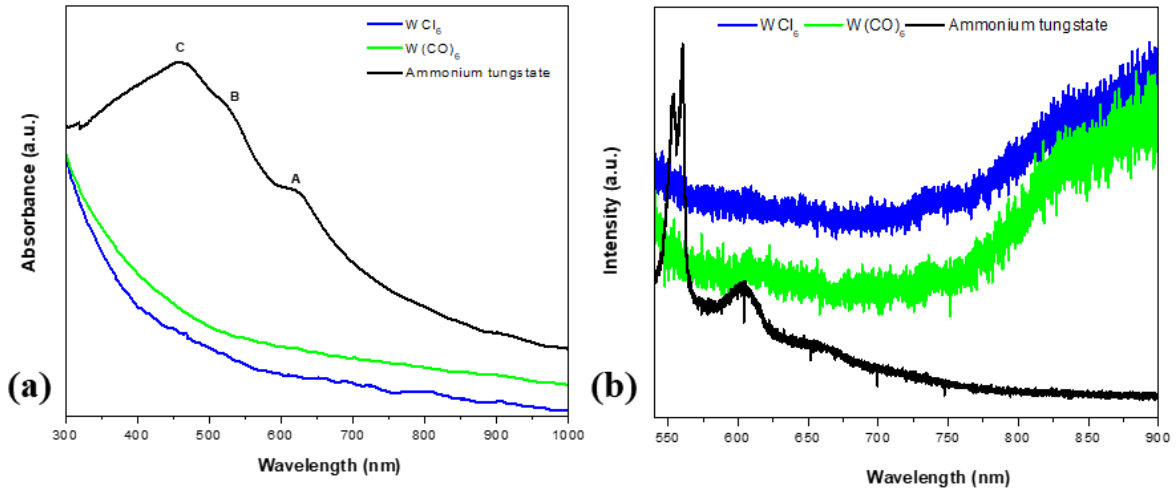


Figure 4.8: UV-Vis absorption (a) and PL emission (b) spectra of the WS_2 produced from ammonium tungstate (black), WCl_6 (blue) and $W(CO)_6$ (green).

4.4 Proposed Mechanisms

Thiourea is the common sulphur precursor used in this study. According to a theoretical study done by Wang *et al.*[26] on the thermal decomposition of thiourea, it is able to undergo several primitive decomposition pathways. It was concluded that thiourea undergoes 2 main pathways. These pathways commonly end up with the formation of NH_3, H_2S and other carbon-containing intermediates such as carbodiimide or isothiocyanic acid. Apart from

theoretical studies, experimental studies have been conducted where it was found that the main gaseous decomposition products of thiourea are NH_3, CS_2, and H_2S. This occurs mainly between 180 and 240 ℃.[27,28] In the case of the formation of WS_2, it is proposed that H_2S or CS_2 are the active species that play a role in sulfurizing the tungsten precursor/intermediate to form WS_2.

$$CS(NH_2)_2 \underset{\Delta}{\rightarrow} H_2S_{(g)} + HN{=}C{=}NH_{(g)} \qquad (4.1)$$

or

$$2CS(NH_2)_2 \underset{\Delta}{\rightarrow} CS_{2\,(g)} + H_2N{-}C{\equiv}N_{(g)} + 2NH_{3\,(g)} \qquad (4.2)$$

(i) Ammonium tungstate

Thermal decomposition of ammonium tungstate:

$$(NH_4)_{10}H_2(W_2O_7)_6 \cdot 4H_2O \xrightarrow{RT-110℃} (NH_4)_{10}H_2(W_2O_7)_6 + 4H_2O_{(g)} \quad (4.3)$$

$$(NH_4)_{10}H_2(W_2O_7)_6 \xrightarrow{180-225℃} 3(NH_4)_2O \cdot 12(WO_3) \cdot 3H_2O + 4NH_{3\,(g)} \quad (4.4)$$

$$3(NH_4)_2O \cdot 12(WO_3) \cdot 3H_2O \xrightarrow{230-300℃} 12WO_{3\,(s)} + 6NH_{3\,(g)} + 6H_2O_{(g)}.^{7,8,29} \quad (4.5)$$

Formation of WS_2:

Based on the decomposition of thiourea, WS_2 can be formed in three ways:

$$2WO_{3\,(s)} + 3CS_{2\,(g)} \xrightarrow{\Delta} 2WS_{2\,(s)} + 3CO_{2\,(g)} + 2S \text{ or } (4.6)$$

$$WO_{3\,(s)} + 2H_2S_{\,(g)} \xrightarrow{\Delta} WS_{2\,(s)} + H_2O_{(g)} + H_{2\,(g)} \text{ or } \quad (4.7)$$

$$2WO_{3\,(s)} + 4H_2S_{\,(g)} \xrightarrow{\Delta} 2WS_{2\,(s)} + 4H_2O_{(g)} + O_{2\,(g)} \quad (4.8)$$

Equation 4.8 is an unlikely reaction as the oxygen that is evolved would re-oxidize the WS_2, turning it back into WO_3. The purity of the product observed on the PXRD pattern indicates that there is minimal re-oxidation.

(ii) WCl_6

WCl_6 can react with OLA to form a W-OLA complex.[15] This complex could have prevented the formation of large WS_2 sheets because of the long carbon chains of oleylamine cause steric repulsion. Instead, very short/small WS_2 sheets were formed as seen on the HRTEM image in Figure 4.5. There was a gas evolved when WCl_6 was added to the oleylamine in the reaction flask as shown in Figure 4.9(a). This gas could have occurred when the oleylamine-W complex was formed, causing the evolution of HCl gas. When WCl_6 was being added to

the reaction flask, it was exposed to moisture in the air and that caused a slight reaction as WCl_6 is unstable in air. The reaction with air caused the dark blue WCl_6 to turn into the yellow WO_2Cl_2 as shown in Figure 5.9(b). Tungsten dioxide dichloride is also an air sensitive compound that is usually used as a precursor for the formation of WO_3.[30] The WO_3 that was observed possibly came from the WO_2Cl_2 compound. WCl_6 has also been found that when it reacts with H_2S, it forms WCl_xS_y intermediates[31,32] before the formation of WS_2. This may be the cause of the PXRD peaks that are unaccounted for. Equation 4.9 and 4.10 show the possible pathways in which WO_3 and WS_2 could be formed.

$$WCl_6 \xrightarrow{air} WO_2Cl_2 \longrightarrow WO_3 \text{ (Scheme 4.9)}$$

$$WCl_6 \xrightarrow{Oleylamine} W - oleylamine + H_2S \text{ or } CS_2 \longrightarrow WS2 + WCl_xS_y \text{ (4.10)}$$

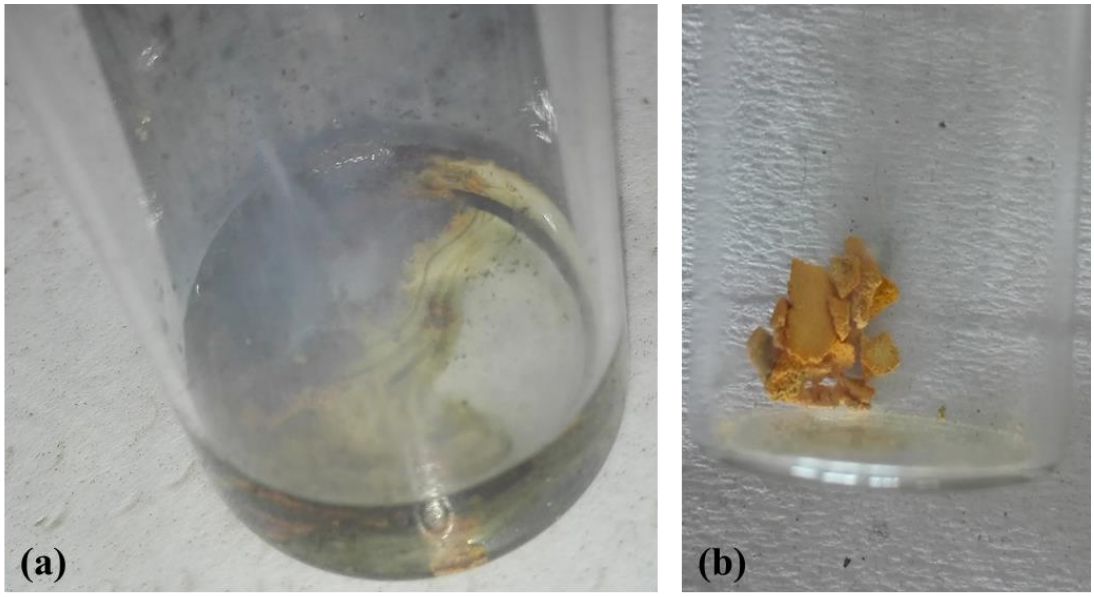


Figure 4.9: (a) White HCl gas evolved when WCl_6 is added to oleylamine and (b) WO_2Cl_2 solid that forms when WCl_6 is exposed to air.

(iii) $W(CO)_6$

From previous studies done on the synthesis of WS_2 from $W(CO)_6$, it has been shown that $W(CO)_6$ decomposes at 150 ℃ [11]:

$$W(CO)_6 \xrightarrow{\Delta} W + 6\,CO \text{ (4.11)}$$

From the Boudouard reaction it is shown that carbon monoxide can form carbon dioxide and graphite:

$2CO \rightarrow CO_2 + C$ (4.12) [33]

It was reported by Pol *et al*. that WO_x can be formed by the dissociation of CO or CO_2 to form oxygen that in turn oxidizes the W to WO_x.[33] Metal carbonyls have been reported to be susceptible to oxidation by air to form a metal oxide and CO or CO_2.[10] From the WO_x, WS_2 can be formed by reaction with H_2S or CS_2 as shown in equation 4.6 and 4.7.It is not clear what other by-products could have been formed.

4.5 Conclusion

The colloidal synthesis of WS_2 is sensitive to the type of precursors used. Using different precursors affects the crystal structure and the optical properties of the material as well as the morphology. It was clearly seen that when organometallic precursors are used, the crystal structure, morphology, and optical properties change significantly. WCl_6 is unstable in ambient conditions and easily reacts with moisture and air, which makes it an unsuitable precursor to use in heating up colloidal synthesis. It also produces a mixture of small WS_2 nanosheets and WO_3 particles. The air and moisture sensitivity of WCl_6 causes the formation of WO_2Cl_2 that further reacts to form WO_3. $W(CO)_6$ produces a mixture of WS_2 sheets and very small quantum dot-like flakes. The products produced have decreased crystallinity. The difference in the types of products formed comes from the fast nucleation that occurs. Ammonium tungstate is an ideal precursor to use as it produces highly crystalline and high purity WS_2 disk-like structures. The WS_2 produced from ammonium tungstate absorbs visible light and exhibits photoluminescence which is beneficial in the solar cell and other optoelectronic applications. The exposed edges observed from this synthesis also make the WS_2 suitable for electrocatalytic applications such as electrodes in dye-sensitized solar cells. WCl_6 and $W(CO)_6$ are not ideal precursors to be used in the heating up, colloidal synthesis of WS_2 as they produce materials with decreased crystallinity and also undergo side reactions that form oxide by-products. Oleylamine has been shown to passivate the WS_2 nanoparticles in all three cases, however, it cannot be said that oleylamine affects the morphology of the WS_2 that arises as it appears that the tungsten precursors are affecting the morphology in this case.

4.6 References

1. J. Van Embden, A. S. R. Chesman and J. J. Jasieniak, *Chem. Mater*., 2015, **27**, 2246-2285.
2. K. L. Sowers, B. Swartz, and T. D. Krauss, *Chem. Mater*., 2013, **25**, 1351-1362.

3. S. Koh and D. Lee, *MRS Communications*, 2018, **8**, 742–753.
4. M. Nasilowski, B. Mahler, E. Lhuillier, S. Ithurria and B. Dubertret, *Chem. Rev*., 2016, **116**, 10934-10982.
5. L. C. Frenette and T. D. Krauss, *Nat. Commun*., 2017, **8**, 1–8.
6. J. S. Arellano, E. Rosendo and R. Galeazzi, *Advanced Materials Research*, 2014, **976**, 52-58.
7. O. Kirilenko, P. Hildebrandt and T. Ressler, *Doctoral dissertation, Technische Universität Berlin*, 2005.
8. G. J. French and F. R. Sale, *Journal of Material Science*, 1981, **16**, 3427–3436.
9. S. Dolci, F. Marchetti, G. Pampaloni and S. Zacchini, *Dalton Trans*., 2013, **42**, 5635-5648.
10. D. Shriver, P. Atkins, T.L. Overton, J. P. Rourke, M.T. Weller and F.A. Armstrong, Inorganic Chemistry 4th Ed., 2016.
11. N. Zink, J. Pansiot, J. Kieffer, H. A. Therese, M. Panthöfer, F. Rocker, U. Kolb and W. Tremel, *Chem. Mater*., 2007, **19**, 6391–6400.
12. X. Lin, J. Ge and Y. Li, *Chem. Eur. J.*, 2004, **10**, 6163-6171.
13. H. Yan, J. Li, D. Liu, X. Jing, D. Wang and L. Meng, *CrystEngComm*., 2018, **20**, 2324–2330.
14. Z. Shen, M. Wang, L. Liu, M. V. So, H. Yang, S. Wang and S. Liu, *Electrochimica Acta*, 2018, **266**, 130–138.
15. L. Cheng, W. Huang, Q. Gong, C. Liu, Z. Liu and Y. Li, *Angew. Chem. Int. Ed*., 2014, **53**, 7860–7863.
16. A. Berkdemir, H.R. Gutiérrez, A.R. Botello-Méndez, N. Perea-López, A.L. Elías, C.I. Chia, B. Wang, V.H. Crespi, F. López-Urías, J.C. Charlier and H. Terrones, *Sci. Rep.*, 2013, **3**, 1755.
17. N. Peimyoo, J. Shang, W. Yang, Y. Wang and C. Cong, *NanoRes.*, 2014. **8**, 1210-1221.
18. A. K. Mishra, K. V Lakshmi and L. Huang, *Sci. Rep*., 2015, **5**, 1–8.
19. T. A. J. Loh, D. H. C. Chua and A. T. S. Wee, *Sci. Rep*., 2015, **5**, 18116.
20. J. Yang, D. Voiry, S. J. Ahn, D. Kang, A. Y. Kim, M. Chhowalla and H. S. Shin, *Angew. Chem. Int. Ed*., 2013, **52**, 13751–13754.
21. Z. Jiang, Y. Zhang, G. Yang, J. Ma, S. Zhang, L. Yu and P. Zhang, *Ind. Eng. Chem. Res*., 2017, **56**, 1365-1375.

22. Y. Kim, J. Song, Y. J. Park, G. H. Ryu, S. J. Lee, J. S. Kim, P. J. Jeon, C. W. Lee, W. J. Woo, T. Choi, H. Jung, H. Lee, J. Myoung, S. Im, Z. Lee, J. Ahn, J. Park and H. Kim, *Sci. Rep*., 2016, **6**, 18754.
23. M. Zhou, Z. Zhang, K. Huang, Z. Shi, R. Xie and W. Yang, *Nanoscale*, 2016, **2**, 15262–15272.
24. H. Long, L. Tao, C. P. Chiu, C. Y. Tang and K. H. Fung, *Nanotechnology*, 2016, **27**, 414005.
25. M. Chhowalla, H. S. Shin, G. Eda, L. Li, K. P. Loh and H. Zhang, *Nature Chemistry*, 2013, **5**, 263-275.
26. Z. D. Wang, M. Yoshida and B. George, *Comput. Theor. Chem*., 2013, **1017**, 91–98.
27. V. P. Timchenko, A. L. Novozhilov and O. A. Slepysheva, *Russian Journal of General Chemistry*, 2004, **74**, 1046–1050.
28. 2S. Wang, Q. Gao and J. Wang, *J. Phys. Chem. B*, 2005, **109**, 17281–17289.
29. M. J. G. Fait, H. Lunk, M. Feist, M. Schneider, J. N. Dann and T. A. Frisk, *Thermochimica Acta*, 2008, **469**, 12–22.
30. M. Bortoluzzi, C. Evangelisti, F. Marchetti, G. Pampaloni and F. Piccinelli, *Dalton Trans*., 2016, **45**, 15342-15349.
31. A. Prabakaran, F. Dillon, J. Melbourne, L. Jones, R. J. Nicholls, P. Holdway, J. Britton, A. A. Koos, A. Crossley, P. D. Nellist and N. Grobert, *Chem. Commun*., 2014, **50**, 12360–12362.
32. A. Margolin, F. L. Deepak, Y. Feldman and R. Tenne, *Nanotechnology*, 2008, **19**, 095601.
33. V. G. Pol, S. V. Pol, N. Perkas and A. Gedanken, *J. Phys. Chem. C*, 2007, **111**, 134–140.

Chapter 5

Synthesis of WS_2 using thiourea, thioacetamide, and N, N'-diphenyl thiourea as sulphur precursors

5.1 Introduction

Over the years, with further development of the colloidal synthesis of nanocrystals, it has been established that the specific synthetic procedure determines the characteristics of the nanocrystals formed. The reactivity of the precursors and the order in which the precursors are added play a role in the resultant size distribution of the crystals as well as the optical and electronic properties. Zhang *et al.* studied the effects of elemental sulphur, thiourea, and thioacetamide on CdS nanocrystals.[1] Elemental sulphur yielded CdS nanocrystals that were highly monodispersed, but with very low quantum efficiency. The CdS nanocrystals synthesized with thiourea were large and polydispersed as a result of rapid nucleation, while thioacetamide produced monodispersed CdS nanocrystals.[1] Li *et al.* also investigated the effect of sodium sulphide, thiourea and elemental sulphur on CdS nanocrystals. The sulphur precursors affected the resultant crystal phase of the materials as well as the morphology (from nanospheres to nanorods) and also the photoluminescence properties.[2] The effects on the properties were attributed to the reactivity or decomposition rates of the precursors. With high decomposition rates, S^{2-} ions are released rapidly, leading to the rapid nucleation of nanocrystals. In the CdS case, it was found that the faster nucleation led to more spherical nanocrystals and as the nucleation rate decreased, more anisotropic growth into rods occurred.[2]

The effect of the sulphur precursors was also shown in layered, early transition metal dichalcogenides such as TiS_2.[3] It was shown that using CS_2 as a sulfur source yielded TiS_2 nanodiscs, while elemental sulphur yielded materials of poor quality. The difference was in the sulfur radicals that elemental sulfur formed which were very reactive, causing the degradation of the TiS_2 that had been formed in the process.[3] For metal sulphide colloids, the nucleation step has been shown to be influenced by the S or Se precursor. In order for nucleation to begin, the S precursor bonds have to break, while the by-products can act as coordinating ligands for the nanoparticles. This means that the relative stabilities or reactivities of the precursors are a crucial factor in determining the formation of the nanocrystals as well as the final morphology of the nanocrystals.[4] In this study, three different

sulfur precursors (thiourea, thioacetamide and diphenyl thiourea) shown in Figure 5.1 have been used to synthesize WS_2 nanostructures. Thioacetamide and diphenyl thiourea are both derivatives of thiourea which means that the reactivity can be compared using their chemical structures.

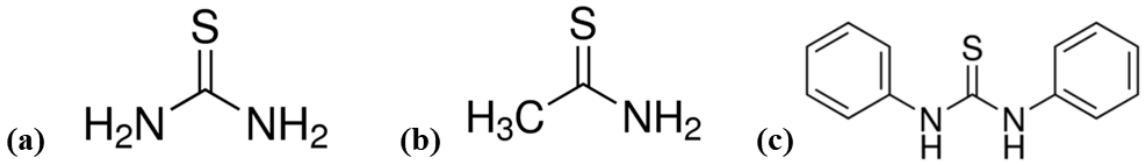


Figure 5.1: Chemical structures of (a) thiourea, (b) thioacetamide and (c) diphenyl thiourea.

5.2 Method and materials

5.2.1 Chemicals

Thiourea ($CS(NH_2)_2$, 99% reagent grade), thioacetamide (CH_3CSNH_2, 98% reagent grade), diphenyl thiourea ((Ph)NHCSNH(Ph)), tungstic acid (H_2WO_4, 99%) and oleylamine (70% technical grade).

5.2.2 Experimental procedure

About 4 mmol of the sulfur precursor was mixed with 1 mmol of tungstic acid in 20 mL oleylamine at room temperature in a three-necked round bottom flask. The mixture was purged with N_2 gas for 20 min at room temperature. Thereafter, the mixture was heated to 300 ℃ under N_2 gas. The reaction was timed for one hour after it had reached 300 ℃. Aliquots were extracted at the 30 min interval. After one hour, the reaction was cooled down to room temperature. The black product was washed with equal parts of ethanol and hexane and then air dried before characterization. The dry powder was re-dispersed in chloroform for other characterization methods.

5.2.3 Characterization

Powder X-ray diffraction (PXRD) was carried out on the Bruker MeasSrv (D2-205530)/D2205530 diffractometer using CuKα radiation (λ 1.5406 Å) at 30 kV/30 mA. Raman and solid-state photoluminescence (PL) spectroscopy were performed on a Horiba J-Y T64000 micro-Raman spectrometer. The excitation wavelength used for all samples was 514 nm. Fourier Transform Infrared (FT-IR) spectroscopy was performed on a Bruker Tensor

27 spectrometer. The UV-Vis absorption characteristics were measured with the Varian Cary Eclipse (Cary 50) UV-vis absorption spectrophotometer. Transmission electron microscopy (TEM) was carried out on the FEI Technai T12 microscope with an accelerating voltage of 120 kV. Scanning electron microscopy (SEM) and energy dispersive spectroscopy (EDS) was performed on the FEI Nova Nanolab 600 microscope.

5.3 Results and discussion

PXRD was used to probe the crystal structure of the materials produced. From the PXRD patterns in Figure 5.2, it is evident that 2H-WS_2 was produced with all three sulphur precursors as the peaks match those of the PDF: 01-084-1398 card number. From the patterns, the (002) plane is present, indicating a well-stacked layered structure.[5] The peak intensities are able to give an indication of the crystal planes that are dominant[6] and in this case, the (101) plane is dominant over the (002) plane. This indicates that the planes on the edge sites of the material are dominant over the basal plane .[6–8] The asymmetry of the (110) plane at 58° indicates that the stacking of the layers is out of alignment due to the surface passivation by oleylamine .[9] The crystallinity of the WS_2 seems to decrease for thioacetamide and thiourea derived WS_2. From the diphenyl thiourea pattern, there is a good separation between the (101), (103) and (105) planes, but the separations decrease when thioacetamide is used and even more when thiourea is used. Some WO_3 impurities are present, indicated by the red (001) index at 24°. The WO_3 is attributed to the oxidation of WS_2 at high temperatures. The impurity peak at 25° for the thiourea pattern is due to some unreacted tungstic acid (JCPDS -ICDD pattern no: 84-0886).[10]

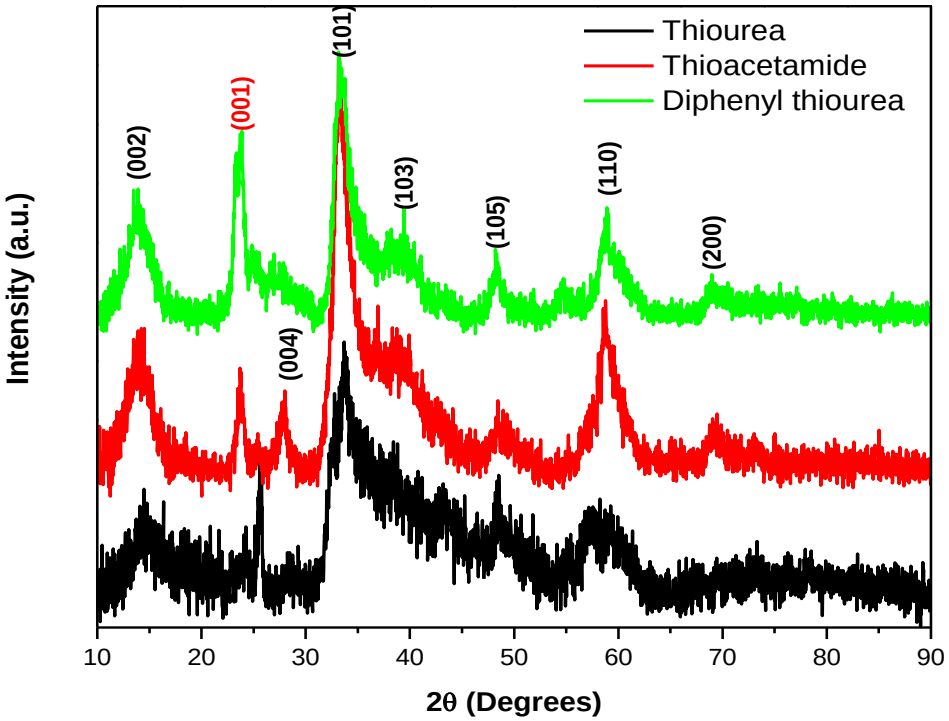


Figure 5.2: PXRD patterns for WS_2 obtained from thiourea, thioacetamide and diphenyl thiourea at 60 min reaction time.

Raman spectroscopy was used as an additional method to probe the crystal structure of the WS_2 produced. Two main Raman peaks are visible on the Raman spectra in Figure 5.3. The 2LA(M) and the $A_{1g}(\Gamma)$ modes. The WS_2 from thiourea and diphenyl thiourea exhibit similar spectra, with the 2LA(M) mode situated at 353 cm^{-1} and the $A_{1g}(\Gamma)$ mode at 418 cm^{-1}. These frequencies indicate that the nanosheets obtained from these two precursors are approximately two layers thick.[11] The intensity ratios of the 2LA(M) to the $A_{1g}(\Gamma)$ mode, as shown in Table 5.1, are 1.4 and 1.1 for thiourea and diphenyl thiourea respectively, indicating the formation of two-layer nanosheets.[7,11] The modes for the thioacetamide reaction, however, have shifted to lower frequencies; 350 cm^{-1} for the 2LA(M) mode and 415 cm^{-1} for the $A_{1g}(\Gamma)$ mode. The downward shift of the $A_{1g}(\Gamma)$ mode usually indicates the formation of fewer layers of WS_2, which can only be monolayer WS_2. However, it is not the case here. The PXRD pattern for the thioacetamide-WS_2 possesses a (002) plane, indicating the presence of more than one layer. So the downward shift of the Raman modes may be caused by localized heating of the sample that occurs when the laser-induced heat causes an increase in the temperature of the area of the sample where the laser is focused. This local increase in temperature has been shown to cause a redshift of the $A_{1g}(\Gamma)$ mode.[12] This could also indicate that the WS_2 produced from thioacetamide has poorer thermal conductivity. The

intensity ratio of the 2LA(M) to the $A_{1g}(\Gamma)$ mode for the thioacetamide-WS_2 is 1.5, again indicating the presence of double layer WS_2. Due to the excitation wavelength of 514 nm, the intensity of the 2LA(M) mode is higher than that of the $A_{1g}(\Gamma)$ mode in all three cases. This is because of the double resonance process that occurs when the excitation wavelength is so close to the B-exciton of the material.[7]

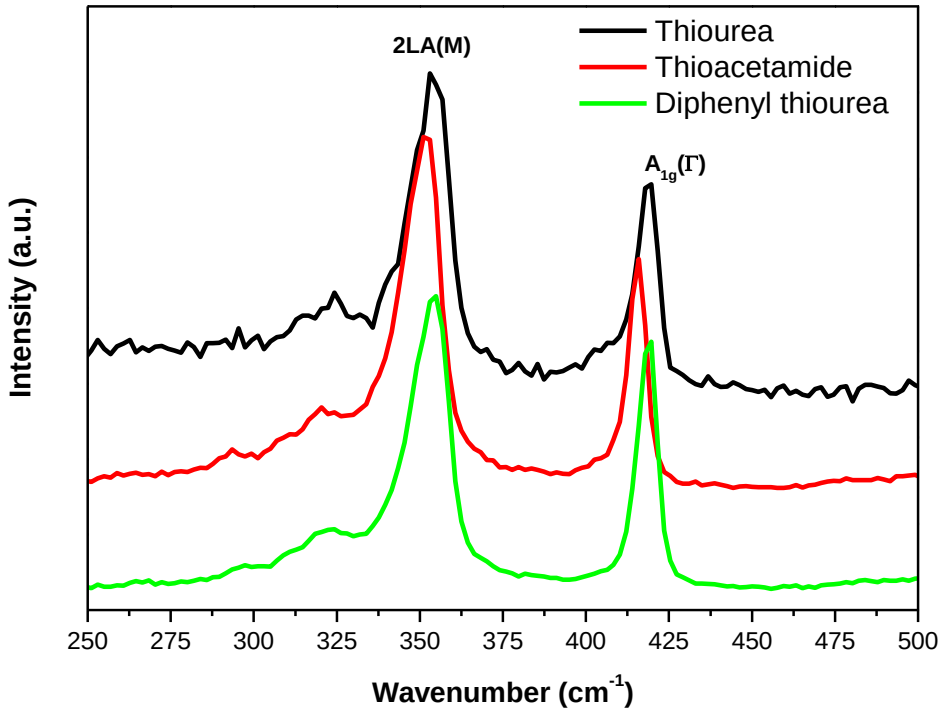


Figure 5.3: Raman spectra of WS_2 obtained from thiourea, thioacetamide and diphenyl thiourea of the 60 min reaction time.

Table 5.1: Raman shifts of 2LA(M) and $A_{1g}(\Gamma)$ modes, including the intensity ratios

	2LA(M)	**$A_{1g}(\Gamma)$**	$I_{2LA(M)} / I_{A_{1g}(\Gamma)}$
Thiourea	353.4 cm^{-1}	418.5 cm^{-1}	1.4
Thioacetamide	350.2 cm^{-1}	415.5 cm^{-1}	1.5
Diphenyl thiourea	353.2 cm^{-1}	418.6 cm^{-1}	1.1

The TEM images (Figure 5.4 (a)) show that at 30 minutes the WS_2 particles formed are flat, almost circular structures that attach to each other. Eventually, these structures form a flower-like morphology as shown in Figure 5.4 (b). The flower-like morphology is also shown on the SEM image in Figure 5.4 (c). The 'flowers' seem to be aggregations of small nanosheets into three dimensional, almost spherical flowers. The edges of the sheets can be seen from the SEM image (Figure 5.4(c)) as well. The flowers do not seem to be monodispersed in terms of size. The petals do not seem to be growing from a central core but are randomly oriented against each other.

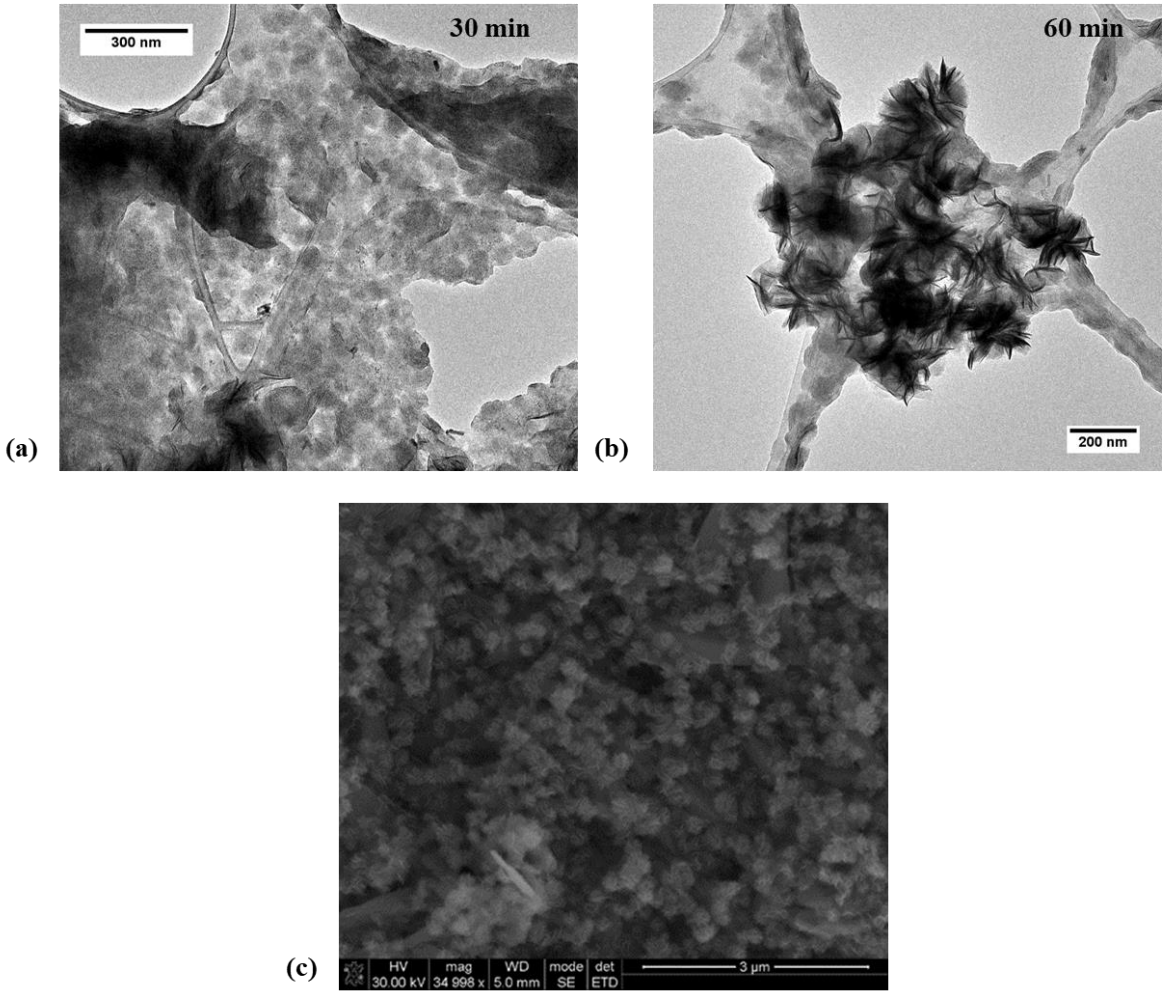


Figure 5.4: TEM images of WS_2 synthesized with thiourea for (a) 30 and (b) 60 minutes and a (c) SEM image of the 60 minute WS_2.

Figure 5.5 (a, b) show the TEM images for WS_2 produced from thioacetamide. It shows that thioacetamide forms crumpled or folded WS_2 sheets. Wrinkling and scrolling can be seen in the nanosheets that are reminiscent of the wrinkling seen in graphene sheets.[13] They also show that the nanosheets start off small and grow into the larger, crumpled sheets as shown in Figure 5.5 (b). The SEM image (Figure 5.5 (c)) shows some sheet edges, however, the sheets are highly agglomerated, making it difficult to deduce any other surface features.

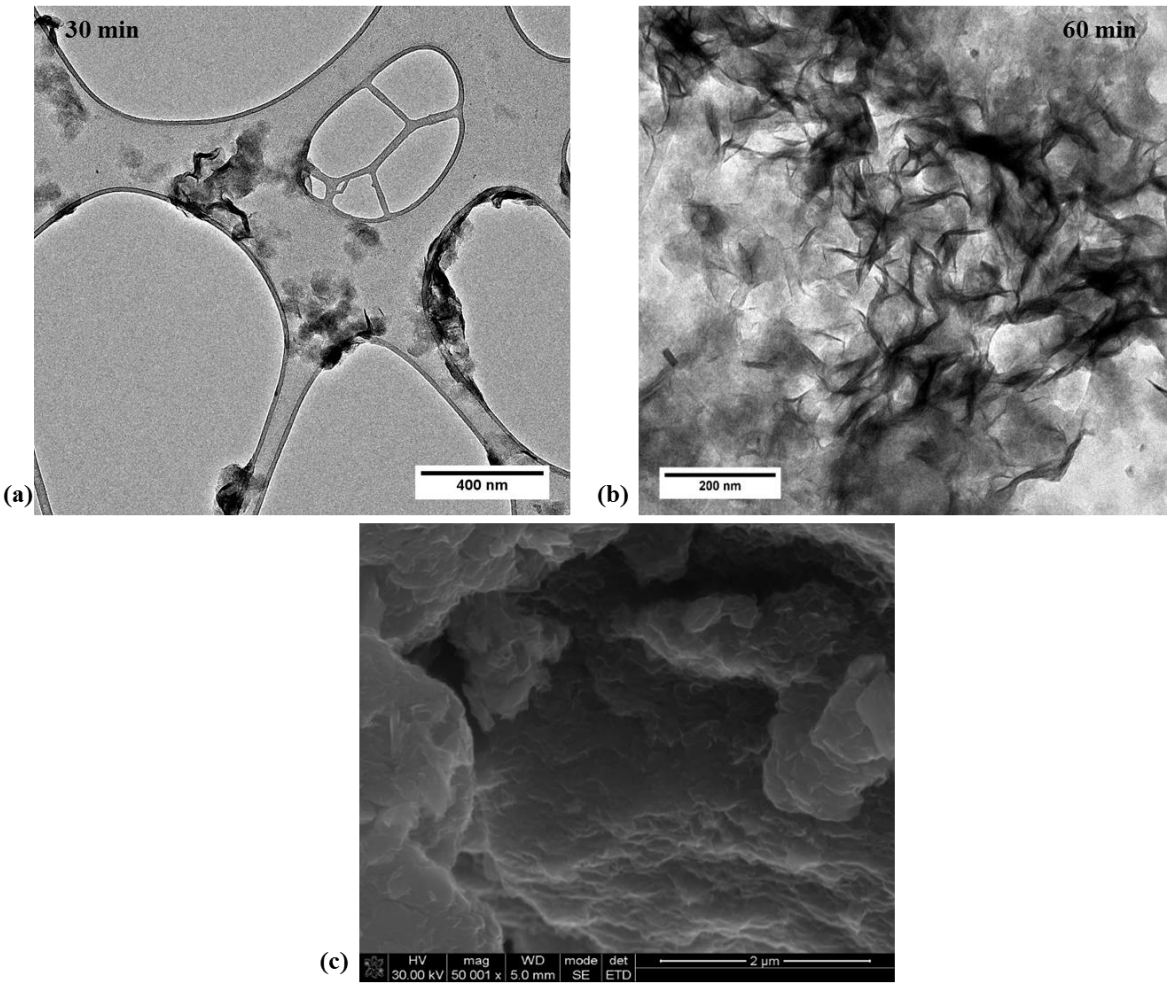


Figure 5.5: TEM images of WS_2 synthesized with thioacetamide for 30 (a) and 60 (b) minutes, including a SEM image (c) of the 60 min WS_2.

Diphenyl thiourea forms crumpled and folded nanosheets as well as structures in a flower-like morphology. The formation of the flowers starts with the formation of flat, thin nanosheets that grow and fold into a flower-like morphology as shown in Figure 5.6 (a-b). The folding into a flower-like morphology is usually a way to reduce the surface energy of

free-standing sheets.[14] The flower-like morphology can also be observed in the SEM image in Figure 5.6 (c). These materials show an abundance of exposed edge sites as was predicted by the dominance of the (101) plane on the PXRD patterns. It is not clear how the nanoflowers are formed, however, it could be that the 2D nanosheets on their own have unfavorable surface energy. So the 2D sheets agglomerate or stick to each other, hence minimizing the surface energy.[15] Although the focus of many studies has been on the flat monolayer WS_2 materials, 3D assemblies of these nanosheets into nanoflowers has many advantages. These structures have a high specific surface area, broad internal space, mechanical stability and easy accessibility to catalytically active sites.[16]The presence of many edge sites is excellent for electrocatalytic applications as the edge sites have been shown to be more catalytically active than the basal planes of the material.[17]

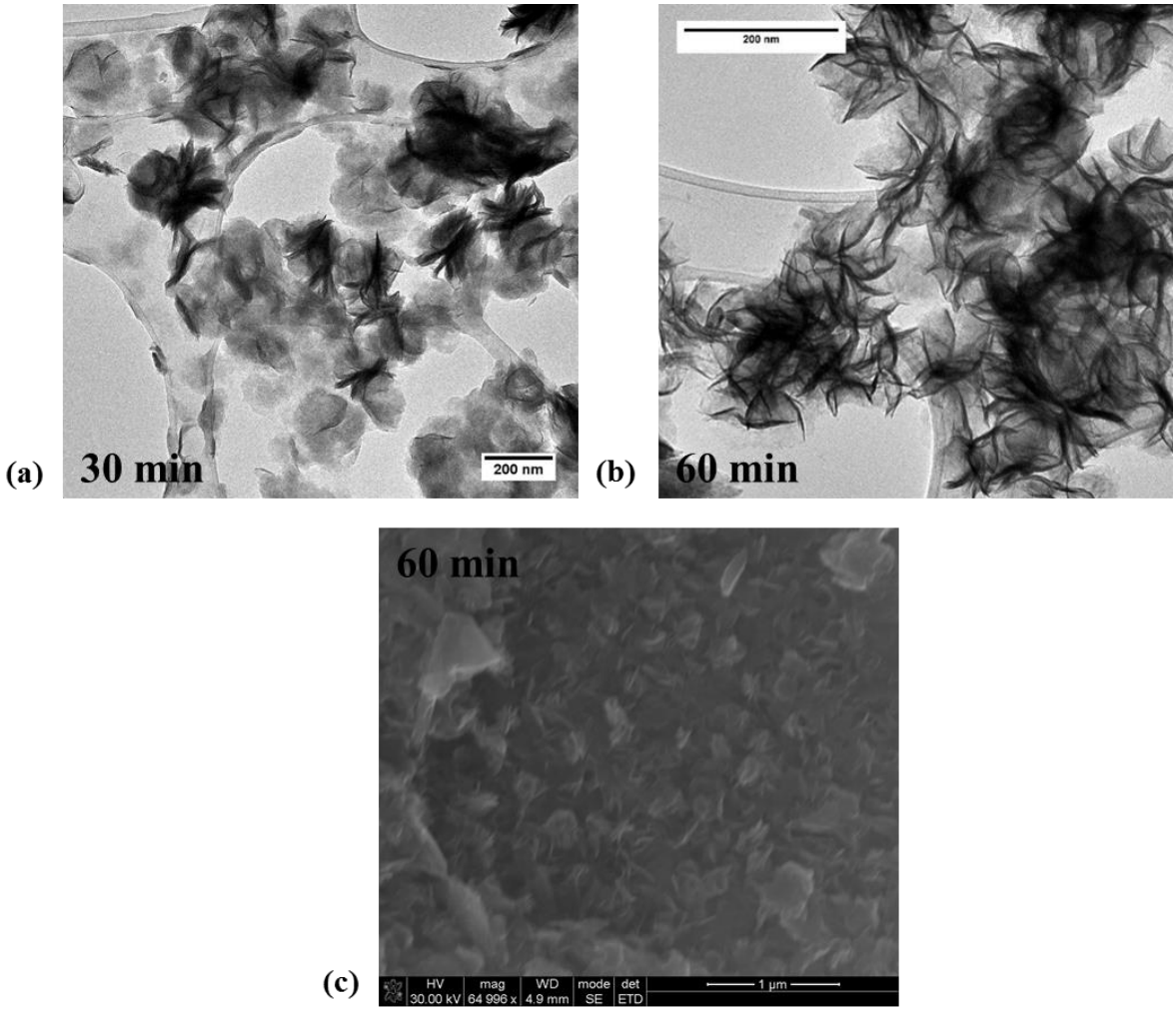


Figure 5.6: TEM images of WS_2 nanostructures obtained from diphenyl thiourea at (a) 30 and (b) 60 min reaction time and a (c) SEM image of the 60 minute WS_2 nanostructures.

FT-IR spectroscopy (Figure 5.7) was performed on the WS_2 material to elucidate whether oleylamine is capping the nanoparticles or not. The basic oleylamine vibrations are visible from the pure oleylamine spectrum. The spectra of the WS_2 particles have a different spectrum than that of free oleylamine as expected. The inset in Figure 5.7 shows the N-H stretch of oleylamine that is absent in the WS_2 spectra. The NH_2 wagging mode at about 798 cm^{-1} is also absent in the WS_2 spectra. The WS_2 spectra do contain the CH_2, CH_3 and C-N stretches of oleylamine, although they are much weaker. The WS_2 spectra also contain broadened NH_2 bend at about 1618 cm^{-1}. This indicates that oleylamine is present as a capping agent on the nanoparticles. The loss of the N-H stretch could be that the amine is chemisorbed onto the WS_2, causing the N-H bonds to be broken in order for the capping of the nanomaterials to occur. Oleylamine not only acts as a capping agent but also as a reducing agent and solvent for these reactions.

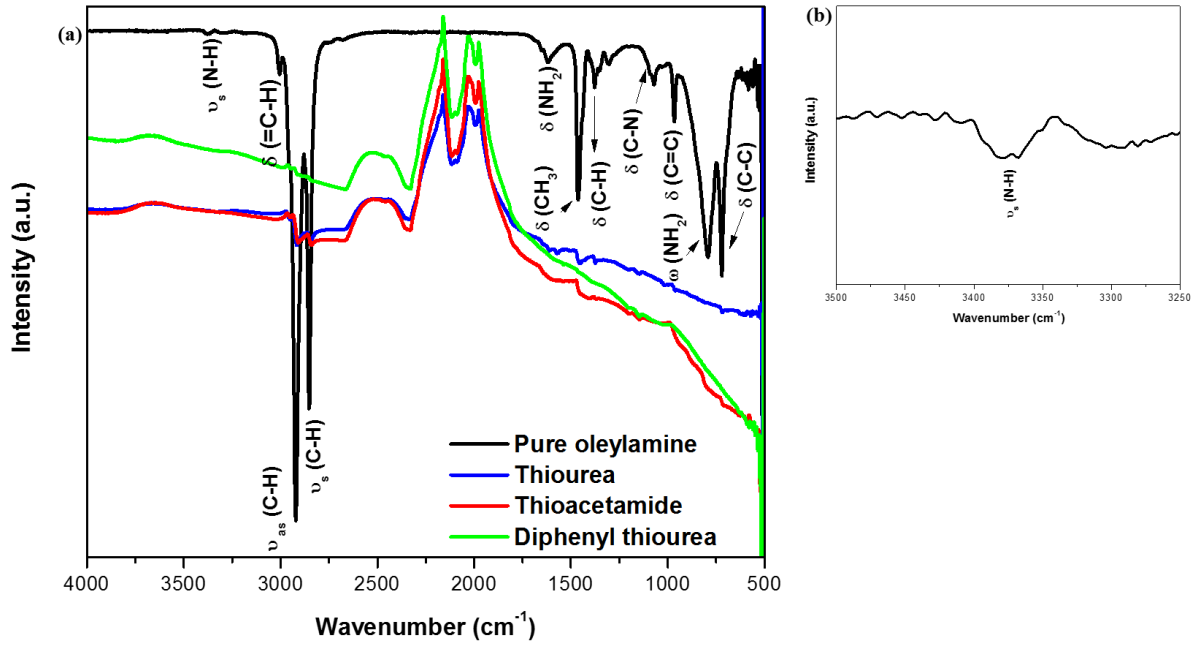


Figure 5.7: (a) FT-IR spectra of pure oleylamine (black) and WS_2 derived from thiourea (blue), thioacetamide (red) and diphenyl thiourea (green) for the 60 min reaction time and (b) magnification of N-H stretch on pure oleylamine.

Bulk WS_2 exhibits an indirect, low energy band gap; UV-Vis absorption and photoluminescence spectroscopy is able to indicate the widening of the band gap as well as a transition from an indirect to a direct band gap, as the materials get smaller. The UV-Vis

spectra in Figure 5.8 (a) show the characteristic absorption peaks for 2H- WS_2. Three distinct peaks are visible: exciton A, B, and C. As was previously stated, WS_2 that has more than one layer, undergoes a splitting of its valence band. The split is caused by spin-orbit and interlayer coupling, which results in the formation of a pair of absorption peaks (A-B). The peak denoted C is caused by high energy optical transitions between densities of states in the valence and conduction band. This transition (C) is not present in bulk WS_2.[18]From the spectra, it is evident that the peaks are most prominent for WS_2 obtained using diphenyl thiourea. The peaks weaken for thioacetamide-WS_2 and even further for thiourea-WS_2. This weakening could be due to the decrease in crystallinity of the WS_2 observed on the PXRD patterns. This means that the quality of the material is diminished and many trap states occur within the material that prevents efficient absorption of light, hence the weak absorption spectra.[19] The first absorption peak A occurs at approximately 627 nm and 617 nm for diphenyl thiourea and thioacetamide-WS_2 respectively. This is a significant blue shift from bulk WS_2 which absorbs light at the near infrared region (920 nm). This blue shift is due to quantum confinement in the nanomaterials.[20]The blue shift is beneficial as it makes the WS_2 a suitable candidate for use in visible light electronic and optoelectronic devices. The WS_2 derived from thiourea has a first absorption peak at a slightly higher wavelength of 670 nm. It still shows a blue shift compared to bulk WS_2 as well. The absorption at higher wavelengths could also indicate that the WS_2 particles obtained from thiourea are the largest compared to WS_2 obtained from thioacetamide and diphenyl thiourea. The PL spectra in Figure 5.8(b) show only the beginning of a weak emission peak at approximately 775 nm for all three samples. This emission is due to the indirect nature of the band gap of WS_2.[21] It has been shown that once there is more than one layer of WS_2, the emission is dramatically decreased because of the shift to an indirect band gap.[22]

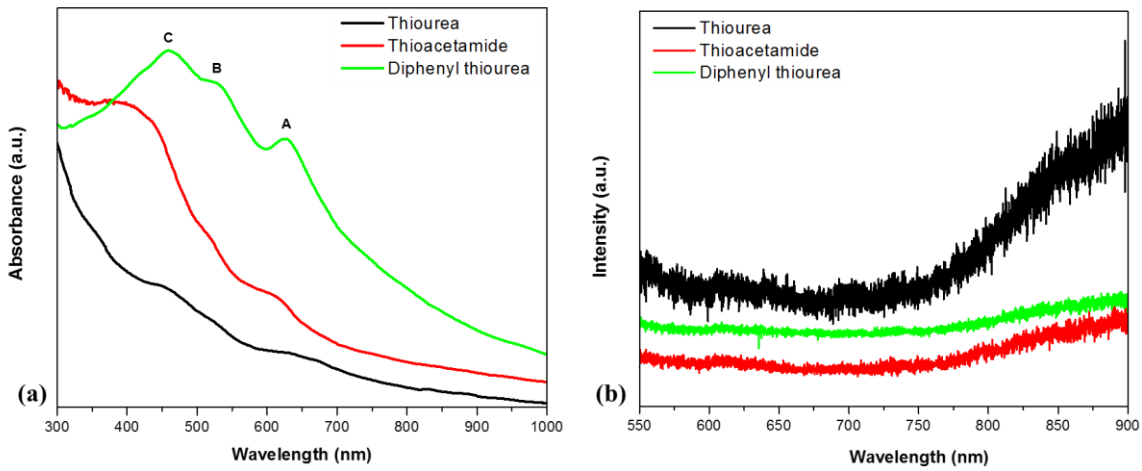


Figure 5.8: (a) UV-Vis absorption and (b) PL emission spectra of WS_2 obtained from thiourea, thioacetamide and diphenyl thiourea for the 60 min reaction time.

5.4 Proposed mechanisms

Because the reactions carried out in this work are all heating-up methods, we rely on thermal decomposition methods to propose possible reaction mechanisms for the formation of WS_2. Below are proposed mechanisms for the formation of WS_2 from the three sulphur precursors. Tungstic acid is a hydrated tungsten oxide that is used as the tungsten precursor in all three reactions. It has been found to decompose at 250 ℃ into WO_3 and steam as shown in equation 5.1.[10]

$$WO_3 \cdot H_2O \xrightarrow{250℃} WO_3 + H_2O \quad (5.1)$$

(i) Thiourea

Studies have been done to elucidate the thermal decomposition of thiourea. Theoretical studies suggest that there are almost eighteen reaction pathways that could take place during the thermal decomposition of thiourea.[23] Wang [24] and Timchenko[25] *et al.* showed that from 140 ℃ to 180 ℃ thiourea undergoes isomerization into ammonium thiocyanate (5.2).

$$CS(NH_2)_2 \xleftrightarrow{140℃-180℃} NH_4SCN \quad (5.2)$$

From there, decomposition occurs resulting in the release of the main gaseous products, namely: ammonia, carbon disulfide, cyanamide, and some H_2S.

$$CS(NH_2)_2 \xrightarrow{above\ 180℃} H_2S_{(g)} + H_2NCN_{(g)} \quad (5.3)$$

or

$$2\,CS(NH_2)_2 \xrightarrow{187℃-246℃} CS_{2\,(g)} + H_2NCN_{(g)} + 2\,NH_{3\,(g)} \quad (5.4)$$

From these decomposition products, WS_2 can be formed in the following ways:

$$2WO_{3\,(s)} + 3CS_{2\,(g)} \xrightarrow{OLA} 2WS_{2\,(s)} + 3CO_{2\,(g)} + 2S \quad (5.5)$$

$$2WO_{3\,(s)} + 4H_2S_{(g)} \xrightarrow{OLA} 2WS_{2\,(s)} + 4H_2O_{\,(g)} + O_{2\,(g)} \quad (5.6)$$

Thiourea is able to also act as a reductant for the W^{6+} when in excess and has been found to also stabilize the ultrathin nanosheets.[26,27] The thiourea molecules can be adsorbed onto the surface of the crystallites which will hinder the oriented crystal growth. This results in nanosheets that have many defects. This may be the cause for the lowered crystallinity of the WS_2 produced from thiourea.

(ii) Thioacetamide

It has been shown that thioacetamide decomposes at 150 ℃ in the following way:

$$(H_3C)CS(NH_2) \xrightarrow{150\,℃} H_2S + N \equiv CCH_3 \quad (5.7)$$[28]

The H_2S can further react with and reduce the WO_3 from H_2WO_4 to form WS_2 as shown in equation 5.6. The PXRD pattern for thioacetamide derived WS_2 showed some WO_3 impurities, which may have been caused by the O_2 evolved from the reaction.

(iii) N, N'-Diphenyl thiourea

It takes a reaction of aniline ($Ph{-}NH_2$) with carbon disulfide (CS_2) to make diphenyl thiourea.[29] Diphenyl thiourea is also able to form H_2S gas when in contact with water.[30] It has also been shown that diphenyl thiourea decomposes between 188-192 ℃ and has many decomposition products such as pyridine and possibly CS_2 and H_2S.[31] It could be that during the course of the reaction, CS_2 and/or H_2S is being released. Therefore WS_2 could be formed through the reaction of WO_3 with CS_2 or H_2S as shown in scheme 5 and scheme 6. From the reaction vessels, thioacetamide seems to have the fastest decomposition as WS_2 nucleation occurred at 260 ℃ which is the lowest temperature between the three precursors. It has been said from theoretical studies that precursors that are most reactive will form many nuclei at once, causing the formation of smaller particles.[32] Diphenyl thiourea formed WS_2 nuclei at 288 ℃ and thiourea at 300 ℃. From the classical nucleation theory, it was shown that the surface energy of the particles decreases after nucleation and during particle growth.[33] Nucleation of WS_2 from thioacetamide occurred at a lower temperature than that of diphenyl thiourea and thiourea. Since the nucleation temperature for thioacetamide is lower, it may be

that the surface energy of the nuclei was lower than those of diphenyl thiourea and thiourea derived WS_2. In order to reduce the higher surface energies, the WS_2 from diphenyl thiourea and thiourea formed assemblies of the nanosheets into flowers, while the WS_2 from thioacetamide remained in a folded sheet-like morphology.

5.5 Conclusion

Thiourea and its derivatives are able to act as sulphur sources to synthesize WS_2. They produce WS_2 with a sheet and flower-like morphology. The WS_2 produced exhibits improved optical absorption in the visible range compared to bulk WS_2. The morphology of the WS_2 shows many exposed edge sites which are essential for the electrocatalytic application that the WS_2 will be used for. Diphenyl thiourea seems to be the best sulphur source in this case, because it produces more crystalline WS_2 that has better optical absorption in the visible range of the solar spectrum. The formation of edge exposed WS_2 is prominent when using these sulphur sources, making it a suitable reaction method for producing electrocatalytically active WS_2 materials.

5.6 References

1. L. Zhang, X. Shen, H. Liang, S. Guo, and Z. Liang, *Journal of Colloid Science*, 2010, **342**, 236–242.
2. F. Li, W. Bi, T. Kong, C. Wang, Z. Li and X. Huang, *Journal of Alloys and Compounds*, 2009, **479**, 707–710.
3. S. Jeong, D. Yoo, J. Jang, M. Kim, and J. Cheon, *J. Am. Chem. Soc*., 2012, **134**, 18233-18236.
4. N. Ortiz and S. E. Skrabalak, *Langmuir*, 2014, **30**, 6649-6659.
5. H. Yan, J. Li, D. Liu, X. Jing, D. Wang and L. Meng, *CrystEngComm.*, 2018, **20**, 2324–2330.
6. Y. Kocak, Y. Akaltun and E. Gur, *J. Phys: Conf. Ser*., 2016, **707**, 012028.
7. T. A. J. Loh, D. H. C. Chua, and A. T. S. Wee, *Sci. Rep*., 2015, **5**, 18116.
8. S. P. Lonkar, V. V Pillai and S. M. Alhassan, *Chem. Asian J*., 2017, **12**, 2528.
9. L. Cheng, W. Huang, Q. Gong, C. Liu, Z. Liu and Y. Li, *Angew. Chem. Int. Ed*., 2014, **53**, 7860–7863.
10. C. L Veenas, L.R. Asitha, V.C. Bose, A.S. Aiswarya Raj, G. Madhu, and V. Biju, *IOP Conf. Series: Materials Science and Engineering*, 2015, **73**, 012119.
11. A. Berkdemir et al, *Sci. Rep*., 2013, **3**, 1755.

12. N. Peimyoo, J. Shang, W. Yang, Y. Wang, C. Cong and T. Yu, *Nano Res.*, 2014, 1-16.
13. Y. Chen, B. Song, X. Tang, L. Lu, and J. Xue, *Small*, 2014, **10**, 1536–1543.
14. X. Zhang, H. Xu, J. Wang, X. Ye, W. Lei, M. Xue, and H. Tang, *Nanoscale Res. Lett.*, 2016, **11**, 442.
15. S. Cao, T. Liu, W. Zeng, S. Hussain, X. Peng, and F. Pan, *J. Mater. Sci: Mater Electron*, 2014, **25**, 4300-4305.
16. A. Prabakaran, F. Dillon, J. Melbourne, L. Jones, R. J. Nicholls, P. Holdway, J. Britton, A. A. Koos, A. Crossley, P. D. Nellist and N. Grobert, *Chem. Commun*., 2014, **50**, 12360–12362.
17. S. H. Ahn and A. Manthiram, *Adv. Energy Mater*., 2016, **6**, 1–7.
18. G. Pagona, C. Bittencourt, R. Arenal and N. Tagmatarchis, *Chem. Commun*., 2015, **51**, 12950–12953.
19. M. Koperski, M. R. Molas, A. Arora, K. Nogajewski and A. O. Slobodeniuk, *Nanophotonics*, 2017, **6**, 1289–1308.
20. A. Bayat and E. Saievar-Iranizad, *Journal of Lumininescence*, 2017, **185**, 236–240.
21. H. Kim, H. Kim, J. Lee, H. Lee, D. Choi, J. Lee, W. H. Lee, S. H. Jhang, B. H. Park, H. Cheong and S. Lee, *ACS Nano*, 2015, **7**, 6854–6860.
22. K. M. Mccreary, A. T. Hanbicki, G. G. Jernigan, J. C. Culbertson and B. T. Jonker, *Sci. Rep.*, 2016, **6**, 19159.
23. Z. D. Wang, M. Yoshida and B. George, *Comput. Theor. Chem.*, 2013, **1017**, 91–98.
24. S. Wang, Q. Gao and J. Wang, *J. Phys. Chem. B*, 2005, **109**, 17281–17289.
25. V. P. Timchenko, A. L. Novozhilov and O. A. Slepysheva, *Russian Journal of General Chemistry*, 2004, **74**, 1046–1050.
26. J. Xie, H. Zhang, S. Li, R. Wang, X. Sun, M. Zhou, J. Zhou, X. Wen, D. Lou, and Y. Xie, *Adv. Mater*., 2013, **25**, 5807–5813.
27. H. Li, K. Yu, C. Li, B. Guo, X. Lei, H. Fu, and Z. Zhu, *J. Mater. Chem. A*, 2015, **3**, 20225–20235.
28. J. R. Bakke, J. S. King, H. J. Jung, R. Sinclair, and S. F. Bent, *Thin Solid Films*, 2010, **518**, 5400–5408.
29. B. C. Ranu, S. S. Dey, and S. Bag, *ARKIVOC*, 2003, **2003**, 14–20.
30. M. R. Maddani and K. R. Prabhu, *J. Org. Chem*., 2010, **75**, 2327–2332.
31. E. Lizarraga, C. Zabaleta, and J. A. Palop, *Journal of Thermal Analysis and Calorimetry*, 2008, **93**, 887–898.

32. J. Van Embden, A. S. R. Chesman and J. J. Jasieniak, *Chem. Mater*., 2015, **27**, 2246-2285.
33. J. Polte, *CrystEngComm*., 2015, **17**, 6809–6830.

Chapter 6

Cyclic voltammetry of WS_2 materials for determination of electrocatalytic activity as a counter electrode

6.1 Introduction

Dye-sensitized solar cells (DSSCs) have several advantages over other photovoltaic devices such as easy fabrication, eco-friendliness, and transparency.[1] The components of a DSSC include TiO_2 semiconductor sensitized by a dye, an iodine electrolyte, and a counter electrode.[2] The counter electrode reduces the oxidized electrolyte.[3] Originally, platinum was used as the counter electrode due to its excellent conductivity and catalytic activity,[3] however, platinum is expensive and prone to oxidation over time.[4] This makes large scale fabrication of DSSCs impractical. Many alternatives to platinum have been investigated such as carbon materials[2], nickel cobalt selenides[5] and alloys of platinum with other metals.

Transition metal dichalcogenides (TMDs) such as WS_2 and MoS_2 have drawn attention as they have promising catalytic activity. It has been shown that the edges of the TMD layers have promising electrocatalytic activity.[6] MoS_2 with a flower-like morphology was found to perform very well as an electrode material[7] because of the abundance of edge sites. The active sites are almost non-existent on the basal plane of WS_2 and hence it is essential that the particles used in this application are not flat. The edge sites have unsaturated metal atoms that facilitate the adsorption process of the electrolyte to be reduced.[8] The inorganic materials have the advantage of being diverse, abundant, easy to modify and of high catalytic activity compared to carbon or polymer materials previously used.[9] From the previous chapters, WS_2 nanomaterials with flowerlike morphologies were shown. Some of the samples were used to determine the catalytic activity for use as a counter electrode.

The nanomaterials are characterized through cyclic voltammetry (CV) to determine whether they are able to reduce the I_3^-/I^- electrolyte. The experiments are conducted through a three-electrode system consisting of a counter, reference and working electrode. There are certain characteristics of the cyclic voltammograms that help with the determination of the catalytic activity of the materials. Firstly, it is the potential difference between the anodic and cathodic peaks (E*pp*), sometimes referred to as the peak-to-peak separation.[10] The E*pp* is inversely proportional to the redox reaction rate. Ideally, a very low E*pp* is required as that indicates a

fast redox reaction rate.[2] Another important parameter includes the current of the cathodic (i_{pc}) and anodic (i_{pa}) peaks. In a reversible redox system the $i_{pa}/i_{pc} = 1$, meaning the current of the peaks should be equal and the oxidation and reduction peaks should be similar in shape.[2,9] In this study, the CV of some WS_2 materials obtained in the earlier chapters was performed and their electrocatalytic activity investigated.

6.2 Method and materials

6.2.1 Chemicals

Lithium iodide (LiI, 99%), iodine (I_2, ACS reagent 99.8%), lithium perchlorate ($LiClO_4$, 99.99%), fluorine-doped tin oxide (FTO) glass slide and toluene. All chemicals were purchased at Sigma Aldrich South Africa.

6.2.2 Experimental procedure

(i) Preparation of thin films

The WS_2 powders (40 mg) were mixed with 0.5 ml toluene and sonicated for 30 minutes. The paste was spin coated onto an FTO slide.

(ii) Preparation of the electrolyte

LiI (0.27 g), I_2 (0.1 g) and $LiClO_4$ (2.1 g) were mixed in 40 ml of acetonitrile and stirred for a few minutes until dissolved.

6.2.3 Characterization

Electrocatalytic characterization was performed on a Metrohm 728 stirrer cyclic voltammetry system. Measurements were done on the General Purpose Electrochemical System software (GPES).

6.3 Results and discussion

The most promising results obtained from the WS_2 nanoparticles were chosen and represented in the results below. The cyclic voltammogram of the platinum electrode is shown in Figure 6.1. Platinum is the state-of-the-art counter electrode used in DSSCs and was used for comparison purposes for the catalytic activity of the WS_2 nanomaterials. The four characteristic redox peaks are visible on the voltammogram, labelled with the corresponding redox reactions as shown below:

(1) $3I^- \rightarrow I_3^- + 2e^-$

(2) $2I_3^- \rightarrow 3I_2 + 2e^-$

(3) $3I_2 + 2e^- \rightarrow 2I_3^-$

(4) $I_3^- + 2e^- \rightarrow 3I^-$

The left pair of peaks (1 and 4) are the most important peaks as they give an indication of the catalytic activity of the counter electrode as these peaks correspond to the oxidation of I^- and the reduction of I_3^-. The peak-to-peak separation (E*pp*) between these two peaks is 926 mV.

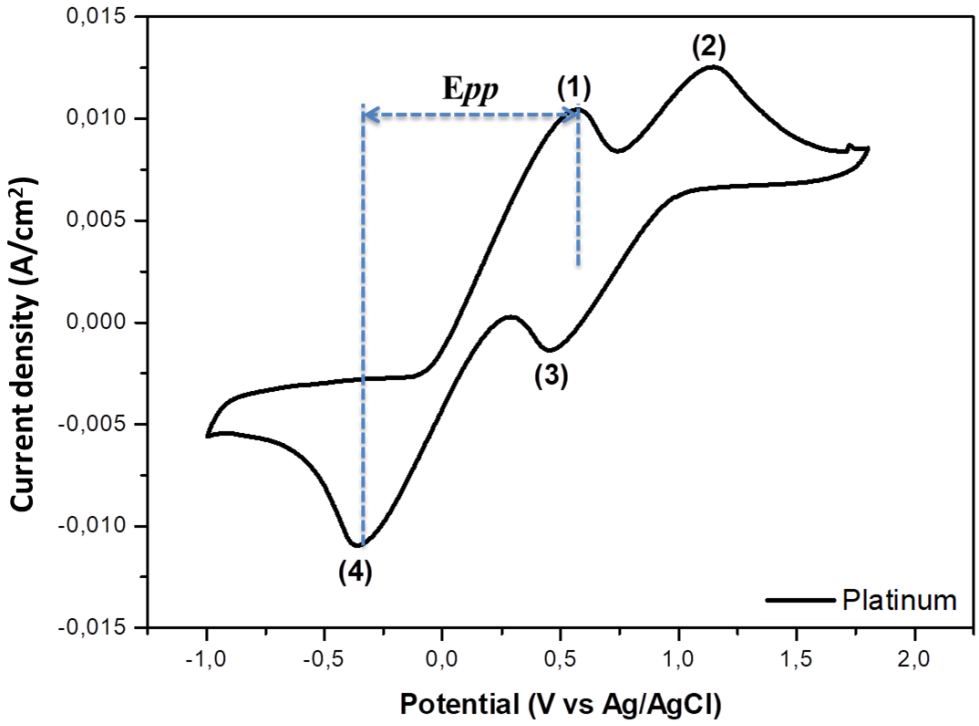


Figure 6.1: Cyclic voltammogram of platinum as a counter electrode.

Different WS_2 nanomaterials from the previous chapters were used in the cyclic voltammetry experiments to determine their catalytic activity. The materials were WS_2 synthesized with 50% octadecene concentration, 25% oleic acid concentration and WS_2 synthesized using diphenyl thiourea as a sulfur source. Figure 6.2 (a) shows the CV of the WS_2 synthesized with 50% ODE concentration. The first observation is that the cyclic voltammogram does not have all the redox peaks necessary for efficient reduction and oxidation of the iodine electrolyte. The peak corresponding to the reduction of I_3^- is very weak and not well-defined. If the weak peak is used to determine the E*pp*, it amounts to 540 mV. The shape of the two peaks on the left show that the system is not reversible. Reversibility is observed when the two peaks have the same shape and their current density ratio is equal to one.

When lower scan rates of 10 and 20 mV/s are used, the first oxidation and reduction peaks weaken or become less prominent. This indicates that with lower scan rates, insufficient oxidation and reduction of the electrolyte occurs. The 100 mV/s scan rate produced a cyclic voltammogram similar to that of the 50 mV/s scan rate, but with a slightly higher current density.

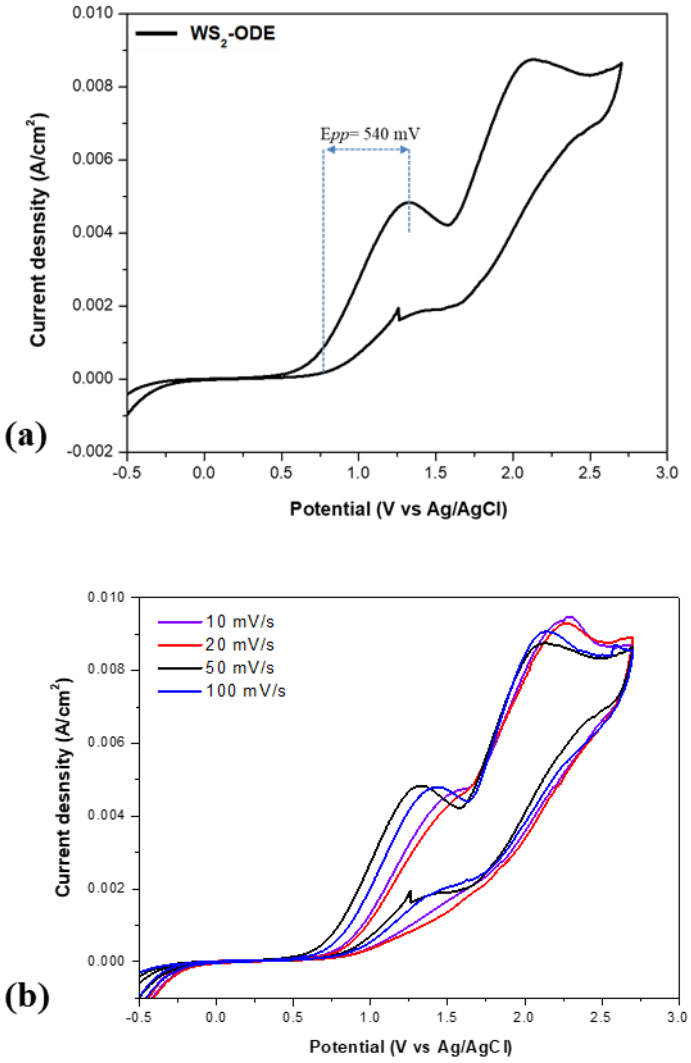


Figure 6.2: Cyclic voltammograms of WS_2 –ODE at (a) 50 mV/s and (b) 10, 20, 50 and 100 mV/s scan rates.

A 25% concentration of oleic acid produced WS_2 with excellent crystallinity with a stacked petal-like morphology was used. The morphology affords the WS_2 with many exposed edge sites, making it a promising candidate for the counter electrode application. However, the cyclic voltammogram in Figure 6.3(a) does not have the last peak corresponding to the reduction of I_3^- to $3I^-$. The WS_2 synthesized here is not suitable for use as a counter electrode in DSSCs, although it has many exposed edge sites, because the final reduction of

the electrolyte does not occur. Figure 6.3 (b) shows how the change in the profile of the voltammograms as the scan rates were varied. It is evident that the voltammograms, in this case, contain only one peak. This indicates that the redox reaction is not happening as it is required. It is also clear that the current of the only resultant peak increases as the scan rate increases. This is due to the flux of the electrolyte towards the electrode being higher at faster scan rates.

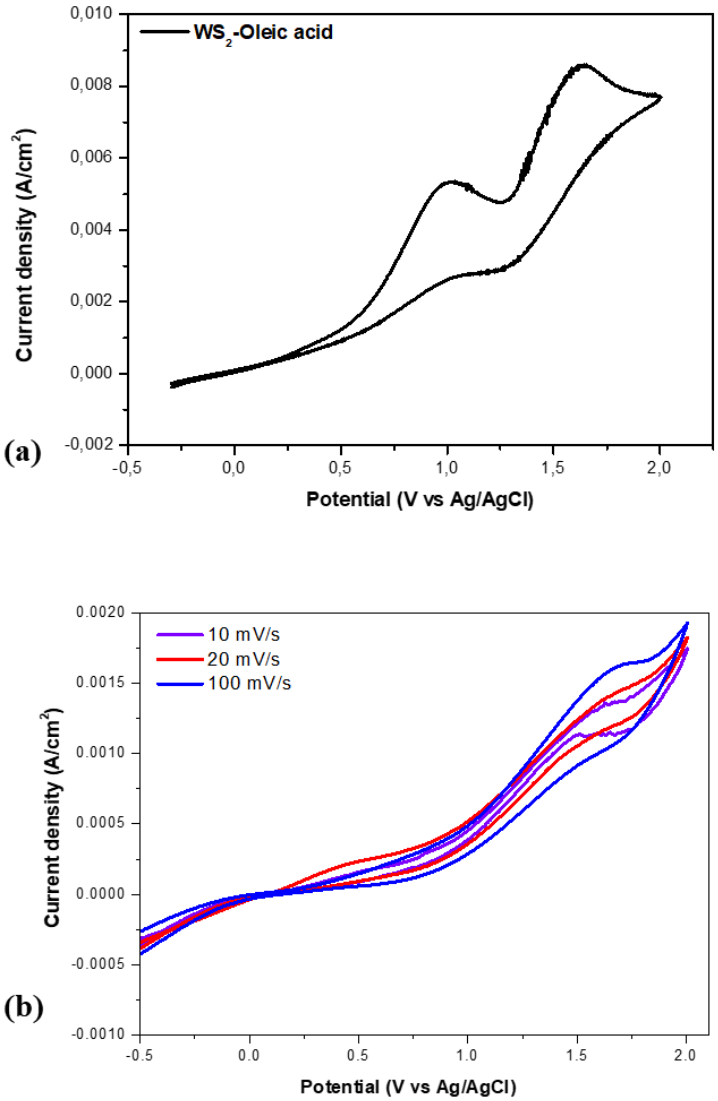


Figure 6.3: Cyclic voltammogram of WS_2 synthesized with a 25% oleic acid concentration. (a) 50 mV/s and (b) 10, 20, and 100 mV/s scan rates.

The most promising of the WS_2 samples comes from the synthesis with diphenyl thiourea as a sulfur source. The WS_2 produced here has a flowerlike morphology which is expected to have good catalytic activity.[7] The cyclic voltammogram in Figure 6.4 (a) contains four peaks with the fourth peak being very weak. The peak-to-peak separation (E*pp*) is 923 mV which is

only 3 mV lower than that of platinum. The peak to peak separation (E*pp*) indicates the redox barrier for the I_3^-/I^- redox couple. Therefore a low E*pp* means better catalytic activity.[6] However, the current density of the WS_2 is much lower than that of platinum which indicates poorer electrocatalytic activity. When the scan rates change to 10, 20 and 100 mV/s, as shown in Figure 6.4 (b), the characteristics of the cyclic voltammogram change. The cathodic and anodic peaks disappear, indicating very poor redox reactions.

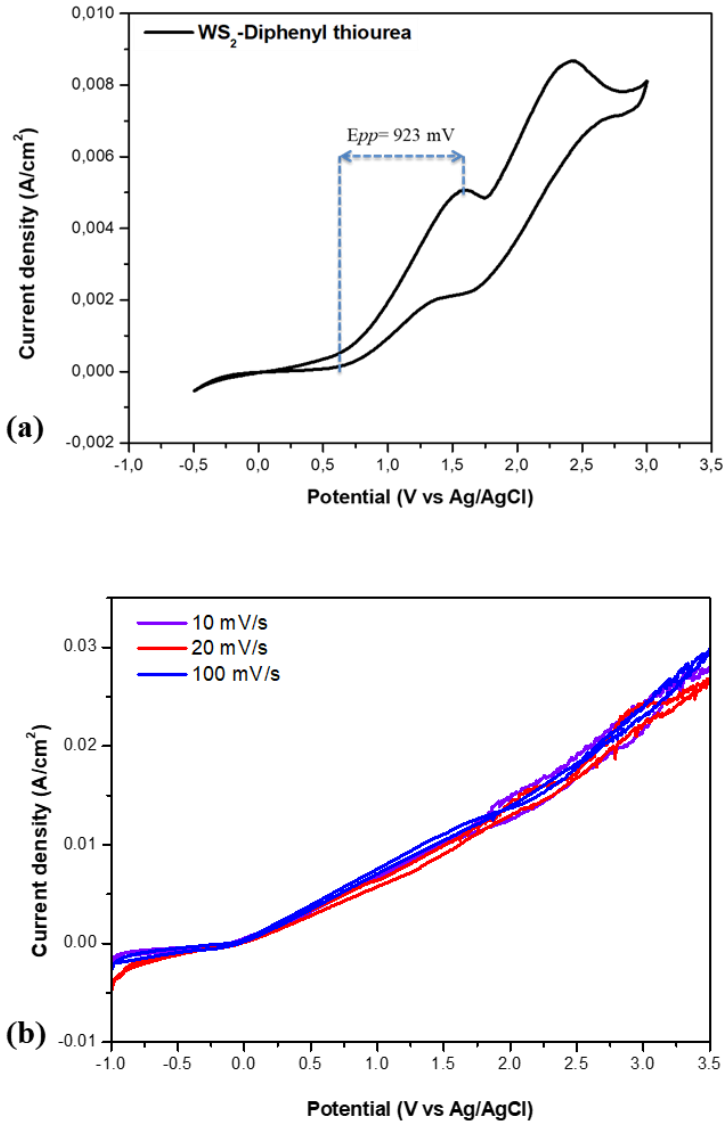


Figure 6.4: Cyclic voltammograms of WS_2 synthesized with diphenyl thiourea as a sulfur source. (a) 50 mV/s only and (b) combined voltammograms with 10, 20, and 100 mV/s scan rate.

It is clearly evident from the above results that the WS_2 samples do not have very efficient electrocatalytic activity towards the electrolyte compared to platinum. This is most likely caused by the presence of capping agents on the surface of the WS_2, forming a shell that hinders the diffusion of the electrolyte towards the WS_2 active sites. Other factors that could be influencing the activity include poor dispersion of the nanomaterials and the presence of impurities.

6.4 Conclusion

Although platinum is expensive and is prone to oxidation by the electrolyte over time, it appears to be the best option when compared to capped WS_2 materials. The WS_2 samples that were examined show poor catalytic activity and are not suitable for use as counter electrodes in dye-sensitized solar cells. The currents obtained were too low, the final reduction peaks were either weak or absent and there was no reversibility of the redox reaction. Using different scan rates also showed the instability of the WS_2 materials. In future, the post-synthesis stripping of the capping agent must be done.

6.5 References

1. S. Goo, L. Wang, C. Zhang, G. Qi, B. Guu, L. Liu and Z. Yuan, Nanoscale, 2017, **9**, 6837.
2. J. Wu, Z. Lan, J. Lin, M. Huang, Y. Huang, L. Fan, G. Luo, Y. Lin, Y. Xie and Y. Wei, *Chem. Soc. Rev*., 2017, **46**, 5975.
3. D. Vikraman, S.A. Patil, S. Hussain, N. Mengal, H. Kim, S. Jeong, J. Jung, H. Kim and H. Joon Park, *Dyes and Pigments*, 2018, **151**, 7-14.
4. J. T. Mlack, P. Masih Das, G. Danda1, Y. Chou, C. H. Naylor, Z. Lin, N. Perea López, T. Zhang, M. Terrones, A. T. C. Johnson and M. Drndić, *Sci. Rep*., 2017, **7**, 43037.
5. X. Qian, H. Li, L. Shao, X. Jiang, and L. Hou, *ACS Appl. Mater. Interfaces*, 2016, **8**, 29486-29495.
6. C. Lin, C. Tsai, F. Tseng, Y. Yu, H. Wu, and C. Hsieh, *Nanoscale Res. Lett*., 2015, **10**, 446.
7. H. Heinz, C. Pramanik, O. Heinz, Y. Ding, R.T. Mishra, D. Marchon, R.J. Flatt, I. Esterla-Lopis, J. Llop, S. Moya, and R.F. Ziolo, *Surface Science Reports*, 2017, **72**, 1-58.
8. A. Eftekhari, *J. Mater. Chem. A*, 2017, **5**, 18299.

9. M. Wu, Y. Wang, X. Lin, N. Yu, L. Wang, L. Wang, A. Hagfeldt and T. Ma, *Phys. Chem. Chem. Phys.*, 2011, **13**, 19298-19303.
10. J. Liang, J. Li, H. Zhu, Y. Han, Y. Wang, C. Wang, Z. Jin, G. Zhang and J. Li, *Nanoscale*, 2016, **8**, 16017.

Chapter 7

General conclusions and recommendations

The study shows that the colloidal synthesis of WS_2 is an effective way to synthesize WS_2 nanostructures. This method of synthesis favours the formation of three-dimensional structures, rather than flat, two-dimensional nanosheets. With regard to the sulphur precursors, it was shown that thiourea derivatives are good sulphur sources and that the nanostructures can be tailored by choosing derivatives with different decomposition temperatures or rates. It was also established that organometallic precursors are not suitable for the colloidal synthesis of WS_2. More stable tungsten precursors are required to produce pure and good quality WS_2. It was also shown that long-chain organic molecules such as oleylamine and oleic acid can be used to passivate the nanostructures, however, oleic acid, oleyl alcohol and 1-octadecene work better as additional capping agents to oleylamine.

It was shown that many of the samples contained tungsten oxide impurities. This was most likely caused by oxidation that occurred when aliquots were taken and the incomplete decomposition of the tungstic acid (H_2WO_4) precursor. The recommendation would be to synthesize the materials in a glove box until the particles are dried. In addition, using more air stable precursors would be beneficial in that they will not react with the air before being placed in the reaction flask.

Another recommendation is with regards to the application of the WS_2 as counter electrodes in dye-sensitized solar cells. The electrocatalytic activity of the WS_2 was not very good as shown by the irreversibility of the cyclic voltammograms. This may have been due to the presence of capping agents on the surface of the particles that made it difficult for the electrolyte to reach the active sites on the particles. The removal or stripping of the capping agents from the nanoparticle surface is a strategy that could be used to improve the catalytic activity of the nanoparticles. The most used methods are solvent washing and annealing. Solvent washing have proved ineffective in this case. Therefore, other methods that could be used in future to strip the capping agents are to use gentle heating of the nanoparticles in pure acetic acid. This method has been used for metal particles passivated with oleylamine. Another recommendation is to use ligand exchange methods. This method entails replacing the long chain hydrocarbons such as oleylamine with shorter chain molecules that are able to competitively bind to the nanoparticles. Other methods include using UV radiation to decompose the capping agents.

When it comes to the electrocatalytric measurements, it would be beneficial, in future, to include cycling stability performance tests as well as electrochemical impedance spectroscopy (EIS) tests. The cycling stability tests would give an indication of the stability of the materials over time. The results would provide a lifetime of the materials. The EIS tests contain information about the interface between the material and the electrolyte and the reactions that occur at the interface. Having these two tests would give information on why the current WS_2 are not performing as well as they were expected to.